2014-05-26

An X-ray Source Model and Characterization Method for Computing kV Radiation Dose

Poirier, Yannick

UNIVERSITY OF CALGARY

An X-ray Source Model and Characterization Method

for Computing kV Radiation Dose

by

Yannick Poirier

A THESIS

SUBMITTED TO THE FACULTY OF GRADUATE STUDIES

IN PARTIAL FULFILLMENT OF THE REQUIREMENTS FOR THE

DEGREE OF DOCTOR OF PHILOSOPHY

DEPARTMENT OF PHYSICS AND ASTRONOMY

CALGARY, ALBERTA

May, 2014

Abstract

According to the American Association of Physicists in Medicine Task Group (AAPM) 75, it is the responsibility of the medical physics community to assess, reduce, and optimize the imaging dose delivered during image-guided radiation therapy. It is currently difficult to accurately estimate patient-specific spatial dose distributions deposited by kilovoltage (kV) cone-beam CT (CBCT) using existing techniques. This thesis describes the development and validation of a characterization method and virtual point source model for describing kV radiographic and CBCT x-ray imaging units for our in-house kV dose computation software, kVDoseCalc.

kV CBCT beams have spatial and spectral fluence variations. In this thesis, the spectrum is characterized using the accelerating potential (kVp) and half-value layer (HVL). These are matched to spectra generated by third-party freeware. The fluence is then isolated from measured in-air kerma. We assume that the fluence is a function of three separate independent variables: the transverse-axis spectra; and the transverse- and radial-axis fluence profiles. This work demonstrates that kV x-ray sources can be characterized using in-air ionization chamber measurements of HVL and kerma profiles.

The characterization method and model are validated by comparing the absorbed dose computed by kVDoseCalc with measurements taken using ionization chambers and thermoluminescent detectors. Doses were measured in homogeneous and heterogeneous block phantoms for radiographic imaging procedures. We then measured imaging doses in homogeneous cylindrical and heterogeneous anthropomorphic phantoms for default CBCT protocols. The percent dose difference between measurement and computation was generally $\leq 3\%$ in homogeneous and $\leq 6\%$ in heterogeneous geometries, respectively. In the anthropomorphic phantom, the average percent difference ranged from 3–6% depending on the imaging protocol and site.

The described method makes the accurate computation of radiographic and CBCT absorbed dose possible. This method has since been used by others in our group to accurately characterize a conventional CT scanner, superficial/orthovoltage therapy units, and to characterize an *in-vivo* film dosimetry program in our centre. Our technique is notable for relying only on empirical measurements. It allows a more accurate kV dose computation than treatment planning systems adapted for this purpose and is more clinically feasible than conventional Monte Carlo simulations.

Acknowledgements

I would first like to thank Dr. Alexei Kouznetsov, who coded the first implementation of the software I used in this project. Through our close collaboration, I was able to devise a kv x-ray source characterization method and model that is easy to implement in a clinical medical physics setting. I would then like to thank my supervisor Dr. Mauro Tambasco, who provided the original idea and motivation for the project. Without his advice and frequent revisions, I would not have been able to present my work at so many conferences and in publications. I also thank Dr. Wendy Smith, who took on the role of co-supervisor late in this project and provided much-needed support in writing and guiding the introduction of this thesis.

Next, I would like to thank my colleagues Phillip McGeachy, Dr. Sarah Quirk, Stefano Peca and Kevin Hynes who often stayed late so that I could complete my measurements. I also thank Dr. Eduardo Villarreal Barajas, whose support in the characterization of the high-sensitivity thermoluminescent detectors at low energies was instrumental in the anthropomorphic phantom measurements described in Chapter 6. Machine-shop specialists, Leo Moriarty and Alan Michaud, were extremely helpful in designing and fabricating a number of equipment crucial to the success of this project, notably the cylindrical acrylic phantom and the TLD chip holders used in Chapter 6. I am extremely grateful for their timely and efficient support.

Finally, I would like to thank my friends and family for their love and support, without which I would not have been able to finish this project.

Table of Contents

List of Tables

List of Figures and Illustrations

List of Symbols, Abbreviations and Nomenclature

Symbol	Definition
μ/ρ	Attenuation Coefficient
μ_{en}/ρ	Mass-energy attenuation Coefficient
3DCRT	Three-Dimensional Conformal Radiation Therapy
AAPM	American Association of Physicists in Medecine
ALARA	As Low as Reasonably Achievable
ART	Adaptive Radiation Therapy
BED	Biologically-Equivalent Dose
BEIR	Committee on the Biological Effects of Ionizing Radiations
CPE	Charged Particle Equilibrium
CT	Computed Tomography
CBCT	Cone-Beam Computed Tomography
CTDI	CT Dose Index
CTDI_{100}	CTDI Measured with a 100 cc Ionization Chamber
CTDI_w	Weighted CTDI
CTDI_{vol}	Volumetric CTDI
CTV	Clinical Target Volume
DGRT	Dose-Guided Radiation Therapy
D50	Dose to 50% of the Volume
DICOM	Digital Imaging and Communication in Medecine
DLP	Dose-Length Product
DTS	Digital Tomosynthesis
ERR	Excessive Relative Risk
EPID	Electronic Portal Imaging Device

FBT	Full Bowtie
GTV	Gross Tumor Volume
GUI	Graphical User Interface
HBT	Half Bowtie
HU	Hounsfield Unit
HVL	Half-Value Layer
ICRP	International Comission on Radiation Protection
ICRU	International Comission on Radiation Units
IGRT	Image-Guided Radiation Therapy
IMRT	Intensity-Modulated Radiation Therapy
ITV	Internal Target Volume
KERMA	Kinetic Energy Released per Unit Mass
kV	Kilovoltage
Linac	Linear Accelerator
LNT	Linear No-Threshold
LBTE	Linear Boltzmann Transport Equation
OAR	Organ At Risk
OBI	On-Board Imager
MCP-N	Mg, Cu, P
MSAD	Multiple-Scan Average Dose
MV	Megavoltage
PMT	Photomultiplier Tube
POI	Point of Interest
PRV	Planning Organ at Risk Volume
PTV	Planning Target Volume
QA	Quality Assurance

QUANTEC	Quantitative Analysis of Normal Tissue Effects in the Clinic
SBRT	Stereotactic Body Radiation Therapy
SSD	Source-to-Surface Distance
TERMA	Total Energy Released per Unit Mass
TLD	Thermoluminescent Detector
TPS	Treatmeant Planning System
U of C	University of Calgary
VIP-Man	Visual Photographic Man
VMAT	Volumetric Modulated Arc Therapy
XVI	X-ray Virtual Imager
Z	Atomic Number

Chapter 1

Introduction

1.1 General Introduction

1.1.1 Cancer and Image-Guided Radiation Therapy

Introduction

With an expected 187,600 new cases and 75,500 related deaths in 2013, cancer is a leading cause of death in Canada, having caused 29.8% of all deaths in 2009[32]. The main treatment options for cancer are radiation therapy, surgery, and chemotherapy. Two-thirds of all cancer patients will receive radiation therapy[8], making radiation therapy, usually delivered by a linear accelerator (linac) one of the mainstays of cancer treatments. Studies estimate that of the ∼9% of radiation therapy patients who develop a secondary cancer, ∼8% of the cancers (or ∼0.7% of the patients) will be induced by the therapy itself[19]. It is the responsibility of the radiation oncology and medical physics community to justify the risk posed by the radiation dose delivered to patients in view of its benefits.

Radiation therapy has undergone many innovations since its inception. Modern techniques, such as three-dimensional conformal therapy (3DCRT), intensity-modulated radiation therapy (IMRT), and volumetric modulated arc therapy (VMAT), allow radiation treatment plans to conform more closely to the physical shape and volume of the tumor, minimizing the irradiation of healthy tissues. While this conformality increases the radiation treatment plan quality, it also causes higher dose gradients near the edges of the treated area. These plans therefore require more precise patient positioning[135, 35]. Historically, patients were positioned by aligning external fiducial markers such as tattoos to treatment room positional lasers, using immobilization devices, or using two-dimensional x-ray film

portal imaging. Today, the level of conformality and sophistication of these state-of-the-art radiation therapy techniques require that the radiation fields be matched with details of the patient's internal anatomy[159, 102]. There is a need to implement and improve image-guided radiation therapy (IGRT) techniques to achieve better position verification accuracy[102].

The main objectives of IGRT techniques are to ensure that the target volume is directly irradiated, to allow safe margin reduction and sharper dose distributions, to track inter-fractional volumetric changes, to track the tumor motion in real-time during radiation therapy gating or tracking, and to permit adaptive radiation therapy (ART)[30]. These techniques and objectives will be explained in greater detail in the following subsections.

IGRT techniques

The history of IGRT begins with film portal imaging in the sixties and seventies. Unfortunately, the development time, and poor reproducibility of radiographic films meant that film portal imaging was infrequently used and prone to large ($\leq$ 1 cm) positional errors[178]. Modern IGRT approaches were first introduced when the electronic portal imaging device (EPID) technology was developed in the nineties. The EPID is a planar detector aligned with the megavoltage (MV) treatment beam that can image the patient on the treatment bed (Fig. 1.1). The EPID is a convenient imaging device because it requires no post-processing, it is integrated to the linac, and it can image the patient in the treatment position immediately before receiving treatment. It is the development of the EPID that made modern IGRT techniques possible[178].

Images taken with therapeutic x-rays (6–18 MV) have poor contrast compared to diagnostic (80–140 kV) energy x-rays. In fact, Groh *et al.* measured signal-to-noise ratio for diagnostic imaging kV x-rays as 6.5 times better than MV[65]. The Compton scattering interactions, which dominate at MV energies, depend only on electron density, while at kV energies, the Z-dependent photo-electric effect provides additional contrast[11, 89]. If we

use a dedicated kV imaging device in the treatment room, the contrast between soft tissues and bones can be vastly improved. The kV imaging system is often integrated to the linac where it is located orthogonally to the treatment beam, such as in the Elekta X-ray Virtual Imager (XVI) or the Varian On-Board Imager (OBI) (Fig. 1.1). Either MV or kV images can be used to position the patient according to digitally reconstructed radiographs, which are radiograph-like images reconstructed from the planning CT. In addition, an orthogonal MV-kV configuration also allows a technique called orthogonal imaging, although it is not as common as kV or MV imaging used on their own. In orthogonal imaging, planar images are taken simultaneously using both MV and kV imaging. The registration between these two images and the planning CT improves patient positioning accuracy compared to using either imaging system individually.
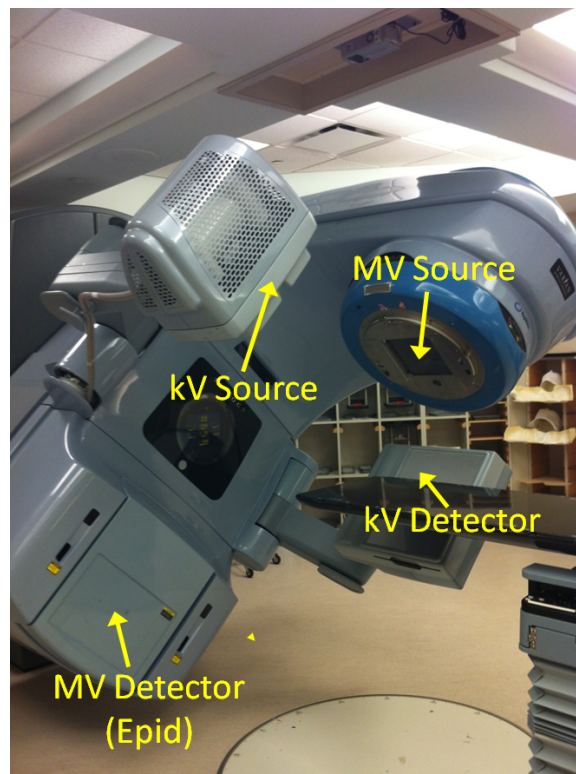
Figure 1.1: Megavoltage and kilovoltage beams and imaging devices on a Varian linac.

As we will explain in further subsections, it is sometimes desirable to obtain 3-D imaging of the patient during IGRT. Ideally, we would replicate the simulation imaging used to create the radiation therapy plan in the first place—via a CT scanner. To reduce the opportunities for the patient position to change between imaging and treatment, it is best if the patient is imaged in treatment position immediately before receiving their radiotherapy. We might achieve this using on-rail fan-beam CT scanners (Fig. 1.2a) installed in the treatment room, but this necessitates the accommodation of and training on dedicated additional equipment[158]. The image is acquired by railing in the CT scanner, performing the scan, and moving the CT arm out of the treatment area. This takes time during which the patient position might change. On-rails CT scanners also cannot be used to image during treatment for gated or adaptive radiotherapy treatments[158]. Helical therapy machines such as a TomoTherapy's Hi-ARTII^{TM} have a detector directly in the path of the beam. This allows a routine MV fan-beam CT to image the patient in the treatment position and measure the patient exit dose. Unfortunately, helical therapy units only account for a minority of all radiation therapy treatments and several factors limit their widespread use, such as 5–15 times longer treatments.[145, 166].

Since linacs are capable of a 360° rotation and already include imaging devices, it is possible to use them as a convenient alternative to fan-beam CT. Fan-beam CT images patients one slice (or set of slices in multi-slice scanners) at a time while the patients move through the scanner. In contrast, cone-beam CT (CBCT, Fig. 1.2b) uses one large ($\sim$ 20 cm width) field that effectively images all the slices at once. This means that only one rotation is needed and the patient can remain immobile. CBCT is ideally suited for gantry-operated linacs, but the image quality is lower than fan-beam CT due to the increased detection of scattered photons. CBCT can be performed either with the therapeutic MV beam and EPID, or with a dedicated orthogonal kV imaging unit. Some progress has also been made in performing CBCT using both MV and kV beams simultaneously for a shorter scan, but

this modality is still at the experimental stage[183].

Finally, digital tomosynthesis (DTS) is one the latest developments in IGRT imaging techniques[62]. DTS techniques use digital image acquisition to keep track of individual 2-D projections. Instead of the continuous 360° rotations of conventional CT and CBCT scans, DTS scans image in a few angles using discrete image acquisition. Images acquired by DTS deposit much lower dose per image acquired, but also have lower quality due to the relatively low angular spread sampled[62, 190, 171]. However, breathing motion artifacts have been partially removed by using motion-compensation in the reconstruction process[171].

Alternatively, DTS can be used to obtain 4D CBCT images by discriminating between 2-D projections taken at different phases of the respiratory cycle. This process, called phase-matched DTS, allows the reconstruction of a 4D CBCT[192]. These images provide valuable time-dependent spatial information directly before treatment[192]. Although images acquired by DTS are acquired slightly differently from conventional CBCT, both techniques are similar from a dosimetric point of view since they use the same x-ray beams.

Technically speaking, any use of imaging to verify the position of the patient or target qualifies as image-guidance. These include non-radiographic methods such as in-room ultrasound or magnetic resonance imaging and older techniques such as portal film imaging. This thesis is concerned with evaluating the radiation dose deposited using ionizing radiation in imaging procedures such as 2-D portal/radiographic imaging and 3-D cone-beam CT (Fig. 1.1)[178]. In general, MV imaging delivers a much larger dose to acquire images of lower quality than kV imaging[87, 65, 30, 54, 49]. MV imaging dose can be easily calculated using the same commercial treatment planning systems (TPS) that calculate the therapeutic dose. It is thus relatively trivial to calculate and include the MV imaging dose in radiation treatment plans[3, 174]. Among kV imaging techniques, CBCT delivers more dose to a greater volume than planar 2-D imaging[135, 126, 49] (Table 1.1) and is computationally and experimentally more difficult to estimate due to rotation. Many clinics have recently adopted

Conventional CT
Patient moves, Slice-by-slice imaging
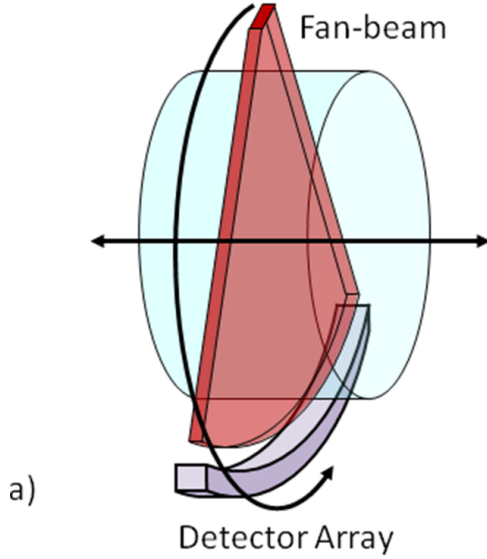
Cone-Beam CT
Patient still, All-in-one imaging

Fan-beam

Cone-beam

a)

b)

Detector Array

Detector Array
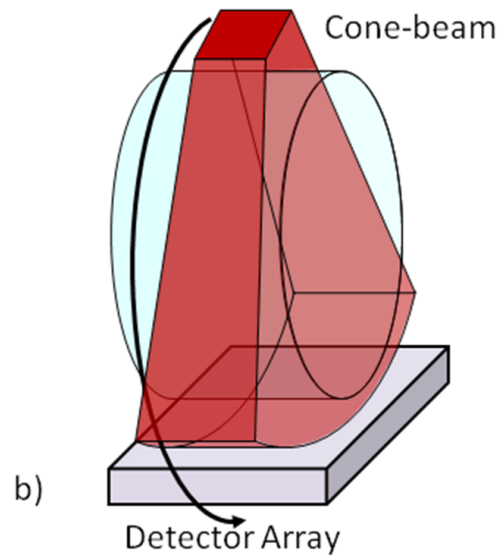
Figure 1.2: Comparison between conventional fan-beam CT (a) and cone-beam CT (b). Cone beams can image the patient without altering the treatment position, but suffer from reduced image quality due to increased scatter.

kV CBCT[88]. Therefore, while we will describe IGRT techniques in general, we will pay special attention to the use of kV CBCT imaging. As new imaging techniques and protocols such as phase-matched DTS are developed, the work in this thesis can be used to evaluate their dose deposition as well.

1.1.2 Uses of IGRT

Uses of IGRT: Treated volume reduction

To understand the advantages offered by safely reducing the treated volume, it is helpful to review the various volumes of interest in radiation therapy (Fig. 1.3).The tumour visible on the planning CT image is called the gross tumor volume (GTV). The microscopic spread of the disease may exceed the visible volume of the tumour by a certain distance depending

on the specific disease being treated. To account for this, we add a margin to the GTV to obtain the clinical target volume (CTV). In some cases, particularly for tumours attached to structures which move during respiration, an internal target volume (ITV) takes into account the intra-fractional CTV motion. Finally, we add another margin to allow for the inter-fractional uncertainty in the position of the ITV. This uncertainty can be caused by difficulties in reproducing the setup of the patient, by motion of the organs between fractions (e.g., prostate tumors), or by uncertainties in the treatment delivery itself (e.g., in-room lasers, isocentre positions). This planning target volume (PTV) is the volume to which we plan the prescribed dose to maximize its conformality and homogeneity. Organs at risk (OARs) are also defined in radiation therapy planning as critical structures in which the dose needs to be minimized to avoid radiation toxicity. As for the PTV, a margin accounting for inter- and intra-fractional motion/setup errors can be added to the OARs to produce the planning organ at risk volume (PRV)[97, 83].

It stands to reason that if the PTV volume can be reduced, total volume receiving the prescribed dose is decreased. Since this reduces the volume of healthy tissue and/or OAR receiving the prescribed dose, a higher quality plan can be delivered to the patient. This can be achieved in a number of ways. First, verification imaging can reduce the margins added to the CTV to create the PTV. Second, real-time gating or tracking can reduce the margins added to the CTV to create the ITV and PTV. Finally, advanced radiation therapy

Table 1.1: Typical OAR $D50$[1] doses delivered by imaging in Varian linacs[2].

Imaged site and OAR	MV portal imaging	kV radiograph	kV CBCT
Thorax imaging: heart	3.5 cGy	0.07 cGy	0.42 cGy
Pelvis imaging: bladder	3.3 cGy	0.07 cGy	1.6 cGy
Head imaging: eyes	4.3–4.8 cGy	0.12 cGy[3]	0.05-0.06 cGy[3]

[1]Values represent the minimum dose to 50% of the OAR volume, $D50$.
[2]Values obtained from Ding and Munro, 2013[49].
[3]kV CBCT in the head uses a partial arc which spares the eye, explaining why the eye dose is lower than for kV radiographs.
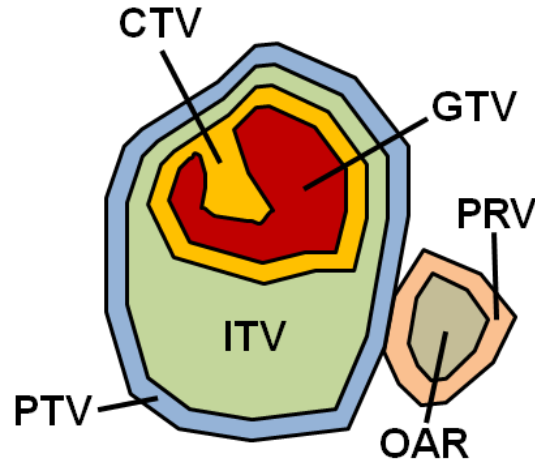
Figure 1.3: Depiction of the various volumes of interest in radiation therapy planning. IGRT techniques allow the safe reduction of margins around the OAR and ITV for better sparing of the OAR or escalation of the dose to the PTV. These volumes are defined in ICRU publication 50[83].

techniques such as IMRT and VMAT sculpt the dose to more closely match the PTV. Because high conformality plans have sharper dose gradients, a delivery error or inaccuracy leading to a geometrical miss of the target carries a much greater risk of underdosing the PTV, leading to loss of local tumour control. For this reason, they require IGRT techniques to be safely delivered[178]. This is particularly true in the case of hypo-fractionated stereotactic body radiation therapy (SBRT). Since IGRT techniques developed concurrently with high conformality techniques (e.g., IMRT, VMAT), both techniques are usually used together, and margin reduction and better conformality are associated.

The use of IGRT techniques reducing the PTV, whether by margin reduction or by dose sculpting, improves the quality of care to the patient in two ways. First, the dose to the PRV can be reduced to decrease the occurrence and severity of morbidities caused by the treatment. For instance, treating head and neck (H&N) tumours with IMRT over 3DCRT allows a reduced dose to the parotid glands. This sparing of the OAR allows up to 80% of patients to retain salivary function for a greatly increased quality of life[142, 157, 181].

Second, the PTV dose can be increased while keeping PRV dose at similar levels. Known as dose escalation, this strategy is used to improve the local control in prostate cancer patients by 10%[134] without noticeable increase in toxicity[140]. In another example, positioning patients using kV CBCT led to a 42.3% reduction in PTV volume and significant reduction in OAR dose for IMRT treatments of cancer spinal metastases[63]. A review of 61 comparative studies of IMRT vs non-IMRT 3DCRT treatments in a large number of anatomical sites found that most IMRT treatments led to better local control or management/prevention of toxicity[157]. This is presumably due to the increased conformality and accuracy of IMRT treatments compared to 3DCRT. Radiation therapy techniques of even greater complexity than IMRT such as VMAT and ART are also expected to either increase control or reduce patient side-effects. Unfortunately, with some highly-conformal treatment modalities comes a greater risk of geometrical miss of the PTV and therefore loss of the therapeutic benefit of the treatment[33, 34].

IGRT protocols, including the site, the frequency and the modality, vary from clinic to clinic. For instance, in our clinic we only use MV and kV orthogonal imaging for position verification patients in most treatments, while kV CBCT is used in hypofractionated stereotactic treatments such as lung SBRT or brain metastases stereotactic radiosurgery. Radiographic kV imaging is used where available, and MV imaging is used otherwise on most sites. Where matching to bony landmarks is not possible (e.g., lung, see 1.2.2), kV CBCT is used for additional soft-tissue contrast. Typically, verification imaging is performed for the first three days of the treatment and only repeated if inter-fractional shifts exceed 4 mm. Patients exhibiting inter-fractional shifts exceeding 3 mm and those treated with SBRT undergo daily imaging. However, other radiation oncology clinics use considerably more imaging during IGRT, for instance performing kV CBCT on all prostate patients on a daily basis.

Uses of IGRT: Verification imaging

To safely reduce margins, the exact location of the tumour must be known at the time of treatment with greater precision than that permitted by skin tattoos and immobilization techniques alone[175, 178]. Despite immobilization, patient setup varies between fractions due to external (e.g., skin) or internal (e.g., organs) motion during a full course of radiation therapy[175]. IGRT techniques are used to image the patient in the treatment position immediately before receiving their daily fraction. This allows us to either match bony landmarks to reference image projections[178], or to localize the tumor directly by soft-tissue volumetric imaging or with fiducial markers[159]. For instance, kV CBCT can be used to match the position of the diaphragm during liver SBRT[29]. These techniques allow either the position of the patient or the field to be altered, eliminating most (but not all) of the geometric uncertainty due to inter-fractional motion[175, 63, 102, 21].

EPID portal imaging was the first modality to be used for verification imaging, but kV 2-D imaging is functionally equivalent. The 2-D image is compared to a reference 2-D projection from the planning CT image for the same location. Radiation therapists can alter the patient's position to match either the bony landmarks or surgically-implanted internal fiducial markers of the patient. Since the position of bones and fiducial markers often relate more accurately to tumour position than do skin markings, the position of the target can be verified with greater[40, 118, 135, 173].

Radiographic 2-D imaging can be used to position patients but has difficulty detecting positional errors caused by tumour rotation. These can induce dosimetrically significant errors caused by patient positioning[69, 67]. Moreover, matching the position of the bony landmarks to reference images is only helpful if the tumor is fixed or immobile compared with these landmarks, which is not true in every site (e.g., lung, liver, prostate)[21]. Finally, some sites (e.g., prostate) require better soft-tissue contrast to locate the target.

In contrast, CBCT imaging provides 3-D localization of the treatment site. As for planar

IGRT approaches, volumetric CBCT images can either be taken using the MV beam and EPID[141], or using a dedicated kV CBCT imaging unit mounted orthogonally. Of these modalities, kV CBCT offers better soft-tissue contrast and better image quality allowing the identification of some soft-tissue tumors during verification imaging[86]. Finally, phase-matched DTS provides 4D information about fraction-specific intra-fractional tumor motion. This can allow better tumor localization in sites affected by respiratory motion[155, 192].

Uses of IGRT: Tracking volumetric changes

IGRT techniques in verification imaging provide a wealth of 2-D (portal imaging, kV radiography), 3-D (CBCT, 3D DTS), and/or 4-D (phase-matched DTS/4D CBCT) images. These images of the PTV, OAR, and ITV are useful for other purposes than verification imaging. One of these is to incidentally track inter-fractional volumetric changes in the patient. The volume and location of the PTV can change drastically during treatment due to tumour shrinkage or patient weight gain/loss. This means that even if the patient positioning is reproduced identically, a geometric miss can occur if the tumor location changes. Alternatively, the OARs may receive unnecessary dose if a tumour that has shrunk significantly continues being treated with the planned field sizes. Tracking the changes in anatomy can also indicate when a patient needs to be re-planned.[178] The newly developed 4D DTS kV CBCT method can also track inter-fractional ITV changes.

Uses of IGRT: Real-time tumor tracking

As we mentioned previously, some tumors are located in areas highly affected by respiratory motion such as the liver or the lung[150]. Even the prostate can experience intra-fractional motion of up to 24 mm due to the respiratory cycle, bladder filling and—more importantly, if treated prone—movement of the bowels[101].

In slow CT scans, the patient can breathe normally during acquisition (allowing imaging of the whole breathing cycle in each slice), and the full extent of the tumor motion is contoured as the ITV (see Fig 1.3). If treated in free breathing, a larger volume including more healthy tissue receives the full treatment dose. Alternatively, breath-hold techniques can be used to image and treat the tumor during a specific phase of the respiratory cycle, but it can be difficult for patients to hold their breath for extended periods of time and in a reproducible manner. Simulation using a time-correlated CT scan (4DCT) can track the real-time position of the tumor[57]. Radiation treatments can be planned to irradiate the tumour in a specific stage of the respiration cycle—respiratory-gated radiation therapy. To deliver gated radiation therapy, one must know the position of the tumour in real time during treatment. The simplest and most commonly used method to achieve this is tracking the external motion of a suitable surrogate, and correlating its position with the tumour position based on the planning 4DCT. However, internal motion is quite complex and can be very different than what external surrogates predict[38]. Phased-matched DTS is a proposed method to verify the correlation of internal motion with the planning 4DCT, but it is not yet in clinical use[155].

By imaging the patient during treatment delivery using continuous 2-D fluoroscopic kV x-rays, the tumor's exact position can be determined. This can be done by using implanted fiducial markers or by soft-tissue identification, similar to verification imaging[38, 37]. Knowledge of the tumour position in real-time makes two techniques possible[125, 96, 38]: activating the beam only in a specific phase of the respiratory cycle (gating), or moving the beam to follow the tumour (tracking)[104, 38]. Gating and tracking can shrink the ITV margins with the benefits discussed previously. On the other hand, continuous fluoroscopy during the treatment represents the most dose-intensive imaging technique in all IGRT techniques[126]. At the time of writing and to the best knowledge of the author, the only published data on the accrued imaging dose delivered by fluoroscopy-guided gated treatments is the measured

air-kerma (kinetic energy released per unit mass) rate at various distances from the imaging unit[150, 149].

Unlike kV CBCT, the patient-specific 3-D dose distribution deposited by kV real-time tracking fluoroscopy is not currently the subject of theoretical investigations like Monte Carlo simulations. Estimating the absorbed dose accrued by fluoroscopy techniques is very difficult because linac manufacturers do not currently track or display the fluoroscopy exposure delivered by their kV imaging devices. While it is relatively simple to characterize the dose-rate at the skin from fluoroscopic imaging, the radiographic exposure values (i.e. kVp and mAs)— and therefore the absorbed dose—will depend on a number of patient-specific factors. These include the treatment time, the distance between the imaging unit and the skin, and the number of fields. *In vivo* skin measurements are technically possible, but complicated by the measurement of scattered therapeutic x-rays. The energy-dependence of most point-dosimeters make a real *in vivo* evaluation difficult, so an anthropomorphic phantom must be used instead. Unless commercial linacs can track and display the imaging exposure, the estimation of the patient-specific absorbed dose and risk will continue to depend on problematic in-air dose-rate estimates.

Uses of IGRT: Adaptive radiation therapy using CBCT

We have discussed how daily volumetric imaging of the patient could be used to re-plan the patient if the target volume changes drastically compared to simulation CT images. In this case, the patient would usually be sent back to be re-imaged in the simulation CT scanner. A new radiation therapy plan would be then be devised. However, this approach is only practical for infrequent and drastic changes in the anatomy of the target or the patient. If the shape of the target changes moderately but appreciably between fractions, it is impossible to correct for it by re-positioning the patient alone[41, 71].

ART techniques are currently under investigation to address this issue. ART recognizes

13

that patients do not receive the exact planned treatment dose because their position and anatomy change between each fraction[185]. In online ART, the IGRT volumetric information acquired before treatment is used to optimize the IMRT fluence maps on the spot. The plan is modified to deliver the optimal treatment in every fraction[39, 186]. In offline ART, the volumetric information is acquired over a certain period ($\sim$five days) and used to assess the patient-specific setup reproducibility. This allows the radiation dosimetrist to adapt the radiation therapy plan by adjusting the PTV margins (Fig. 1.3). Actual dose delivered is closer to the desired dose for the subsequent fractions[188].

Even if ART techniques are used to optimize the treatment fields and fluence maps, the actual dose delivered to the PTV and OARs can be different than originally planned. In dose-guided radiation therapy (DGRT), the setup-specific delivered dose to PTV and PRV is computed for every fraction. The radiation therapy plan is adapted by increasing or decreasing the delivered dose in subsequent fractions. This ensures that the patient receives the exact prescribed dose[158]. DGRT is possible since daily volumetric imaging provides the Hounsfield Unit (HU) information similar to that of a simulation CT scanner and can be used in the TPS to compute the fraction-specific dose[35, 147, 36, 174]. The imaging can be performed either using MV[165, 164] or kV CBCT daily imaging[189, 48]. If imaging with MV x-rays, the imaging dose can be routinely included as part of the treatment plan [174, 2] for even more precise DGRT/ART. In both cases, issues of lower image quality due to MV photons and increased scatter mean that CBCT imaging will deliver more dose than radiographs or conventional CT scanner.

Conclusions

We have seen that IGRT techniques make the safe delivery of modern high quality radiation therapy possible. These high quality plans allow margin reductions made possible by 2-D or 3-D verification imaging, or by real-time tumour gating or tracking. Furthermore,

IGRT can provide radiation oncology specialists with valuable volumetric information. This information can be used either to track anatomical changes, or to implement ART. The development of ART techniques are promising, but ART is not yet commonly used in radiation therapy clinics. Proposed ART techniques are impossible to implement without volumetric imaging—presumably acquired using a linac-integrated kV CBCT.

Thus, it is clear that current trends in the radiation therapy industry call for increasing use of imaging. As we move towards more specialized and personalized treatments, we require more information and deliver more imaging dose. As these techniques become more common, the absorbed radiation dose deposited in patients by imaging procedures will increase with time. This is unless or until a suitable and practical non-ionizing alternative is developed[158]. It is thus the responsibility of the medical physics community to assess and minimize the additional risk posed by these imaging procedures[126, 158].

1.1.3   Imaging dose: Associated risks

In the last section, we described the various IGRT techniques and their clinical benefit. However, any amount of radiation dose deposited in a patient's body presents a certain risk which needs to be balanced against the procedure's benefit. This subsection outlines the main risks involved with daily imaging, namely deterministic morbidities and stochastic radiation-induced cancers.

Deterministic risks of imaging dose

Historically, the considered risk arising from imaging dose has concerned long-lasting fluoroscopy. These could deliver enough dose in one sitting to cause deterministic effects such as eye cataracts and skin reactions (Table 1.2)[80, 126, 122]. There have been about 200 incidents[146] where long interventional fluoroscopic imaging has delivered enough dose to cause acute[161, 151, 180, 18, 179, 146] or chronic[31, 110] harm in patients.

Studies estimate a maximum absorbed dose of roughly 1–1.5 Gy in soft tissues arising from the cumulative imaging in IGRT treatments[126]. Due to cell repair in between fractions, the biologically equivalent dose (BED) is reduced compared to the single-fraction imaging dose in intervention fluoroscopy[68]. Therefore, the doses delivered by verification imaging in many fractions are generally not large enough to cause deterministic effects on their own.

Table 1.2: Deterministic effects caused by fluoroscopy.

Effect	Threshold
Early transient erythema	2 Gy
Temporary epilation	3 Gy
Main erythema	6 Gy
Permanent epilation	7 Gy
Dermal necrosis	15 Gy
Eye lens opacity (detectable)	> 1 Gy
Cataract (debilitating)	> 5 Gy

Values from ICRP 85[80].

Unlike historical uses of imaging, patients undergoing IGRT are exposed to very high concomitant therapeutic doses[126]. The risk of deterministic effects to the OARs is usually assessed based on the dose delivered by the therapeutic MV beam alone. Because the imaging dose in IGRT is significant (1-2 Gy), there is a danger that it may push the dose to the OAR beyond tolerances, especially if the reduction in margins permitted by IGRT is used to escalate the treatment dose. For this reason, informed decisions regarding treatment planning should include the non-negligible contribution of the imaging component of the dose[126, 3]. Details on organ specific morbidities and complications are found in the QUANTEC database[116].

Stochastic risks of imaging dose

In radiation protection, the Linear No-Threshold (LNT) model holds that there is no level of radiation exposure too low to cause additional risks. There is some evidence that the LNT

model is not valid. To estimate these risks, we use the life-span study of the excess relative risk (ERR) of cancer incidence or mortality to the atomic bomb survivors of Nagasaki and Hiroshima, as well as a multitude of smaller population studies. These estimated risks to the general population are based on the assessed doses absorbed in the whole body of the atomic bomb survivors; to estimate the ERR, it is necessary to scale the absorbed dose in an individual to a whole-body dose which would cause the same ERR. This effective dose E is obtained by summing the effects of the average absorbed doses $\bar{D}_i$ in the total N of irradiated organs and tissue using the following expression[97]:

$$E = \sum_{i}^{N} w_R \cdot w_{T,i} \cdot \bar{D}_i, \tag{1.1}$$

where w_R and w_T are weighting factors for the radiation and tissue, respectively. For the low-energy x-rays of CT imaging, the w_R is usually assumed to be unity. Recent investigations suggest that low-energy x-rays might cause more damage per unit energy released, as their radiation biological effectiveness has been estimated at 1.1[100]. Therefore, using a $w_R = 1$ might underestimate the ERR caused by low-energy x-ray imaging procedures.

There is currently no epidemiological evidence that the LNT model is accurate at low doses[169, 143, 72]. In the absence of a suitable alternative model, the LNT represents a conservative risk estimate for the incidence of lethal cancers. For this reason, the Committee on the Biological Effect of Ionizing Radiations (BEIR) V and VII recommend that the LNT model continue to be applied to estimate the risks posed by x-ray imaging[15, 16, 148]. While much work has been made applying the BEIR VII recommendation to estimate the stochastic risks associated with conventional CT imaging[75], comparatively few studies estimate the risks associated by kV CBCT imaging. One exception is the work of by Kim *et al.* who studied the cumulative effective doses delivered by a full course of IGRT CBCT procedures. By calculating the effective dose to a variety of patients, they determined that the imaging dose would cause an excess of 400 cancer cases per 100, 000 patients[98]. This

represents approximately 70% of the empirically estimated risk of secondary cancers from the therapeutic dose. At first glance, this means that the CBCT dose is almost as likely to cause secondary cancers as the radiation therapy course. According to the authors, this is because the high therapeutic dose in the PTV induces more cell-killing than the carcinogenic faulty DNA repair[98]. However, because much of the imaging dose is also absorbed in the PTV, simple use of the ERR is probably not an accurate description of the real stochastic risk caused by kV CBCT IGRT procedures.

The current methods for estimating the effective dose and the ERR are based either on homogeneous or anthropomorphic phantom measurements (see section 1.2.1). The medical physics community continues to debate their ability to accurately estimate the effective dose[27, 28]. Monte Carlo simulations can be performed on a patient-by-patient basis such as done by Ding *et al.*[44] or Kim *et al.*[98] (see section 1.2.2). Unfortunately, currently-available Monte Carlo simulation packages are time-consuming and require specialized training. There is thus room for the development of a more clinically feasible tool.

Pediatric patients

In the previous subsections, we discussed the risks associated with imaging dose concerning the general population. Pediatric patients receiving ionizing radiation experience the same kind of risks as the general population, but are affected on a much greater scale. Studies estimate that children are up to ten times more susceptible than adults to secondary cancer induction by ionizing radiation[15, 26]. Some of the factors that increase radiation sensitivity in pediatric patients include a much longer lifetime for a radiation-induced cancer to develop, and the proportion of fast-growing tissues. Furthermore, CT imaging protocols have historically been poorly optimized for the smaller bodies of children and therefore may deliver unnecessary dose[132]. To reduce the additional risk, IGRT imaging procedures should be optimized for pediatric patients[58].

A recent long-term population study of Australian children and adolescents shows that children who underwent diagnostic CT imaging procedures were 25% more likely to develop a cancer in the 10 next years than the control cohort, representing an excess 9.3 cancers per 100 000 pediatric patients[117]. The risk of developing a radiation-induced cancer was commensurate with the number of imaging procedures (more dose meant more risk), the imaging site (correlation between induced cancer and imaging site), and age (cancer more frequent in young patients). While CT imaging during the study period (1985-2005) delivered doses greater than current diagnostic CT protocols, daily IGRT over 20–30 fractions would deliver much greater effective doses than received by the imaged cohort. For this reason, medical specialists should be extremely judicious when choosing to use IGRT techniques to treat young children. Proper assessment of the risk associated with the imaging dose is more crucial when pediatric patients are concerned.

The medical community is well aware of these risks. Indeed, the Image Gently campaign was started in 2008 to sensitize medical professionals to the risk posed by radiation dose in children. The goal is to induce the use of alternatives to ionizing-radiation imaging, and to suggest many strategies reducing the radiation dose from imaging procedures.[52, 10]. One of these strategy is to attempt to move towards low-dose CT scans. While these protocols provide images of lower-quality, up to 55% of the dose can be lowered while the quality remains acceptable for diagnostic purposes[130].

1.1.4 AAPM Task Group 75 recommendations

In 2007, the American Association of Physicists in Medicine (AAPM)'s Task Group 75 (TG-75) released a report on the management of imaging dose during IGRT. The report underlines the importance of evaluating the doses incurred from IGRT because they are concomitant with large therapeutic doses. The task group argues that this additional imaging dose represents two potential health hazards: stochastic and deterministic effects potentially

incurred by the patient. The imaging dose should be kept as low as reasonably possible following the spirit of the "as low as reasonably achievable" (ALARA) principle used in radiation protection[127]. Furthermore, the task group suggests that the benefit of every imaging procedure be weighted against the potential risks for each patient.

The task group recommends a three-step approach to achieve this goal: (1) assessment, (2) reduction and (3) optimization. First, the distribution of the dose throughout the patient must be assessed correctly (1). It is only then we can make informed decisions to refine the imaging technique and reduce dose (2). It becomes possible to think of the imaging dose as not an unwanted additional dose, but as part of the treatment dose. This dose that can be optimized (3). This allows us to make the best use this imaging dose and obtain the highest quality treatment plan for the patient.

1.1.5 Conclusions

In this subsection, we described modern IGRT techniques and their clinical rationale: the safe reduction of margins in radiation treatment plans by verification imaging, patient repositioning, tumor tracking or gating, and adaptive radiation therapy. We also explained the various risks that are introduced by the additional imaging dose delivered by IGRT procedures. These risks are not routinely assessed or taken under account by radiation oncology specialists. It is clear that the assessment of the patient absorbed dose delivered by IGRT techniques figures as one of the main steps in achieving the AAPM's TG-75's recommendations. In the following subsection, we will describe existing and proposed IGRT imaging dose assessment techniques.

1.2 Existing methods for evaluating kV CBCT dose

Following the AAPM's Task Group 75 recommendations, the first step in assessing the risk posed by kV CBCT imaging techniques is evaluating the 3-D distribution of absorbed dose they deposit in patients[126]. This subsection outlines the advantages and shortcomings of existing and proposed kV CBCT imaging dose assessment techniques.

1.2.1 Experimental estimation of kV CBCT dose

Experimental measurements represent the simplest and most straight-forward way to estimate the absorbed dose accrued to patients through kV CBCT techniques. The current industry-standard CT and CBCT dose estimation method is the CT Dose Index (CTDI). The CTDI is a relatively simple measurement performed in a cylindrical homogeneous phantom; it approximates the mean dose to the patient delivered by a CT imaging procedure.

Other experimental methods are more direct. They either measure the patient skin dose, or estimate the internal patient dose by anthropomorphic phantom phantoms. The dosimeters used to achieve this for kV CBCTs include thermoluminescent detectors (TLDs) and dosimetric radiochromic films. In this subsection, we explain their properties and the theoretical basis behind their use in kV dosimetry.

CT Dose-Index and associated values

The CTDI was originally proposed by Jucius and Kambic[93] and introduced by Shoppe *et al.*[152] In its many forms, and along with the dose-length product (DLP), it is currently the legal standard used to estimate and regulate the dose deposited by CT imaging devices[120, 76]. Since CBCT is a subset of CT, quality control and dose estimations were first performed using CTDI.

In CT, the patient is imaged in a series of small slices each depositing dose in the body. While we cannot practically measure the internal dose in a patient, we can measure it in a phantom. CTDI phantoms are homogeneous cylinders, usually of acrylic (also called Polymethyl methacrylate, or PMMA). They come in two sizes: the head and body CTDI phantoms with diameters of 16 and 32 cm, respectively.

The dose is estimated by the CTDI in the middle slice along the longitudinal axis of the phantom. If the phantom is imaged with a CT procedure, each successive slice contributes to the absorbed dose in this central slice. However, the contribution of slices farther away becomes less important and eventually negligible. This leads to a maximum dose value if imaging procedure is infinite, called the multiple slice dose average (MSDA, Fig.1.4).
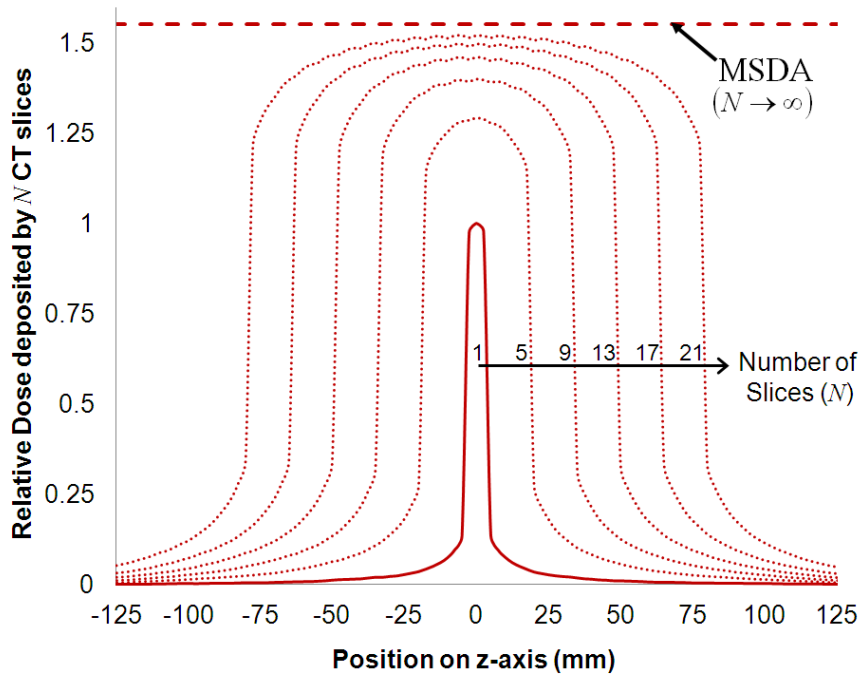
Figure 1.4: Relative dose deposited by a number N of CT slices of thickness and separation I=5 mm along the longitudinal z axis of a cylindrical phantom. As N increases, scatter from the additional slices contributes to the dose at the centre of the phantom until it reaches a theoretical maximum value, the MSDA. This value is mathematically analogous to the more easily measurable CTDI. These profiles were generated using kVDoseCalc and are meant to represent the MSDA concept, and are not necessarily representative of a real CT scanner. The dose is normalized to the maximum value of one slice.

The MSDA is expressed by the following equation:

$$\text{MSDA} = \frac{1}{I} \int_{-I/2}^{+I/2} D(z) \, \mathrm{d}z, \tag{1.2}$$

where I represents the distance between slices and D(z) the dose at various points along the longitudinal (z) axis. The MSDA represents the dose deposited by all CT slices integrated in the width of a single, central slice (-$I/2$ to +$I/2$). Since it theoretically represents the dose actually deposited by CT in the phantom, the MSDA should be the quantity of interest. The MSDA can technically be measured using a point dosimeter. However, point dosimetry poses practical problems compared to ionization chamber dosimetry so the CTDI was introduced instead to estimate the MSDA. CTDI is meant to measure the total dose deposited by a single CT slice irradiating the centre of the phantom. The dose in one point delivered by an infinity of slices (MSDA) can be shown to be mathematically equivalent to the total integrated dose delivered by a single slice (CTDI, Fig. 1.5).

The CTDI is defined by the following equation

$$\text{CTDI} = \frac{1}{nT} \int_{-\infty}^{+\infty} D(z) \, \mathrm{d}z, \tag{1.3}$$

where nT represents the effective slice thickness in a multiple-slice CT scanner. In a single-slice scanner, $n = 1$ and the thickness is simply T. The dose ($D(z)$) along the longitudinal z axis is integrated to yield the CTDI. Since integrating from $-\infty$ to $+\infty$ is not practically possible, the CTDI_100 is measured using a long (10 cm) 100cc pencil-type ionization chamber. Using the approximation that the mean path-length of the scattered photons is small compared to the length of the ion chamber, $D(z)$ goes to zero within the integration bounds ($-50\,\text{mm}$ to $+50\,\text{mm}$). We therefore obtain

$$\text{CTDI}_{100} = \frac{1}{nT} \int_{-50\,\text{mm}}^{+50\,\text{mm}} D(z) \, \mathrm{d}z. \tag{1.4}$$

$$MSDA = \frac{1}{I} \int\limits_{-I/2}^{+I/2} D(z)\mathrm{d}z$$

$$CTDI = MSDA$$

$$CTDI = \frac{1}{nT} \int\limits_{-\infty}^{+\infty} D(z)\mathrm{d}z$$
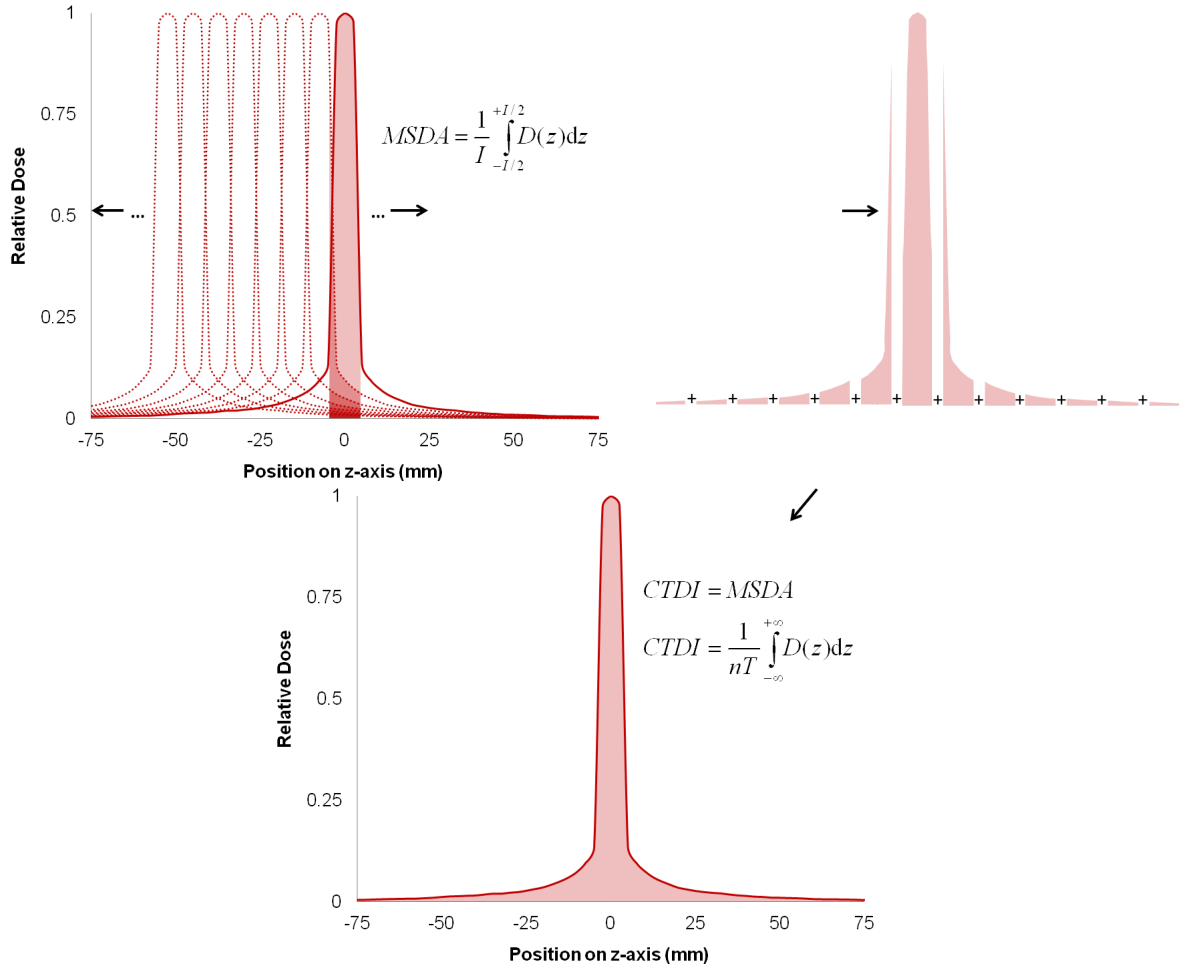
Figure 1.5: Relationship between the MSDA (top left) and the CTDI (bottom). A succession of $N \to \inf$ CT slices are integrated along a small (-$I/2$ to +$I/2$) area to compute the MSDA. This is mathematically equivalent (top right) to integrating the total dose deposited by a single slice. In either case, the same single-slice dose distribution $D(z)$ is normalized to a maximum value of 1, as in Fig. 1.4

The CTDI$_{100}$ has since become the standard of CTDI measurement, but the base assumption—that all of the scattered and primary dose are collected by the 100cc ionization chamber—is not true for many CT imaging protocols. Indeed, Boone has shown that for CT slices of 10 mm width, as little as 63% of the total dose was collected by the central CTDI$_{100}$ in a body CTDI phantom[23]. This is because scatter inside the phantom deposits up to 37% of the dose outside the 10 cm of the ionization chamber. The values were practically unchanged for relatively large 40 mm slices. The implication is that the relatively easily-measured CTDI$_{100}$ is not adequately assessing the patient absorbed dose for CT protocols for which it was designed.

This CTDI$_{100}$ can be theoretically measured anywhere in the phantom. However, the CTDI$_{100}$ value will change between the periphery and the centre as photons are increasingly scattered with depth. To address this issue, Leitz *al.* introduced the weighted CTDI (CTDI$_w$) representing the average CTDI$_{100}$ with a single value[107]. The CTDI$_w$ is obtained by measuring the CTDI$_{c,100}$ and the CTDI$_{p,100}$ in the centre and the periphery of the phantom, respectively (Fig. 1.6). Peripheral measurements are performed at a distance of 1 cm from the edge of the phantom. The number of peripheral locations is usually 4, but sometimes 8[1], and they distributed at equal angles. The CTDI$_w$ is calculated using the following expression

$$\text{CTDI}_w = W_c \cdot \text{CTDI}_{100,c} + W_p \cdot \frac{\left[\sum_{i=1}^{N} \text{CTDI}_{100,p}^i\right]}{N}, \qquad (1.5)$$

where W_c and W_p are weighting factors for the central and peripheral CTDI$_{100}$, respectively. Leitz *et al.* obtained values of W_c=2/3 and W_p=1/3 by making two assumptions: a linear dose decrease between the periphery and the centre, and a negligible dose outside the nominal slice thickness. These are currently widely used to calculate the CTDI$_w$. A more rigorous theoretical treatment by Bakalayar found that W_c=1/2 and W_p=1/2 are values which more closely approximate the real value of the average CTDI[12]. Kim *et al.* have confirmed that

the Bakalyar factors yield slightly better agreement with Monte Carlo simulations for CT and CBCT imaging procedures[99].
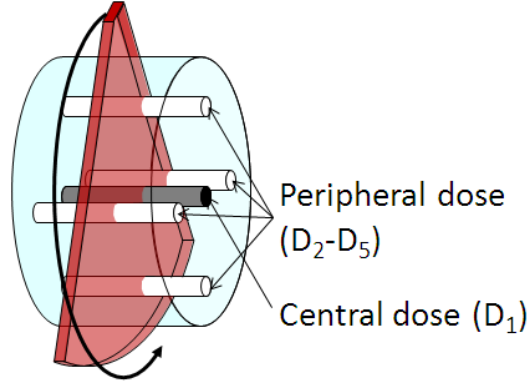
Figure 1.6: Positions where the CTDI_{100} is measured to obtain the CTDI_w.

The CTDI_w gives the average dose deposited by a CT imaging procedure if the effective slice thickness nT is equal to the slice separation I. This is usually true in axial scanners, but in helical scanners the bed moves continuously as the patient is imaged. The pitch p represents the relative speed of the rotation with regards to the couch motion. It is represented by the ratio between the distance between slices I and the effective thickness nT, $p = I/nT$. The volumetric CTDI (CTDI_{vol}) gives the average local absorbed dose when $p \neq 1$, and it is defined by[120]

$$\text{CTDI}_{vol} = \frac{nT}{I} \times \text{CTDI}_w = \frac{1}{p} \times \text{CTDI}_w. \tag{1.6}$$

Up to now, every CTDI has been an estimate of local absorbed dose in a homogeneous phantom. This local absorbed dose can be used to assess deterministic effects, but cannot estimate the stochastic risk. As we saw in section 1.1.3, risk estimates on individual and population levels are made using the effective dose. Because it assumes an irradiation to the whole body, the conversion from CTDI to effective dose is not trivial. First, a value proportional to the irradiated volume, the dose-length product (DLP), is calculated as a surrogate[77]. The DLP is defined by[120]

$$\text{DLP} = \text{CTDI}_w \times L, \tag{1.7}$$

where L represents the scan length. The effective dose can finally be calculated[107] using

$$E = \sum w_R \cdot w_t \cdot \bar{D} = \text{DLP} \times w_{\text{DLP}}, \tag{1.8}$$

where w_{DLP} are site-specific weighting factors. In principle, if the 3-D distribution of the dose was known in a certain patient, the average dose in each organ would be calculated and multiplied by the relevant tissue weighting factors. In practice, it is very difficult to estimate the organ dose from the CTDI_w or DLP[120]. Instead, the International Commission on Radiation Protection (ICRP) publications 26, 60, and 103 provide convenient site-specific DLP-to-E conversion factors[78, 79, 81]. Lee *et al.* also calculated these factors for patients of different ages and sex to estimate the effective dose to pediatric patients[106]. The CTDI can thus estimate the local absorbed dose (CTDI_w, CTDI_{vol}) and stochastic risk (DLP, E) caused by a CT imaging procedure.

Limitations of CTDI-based dose estimation techniques to CBCT

There are three main limitations to using the CTDI and its associated quantities (CTDI_{100}, CTDI_w, CTDI_{vol}, DLP) to assess the absorbed dose delivered to patients by kV CBCT imaging procedures.

First, CTDI measurements assume the acquisition of the dose from the entire CT slice. This is usually performed using a 10 cm ionization chamber, but many CBCT fields are larger than 10 cm. This means that it is impossible to acquire the entire primary dose from the CBCT, let alone the scattered components.

Second, CTDI values were created for scans with 360° arcs where the dose distribution throughout the body was nearly homogeneous. In contrast, CBCT imaging procedures can be performed with partial arcs. For instance, two of the default Varian® OBI® 1.4 CBCT

procedures have arc sizes of only 200°. These partial arc imaging techniques are designed to reduce the OAR dose[162] such as to the eyes in head imaging protocols. The use of the CTDI for CBCT imaging procedures of arc $\leq 360°$ estimates a very heterogeneous dose distribution by a single value over the entire patient or phantom volume. A medical practitioner relying on CTDI to make informed decisions concerning deterministic risks from the combination of treatment and CBCT imaging dose would therefore greatly overestimate or underestimate the deterministic risk contributed by the CBCT imaging dose.

Third, CTDI values are measured in standard phantoms, namely of 16 cm and 32 cm diameters for the head and body respectively. These reference sizes only provide patient dose estimates for a single geometry. In fact, patient geometry can vary tremendously, especially in pediatric patients. As we show in Chapter 4, $CTDI_w$ measured in reference geometries underestimate the local absorbed dose by a factor of 2 in an anthropomorphic phantom simply due to differences in diameter. To follow the recommendations of the AAPM Task Group 75, we require a patient-specific risk-assessment tool. Unfortunately, to use the CTDI to compare imaging protocols is to discount patient size-dependence.

The first of these limitations can be solved by adapting existing CTDI methodologies. One proposal is to use a longer phantom (35 cm) and ionization chamber (30 cm) to measure the $CTDI_{300}$. This $CTDI_{300}$ is conceptually identical to the $CTDI_{100}$ except for the much longer integration volume[123, 59], allowing the acquisition of more scattered photons. Unfortunately, the enlarged phantom is quite heavy ($\sim$35 kg) and hard to handle. Alternatively, Dixon proposed the "point-dose" CTDI estimation method. In this method, the dose is measured in a small volume in the central slice of a phantom exposed to a long CT scan, as opposed to a single slice[51]. This new method is functionally identical to the original MSDA. Kim *et al.* and Descamps *et al.* have since successfully used it to estimate the $CTDI_w$ of CBCT protocols[99, 42]. The method has also been suggested as an official replacement of the $CTDI_{100}$ by the AAPM's Task Group 111's comprehensive methodology on the evalu-

ation of the radiation dose in x-ray CT[1]. The point-dose method was also used successfully by Li *et al.* to measure the average absorbed dose, equivalent to the $CTDI_{vol}$[109].

These proposed technical adaptations of the CTDI methodology solve the first limitation, but not the second and the third. A single CTDI value cannot estimate the spatial distribution of the dose and allow a practitioner to make informed decisions concerning deterministic risks posed by CBCT imaging. Even if it did, the CTDI would still be specific to a single geometry. It would be very difficult—if not impossible—to further adapt the CTDI methodology and provide patient-specific risk accrued from CT and CBCT imaging. The CTDI and DLP remain useful tools to provide rough estimates of population doses from CT imaging. Unfortunately, they cannot fulfill the objectives set out by the AAPM's Task Group 75 on the management of imaging dose. For this reason, there has been significant debate concerning the CTDI. There has been pressure to move away from CTDI-related surrogates of patient dose to the benefit of anthropomorphic phantom measurements or patient-specific dose computation[27, 28].

1.2.2 *In vivo* measurements

The various CTDI measurements provide an estimate of the CT dose that is not patient-specific. In this subsection, we present various *in vivo* dose measurement techniques that can be used to measure the patient-specific dose deposited by kV x-rays in general, and imaging in particular.

Thermoluminescent detectors

TLDs are a type of integrating detector which measure accumulated dose[11]. They are composed of an ionic-bound lattice compound doped with impurities. At room temperatures, the lattice acts as an insulator. The impurities cause imperfections in the lattice; these impurities serve as electron traps (Fig. 1.7). When irradiated, a number of electrons

proportional to the absorbed dose are excited to the conducting band and settle in the electron traps. Upon thermal re-excitation, the trapped electrons emit a photon of energy equal to the gap between the valence and conducting energy band. These photons can be measured using a photomultiplier tube (PMT). The total charge collected by the PMT is proportional to the number of trapped electrons and, consequently, to the absorbed dose. The relationship between absorbed dose and PMT reading can be quality-dependent[55], so the TLDs have to be characterized for each beam quality. The most prevalent clinical TLD is lithium fluoride (LiF), typically doped with magnesium (Mg) and titanium (Ti) to form TLD-100. However, different concentrations of dopants have been shown to radically change the dosimetric properties of the TLD[55].
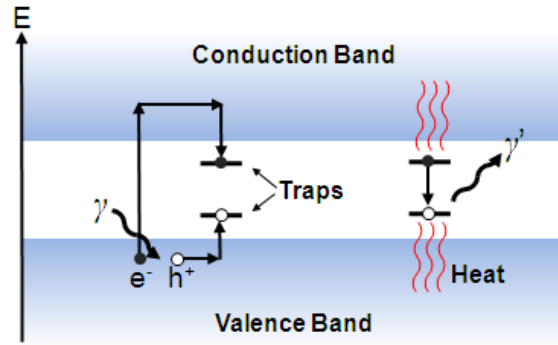
Figure 1.7: Description of a TLD. The incident radiation (γ) ionizes an electron-hole pair (left) until both the hole (h$^+$) and the electron (e$^-$) are trapped in electron traps caused by crystal impurities. The application of heat (right) excites the electron-hole pair until they recombine, emitting a photon (γ') that can be measured via a PMT.

Because of their powder form, TLDs can take on any shape or size. They are therefore of special interest in measuring point-dose in very small volumes, such as on the surface of a patient for *in vivo* dosimetry, or inside an anthropomorphic phantom such as RANDO® (The Phantom Laboratory, Salem, NY USA).

In vivo skin dose

TLDs are ideally suited for *in vivo* patient skin dosimetry due to their small size, integrating nature and relatively low energy dependence. Wen *et al.* used thermo-luminescent detectors (TLDs) to estimate dose from Varian® OBI® CBCT procedures[182]. TLDs were positioned on seven prostate patients imaged via CBCT. Skin doses ranged from 2.6 to 6 cGy per scan, depending on patient size and imaging beam parameters. Likewise, Marinello *et al.* performed *in vivo* dosimetry on patients undergoing Varian® OBI® 1.3 using TLDs and found that skin doses varied from 5.8 to 7.3 cGy, depending on position and patient size[115]. Using TLDs like this provides a good *in vivo* estimate of the patient-specific skin dose, but does not provide measurements of the variable dose within the irradiated volume. Therefore they cannot be used to assess the deterministic risk of morbidities to the OARs or the stochastic ERR.

Anthropomorphic phantom organ dose

There exist a number of anthropomorphic phantoms such as the RANDO® (The Phantom Laboratory, Salem, NY, USA) or the Alderson (Radiation Support Devices, Long Beach, CA, USA) phantom suitable for estimating organ dose depositing by kV CBCT procedures. These phantoms typically comprise tissue and lung-equivalent materials, as well as real human bones (RANDO®) or bone-simulating material (Alderson); they also typically include cavities in which a point dosimeter such as a TLD or a MOSFET can be inserted. This makes it possible to obtain point estimates of the local dose in a variety of anatomical sites in a way that more closely approximates the dose distribution inside a real patient than a CTDI phantom. These have been, for instance, measured by Palm *et al.*[131], and Alaei *et al.*[7] for Varian OBI CBCT procedures. These values can be used to compute effective doses to assess the ERR from kV CBCT procedures, as done by Kan *et al.*[94] and Dufek *et al.*[54].

There are two limitations to using anthropomorphic phantom measurements to assess pa-

tient risk from kV CBCT. The first is that the measurement process is fastidious. In general, only a few points are measured and it can be difficult to assess the mean organ dose accurately. The second is that the measured doses are specific to the size of the anthropomorphic phantom. Since the dose distribution can vary significantly with patient size and imaging geometry, anthropomorphic phantom measurements do not provide a patient-specific dose deposited by kV CBCT.

Choice of dosimeter

In this thesis, we used high-sensitivity MCP-N (LiF:Mg, Cu, P) TLDs to measure anthropomorphic internal doses in chapter 4. However, radiochromic films are alternate dosimeters that could be used for similar measurements.

Radiochromic film

Radiochromic films are a recent addition to integrating dosimeters. Radiochromic films, specifically Gafchromic^{TM} films, are self-developing, ambient light-insensitive, high spatial resolution (sub-millimeter), and highly reproducible films. They are convenient and accurate method to estimate spatial dose distributions to a much higher accuracy than conventional silver-bromide films.[43, 191, 9]

The standard quantitative dosimetric radiochromic film, Gafchromic^{TM} EBT was found by ourselves [85] (see Appendix 3) and Fletcher and Mills [56] to be appropriate for relative and absolute dosimetry of therapeutic kV beams. These radiographic films are known to have a response that is spectrum-independent at the MV range, but have not been used in the kV range until recently. The spectrum of a beam is dependent on its characteristics (i.e. accelerating potential, inherent and added filtration) and attenuation-induced beam hardening when traversing a medium. Our empirical measurements showed that the energy dependence of EBT3 was such that a beam-specific characterization (i.e. for a given

accelerating potential and filtration) was required. However, energy-corrections were not required even at large (d ≥ 15 cm) depths[85], presumably because the energy spectrum of the beam does not vary sufficiently over this distance to require corrections. Unfortunately, the sensitive dose range for EBT films is much too high (50-200 cGy) for it to be useful in the estimation of dose deposited by imaging procedures such as CBCT[136].

Gafchromic^{TM} XR-QA and XR-QA2 films include a high-Z layer to increase their sensitivity to the 2-200 mGy range[25], which makes them the only film able to estimate CBCT dose[22]. A characterization method allowing quantitative dosimetry for XR-QA2 films based on in-air kerma was developed by Tomic *et al.*[167]; this method was further investigated by Giaddui *et al.*[60] and Boivin *et al.*[22] and can be used to accurately estimate the surface and volumetric dose deposited by conventional CT [25, 144] and CBCT procedures[167, 22, 60]. However, we were concerned that the high-Z component would introduce an energy-dependence that would make measurements of the 2-D HVL unfeasible since a change in detector response of even 1% would change HVL calculation by 0.9%[64]. For this reason, we have not used Gafchromic^{TM} films to measure the dose deposited by CBCT procedures in this thesis.

TG-61 dosimetry protocols

The AAPM's Task Group 61 (TG61) provides protocols for relative and reference dosimetry for 40–300 kV x-rays. We mention these protocols because they are used to prescribe and estimate dose on the skin and at depths deposited by therapeutic x-rays. The backscatter factors used in TG61 assume a flat surface in a homogeneous phantom[111]. It should be no surprise that using TG-61 formalism to estimate doses to curved or small surfaces leads to large dose discrepancies[128]. Therefore, TG-61 formalism is useful to calibrate other dose estimation techniques via reference dosimetry, but cannot be used to accurately estimate the patient-specific dose deposited by kV x-rays. In this study, we use TG-61 protocols for

relative dosimetry to validate our approach in chapters 2 and 3, and reference dosimetry to calibrate our TLDs in chapter 4.

1.2.3 Theoretical estimation of kV CBCT dose

There exist multiple experimental methods by which the kV CBCT patient dose can be estimated. Ideally, the full patient-specific 3-D dose distribution would be required in order to satisfy the mandate set out by the AAPM Task Group 75. In this subsection, we outline the two main approaches that have been used to compute these 3-D distributions; namely, conventional Monte Carlo simulations and the adaptation of existing commercial treatment planning systems.

Monte Carlo simulations of kV beams

Monte Carlo Simulations

In principle, an ideal calculation of the dose deposited by ionizing particles would involve calculating the primary and scattered x-ray and electron fluences from first principles (e.g., using the Boltzmann transport equation). The result would be an analytical equation describing the spatial distribution of the absorbed dose. In practice, the Boltzmann transport equation is very difficult (if not impossible) to solve because it is highly specific to the specific beam and medium geometry. Primary and first-scattered events can be modeled fairly accurately, but the equations defining multiple-scatter events become increasingly more complex. Monte Carlo simulation techniques are currently the most accurate way to compute dose distributions.

In Monte Carlo simulation techniques, the beam characteristics are obtained by modeling the physical interactions from first principles. These beam characteristics are used to generate x-ray energy, position and orientation probability functions. These probability functions are then used to randomly generate the photons irradiating the medium of interest. Every

photon is randomly assigned an optical pathlength—a distance before they interact with matter—based on interaction probability coefficients and the material composition. The angle of scattering and energy imparted to the secondary particle is randomly generated from angular and energy scattering probability distributions. Every seeded photon thus deposits dose in a certain part of the phantom. This represents a particle history. Repeated over a very large number (billions) of particle histories, Monte Carlo simulations generate accurate and smooth approximations of the 3-D dose distribution expectation value.[121]

There exist many established Monte Carlo software packages which can be applied to a variety of energies and particles. In this subsection, we explain the work that has been done to model kV CBCT patient dose using Monte Carlo techniques.

Monte Carlo modeling of kV CBCT IGRT procedures

The work performed by Ding *et al.* to model kV CBCT sources using the BEAMnrc and DOSXYZnrc code packages[95] represents the most comprehensive and successful approaches to computing IGRT doses by Monte Carlo simulations. First, they successfully modeled a Varian OBI kV 1.3[46] and 1.4[45] imaging unit. Then, they computed the kV imaging dose delivered to a prostate patient during a full course of IGRT with daily kV CBCT imaging[44]. While it was found that the additional imaging dose did not push any of OAR doses beyond accepted limits for this particular patient, the imaging dose altered the OAR dose-volume histograms by 1-2 Gy. Since these imaging OAR doses are not negligible, beam-specific 3D dose distribution in the patient could be useful in making informed decisions about patient risk in different cases where the OAR dose from the therapeutic component of the treatment was higher. They calculated the dose to patients from standard CBCT procedures[47]. Their work has recently culminated in a comprehensive comparison by Ding and Munro of the imaging dose delivered to a patient by each Varian OBI imaging modality (i.e., MV portal imaging, kV 2-D radiography, and kV CBCT) per anatomical site, showing that MV imaging

delivers by far the most dose and kV CBCT delivers more dose than 2-D kV imaging[49]. These results were previously depicted in Table 1.1.

Monte Carlo simulations are also used by other teams to assess the patient absorbed dose delivered by kV CBCT. Gu *et al.* computed organ doses and effective doses in a VIP-Man (Visual photographic man) Monte Carlo phantom[66]. Downes *et al.* also characterized an Elekta XVI using BEAMPP, essentially a newer version of BEAMnrc[53]. Spezi *et al.* developed a multi-focal virtual source model (VSM) for a simpler characterization of XVI units[156] and used it to compute patient dose.

Monte Carlo simulations like the approach developed by Ding *et al.* are presumed to be the most accurate way to compute 3-D dose deposition, either through kV or MV. This presumption is based on the fact that the dose distributions are calculated from first principles. While Ding *et al.* and Spezi *et al.* have compared their Monte Carlo models against depth-dose profiles in water, they have not validated it in an anthropomorphic phantom. Instead, Ding *et al.* calculate the dose in an entirely computerized voxel phantom. These phantoms already have their tissue compositions predefined. For patient-specific dose computations, the accuracy of Monte Carlo depends on accurate tissue segmentation of the patient simulation CT image[177, 14]. Without validation of this process in an anthropomorphic phantom, it is difficult to substantiate the presumed accuracy of the Monte Carlo simulations.

In their development of a tool to assess patient-specific doses deposited by conventional CT scanners, Li *et al.* compared Monte Carlo simulations in anthropomorphic phantoms to TLD measurements: the agreement ranged from -17.2% to 13.0%[108]. Furthermore, in their validation for a convolution algorithm (see section 1.1.2), Alaei *et al.* also compared their measured and calculated dose to Monte Carlo simulations. The doses calculated by Monte Carlo show agreement with measured dose ranging from -6 to 14%.

Monte Carlo techniques require specialized tools, knowledge, and are computationally intensive. They are also considered the most accurate methods used to calculate the dose

deposited by MV x-rays, but they are not used to compute 3-D patient dose distributions due to their computation times and are perceived as clinically infeasible. While it is possible to create a end-user Monte Carlo product that avoids many of the perceived inconveniences, no such Monte Carlo product currently exists. Therefore, there is room for the development of a technique that is easier to use and implement even if not as accurate.

Convolution algorithms in commercial treatment planning systems

Another approach to computing kV dose distribution is to adapt existing commercial treatment planning systems (TPS) such as Pinnacle[3]. This only requires the use of software already available in radiation therapy clinics; it requires no specialized knowledge from the user. Furthermore, many commercial TPS allow the user to import the absorbed dose from a previous plan to the patient. Thus, it is relatively convenient to combine the dose distributions from imaging and therapy components of IGRT, as performed by van Elmpt *et al.*[174]

If it could be done accurately, adapting a TPS would be the most clinically feasible method of estimating patient absorbed dose from the kV imaging component of IGRT. To understand the limitations of adapted TPS in kV dose computations, we must first describe how TPS operate in the MV range for which they were developed.

Convolution algorithms for MV x-ray dose

Commercially-available TPS currently used for MV radiation therapy planning generally use the convolution-superposition method to compute the three dimensional dose distribution within a medium. The convolution-superposition method follows these general steps: 1) A model-based approach is used to describe the total energy released per unit mass (terma) by the primary field of ionizing particles, 2) Monte Carlo simulations calculate the energy deposition kernel which describes the dose deposited by secondary particles from a primary

37

particle interaction, and 3) the energy deposition kernel is convolved with the terma to compute the 3-D dose distribution (Fig 1.8). The energy deposition kernel is analogous to an impulse response in signal theory while the primary photon is analogous to the signal. Convolving both functions yields the total dose distribution in the patient[113].[121]

Terma
Where primary photons interact and release energy

Energy deposition kernel
Dose distribution from a single photon interaction

Dose distribution
Calculated in K-Space fast and accurately
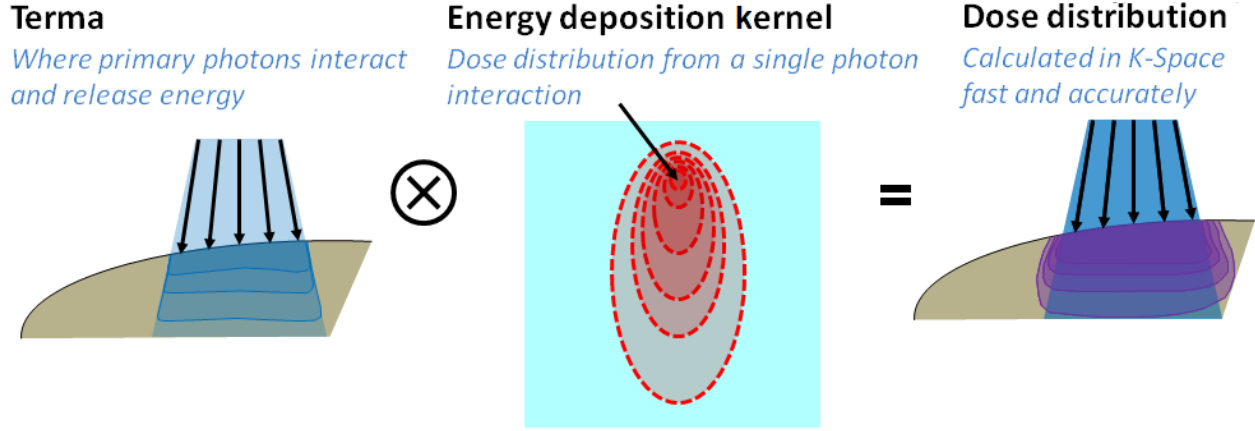
Figure 1.8: Description of the convolution-superposition dose computation method. The terma (left) is obtained by transporting the beam through the medium and describes where particles interact. The dose-deposition kernel (middle) is obtained by Monte Carlo simulations and describes where primary particle interactions ultimately deposit energy. The convolution of both (right) gives the spatial dose distribution in the medium. Terma and kerma are calculated and convolved for different incident energy ranges, the superposition of which giving the total 3-D dose ditribution in the patient—hence, convolution-superposition.

Terma

The terma is a quantity similar and related to the much more commonly used kerma, with the difference being that terma considers the total released energy as opposed to only that of charged particles. Unlike kerma, the terma includes the energy released as scattered photons. Since the total released energy is the quantity of interest, there is no need to tabulate the average energy released per interaction. For terma, $T(E, \vec{r})$, the attenuation coefficient μ/ρ is used (instead of the mass-energy absorption coefficient μ_{en}/ρ usually seen in kerma), as shown by:

$$T(E, \vec{r}) = \Phi(E, \vec{r}) E \frac{\mu}{\rho}, \tag{1.9}$$

where $\Phi(E, \vec{r})$ represents the beam fluence of photons of energy E evaluated at a position $\vec{r}$. If the beam used in the computation is mono-energetic, a single terma suffices. However, the MV x-ray beams used to treat patients are produced by Bremsstralung interaction and have a very wide spectrum. For this reason, the terma is usually calculated for different energy ranges and the convolution is performed separately for each energy. The total 3-D dose distribution is then obtained by superposing the contribution of each energy range—hence the naming, convolution-superposition.

The terma can be computed within the medium relatively easily by simple radiation transport of the primary photons through the model via exponential attenuation, as the effect of the secondary particles is already modeled through the energy deposition kernels. The diffusion of the beam due to the inverse-square law must also be taken into account. Finally, if the medium contains inhomogeneities, the radiological depth must be used to attenuate the beam instead of the simple depth. This is performed by simply evaluating the point at which the beam first intersects the medium in the CT image, and using the CT electron densities relative to water in every pixel to obtain the depth in water which would produce the same attenuation.

Energy deposition kernels

The energy deposition kernels represent the average dose distribution arising from the secondary particles released when a primary photon interacts in a certain location[113]. Since real photons interact with matter stochastically, it is impossible to force photons to interact in a specific volume to directly and empirically measure the dose distribution deposited by secondary particles. For this reason, they must be estimated through theoretical simulations techniques such as Monte Carlo algorithms. Energy deposition kernels are calculated by modeling a homogeneous phantom where a primary photon interacts within a specific voxel, typically including the photoelectric effect, Compton scattering and pair-production interactions. Energy deposition kernels depend on scattering angle and secondary particle

energy; therefore they are azimuthally symmetrical and can be represented with a simple two-dimensional array.

Similarly to the terma, energy-differential kernels must be calculated for various energy ranges and convolved with the terma component by component.

Convolution

In principle, since the interaction rate is directly proportional to the incident number of photons $(dN/dx = \mu)$, the total three-dimensional distribution of dose is simply given by the convolution of primary photon distribution $T(E, \vec{r})$ and the energy deposition kernel $K(E, \vec{r'})$ by the following expression

$$D(\vec{r}) = T(E, \vec{r}) \otimes K(E, \vec{r}) = \int T(E, \vec{r'}) K(\vec{r} - \vec{r'}) \mathrm{d}^3 r', \qquad (1.10)$$

where $\vec{r'}$ is a mute variable that is removed by the convolution integral. One useful property of convolutions is that, when a Fourier transform is performed, we obtain

$$\mathcal{F}(D) = \mathcal{F}(T \otimes K) = \mathcal{F}(T) \times \mathcal{F}(K), \qquad (1.11)$$

which is much easier to solve in K-space because it is simply the product of the Fourier transforms of T and K, without requiring the evaluation of a complex integral. The dose distribution can then be obtained simply from the inverse Fourier transform of Eq. 1.11. To solve this equation, we are implicitly assuming that the energy deposition kernel does not depend on the position. However, real patients have inhomogeneities of widely varying density (e.g., bone, lung).[121] Therefore, the dose deposition kernel depends on the local tissue. For MV energies, Compton scattering is the dominant interaction. Compton scattering interactions occur with free electrons:

$$\left(\frac{\sigma}{\rho}\right)_{Compton} \propto \frac{N_A Z}{A} \sigma_e \qquad (1.12)$$

where σ is the Compton interaction cross-section for a whole atom of a given element, ρ is the physical density of the element, N_A is Avogadro's number, Z the atomic number, A the mass number, and $_e\sigma$ the Compton interaction probability with a single electron[89]. In eq. 1.12, $N_A Z/A$ represents the number of electrons per unit mass. The material composition, determined by Z, does not appear in eq. 1.12 elsewhere than the electron density; therefore the exact material compositon is unimportant and only the electron density matters. Since the spatial HU information in a CT scan provides this electron density, inhomogeneities can be modeled by simply scaling energy deposition kernels according to electron density[121].

Theoretical issues with convolution-superposition computation of kV x-ray dose

Adapting a convolution-superposition TPS for kV x-rays theoretically only requires that the terma and energy deposition kernels be calculated for keV energies. The terma can be calculated in exactly the same way as for MV x-rays. This leaves only the problem of the energy deposition kernels.

In some ways, computing energy deposition kernels should be easier in the keV energy range. First, electrons created by a 150 keV mono-energetic photon—a conservative high bound for diagnostic kV beams—have a maximum range of 50 μm[89], using the continuously-slowing-down approximation. Even in low-density lung, these electrons have a range of $\sim$0.2 mm. Since these electrons are absorbed locally for all practical purposes, there is no need to model contamination or scattered electrons. Second, fluorescence photons created when a K-shell electron is ejected from the atoms found in the human body (Z<30) by photo-electric effect have very low energy ($\leq$ 10 keV) and can be also considered to be locally-absorbed. Third, there is practically no bremsstrahlung radiation production, so no photons escape the energy-deposition kernel computation. Finally, the photons are well below the threshold energy required for pair production (1.022 MeV), so there is no need to account for positron-electron annihilation photons[89]. Despite these advantages, there are two very important limitations of convolution-superposition algorithms that limit

41

their adaptation to kV applications.

The first limitation is the relative importance of scattered dose in kV beams. As we showed earlier, convolution-superposition algorithms handle heterogeneities by calculating effective radiological depths. These radiological depths in turn only depend on the average density between the origin of the photon and the dose computation point, and not the density distribution. This is a valid approximation for the primary and secondary kernels, but not for photons which undergo more than 1 scattering event[121]. At MV energies, photons lose an average of $\geq 60\%$ of their energy per interaction (Fig. 1.9), and most of the scatter is forward-directed. Therefore, the error introduced by inaccurate treatment of multiple-scatter photons is negligible[121]. However, the reverse is true at kV energies: the photons on the higher end of the kV spectrum ($\sim$100-150 kVp) only lose an average of 20% of their energy per interaction (Fig. 1.9), and the scatter is nearly isotropic[11, 121]. Photons thus survive many scattering events and diffuse widely through the medium. For instance, in our percent-depth-dose (Chapters 2 and 3) or CBCT (Chapter 4) dose computations, multiple-scattered photons deposited $\sim$10-50% of the total dose, depending on the depth. Because of the relatively isotropic distribution of the scattered photons at kV energies, convolution-superposition algorithms adapted for kV dose computations will not be able to accurately model the portion of the dose deposited outside the nominal width of the beam.

The second limitation is the increased contribution of photoelectric effect in bone. In MV beams, Compton interactions dominate even in high-Z materials[89]. Since the interaction probability of Compton interactions only depends on electron density, the density-scaling of energy-deposition kernels is a valid approximation[121]. In contrast, the photoelectric effect interaction probability increases at low energies and high Z. It is thus important at kV energies in calcium-rich bone. This causes the attenuation through bone to be two to four times higher than could be expected from density-scaled dose-deposition kernels alone[4, 50]. Convolution-superposition computation of kV dose in, around or through bone will thus be
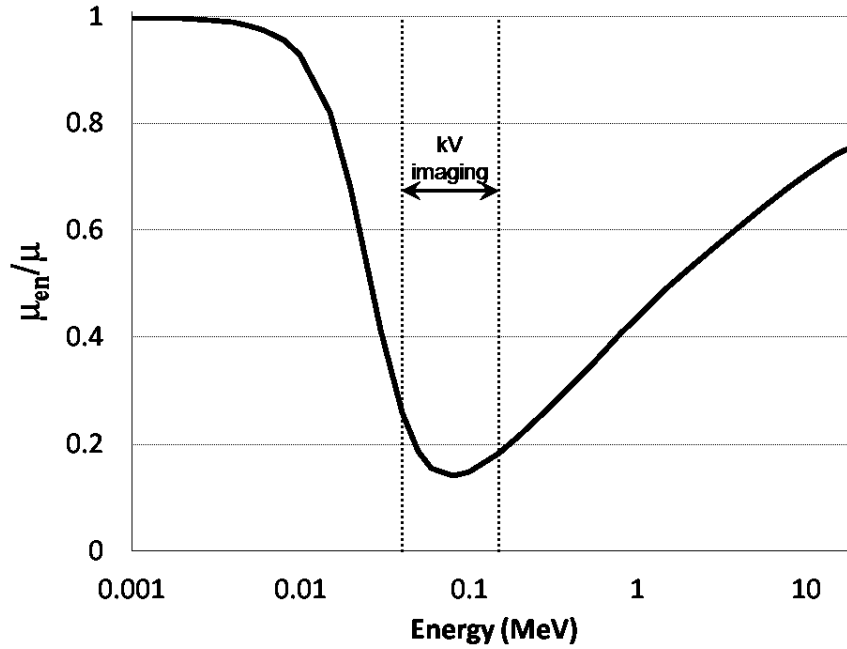
Figure 1.9: Proportion of surviving photons in kV energy range in water. The μ_{en}/μ represents the average fraction of energy lost per interaction as a function of energy. At low energies, the photoelectric effect causes $\mu_{en}/\mu \approx 1$. At high energies, Compton and pair-production interactions transfer more energy to charged particles per interaction. In the 40–150 keV range, $\mu_{en}/\mu \approx 15$–25% and photons can survive many scattering events. The values of μ_{en} and μ were obtained from the NIST.[17]

subject to systematic errors. These errors are impossible to correct without changing the nature of the algorithm—and therefore negating the main advantage of adapted TPS, their relative clinical feasibility.

Convolution-superposition algorithms adapted for kV x-ray dose

Despite these difficulties, Alaei *et al.* have developed a method to commission a kV beam in the commercial TPS Pinnacle[3]. The first requirement was the generation of kV energy deposition kernels. This was achieved for the 20–110 keV range using the EGS4 Monte Carlo package[95] in Alaei *et al.*, 1999[4]. The kernels were subsequently incorporated in Pinnacle[3] and used to compute doses in homogeneous[4] and heterogeneous (i.e., including lung-equivalent material) reference geometries[5]. Estimation of dose in an anthropomorphic

phantom followed in Alaei *et al.*, (2001), but this was not experimentally validated[6].

While the initial work by Alaei *et al.* was meant to model long intra-operative fluoroscopy or brachytherapy procedures, the focus of their work changed in Alaei *et al.*, 2010 due to the advent of kV CBCT in IGRT[3]. In this study, Alaei *et al.* modeled a Varian® OBI® in Pinnacle^3. The bowtie filter was modeled as an added physical wedge in the Pinnacle^3 software. Commissioning a beam in a TPS requires the modeling of a plethora of variables describing the source: the beam spectrum, electron contamination parameters, the effective source size, and the filter shape. These were varied by Alaei *et al.* by trial-and-error until a best fit with measured depth-dose curves was obtained.

Alaei *et al.* validate their approach using TLDs measurements in a RANDO® anthropo-morphic phantom. The study shows good accuracy ($\leq 4\%$) in water between measured and calculated percent depth-dose and lateral profiles in the main path of the beam. Outside the main path of the beam, where a greater portion of the dose is deposited by multiple-scattered photons, local dose disagreement reaches up to $\sim 20\%$ of local dose. This high percentage dose disagreement is applied to a lower overall dose, so it would not lead to large absolute dose errors. In the anthropomorphic RANDO® phantom tissue and lung-equivalent materials, the agreement ranged from -19–14%. Moreover, the agreement near or inside bones left much to be desired, as it was systematically 12–29% higher than measurements. This was after a post-hoc attempt to correct for different mass-energy attenuation factors using the method outlined in the AAPM's Task Group 61 protocols on kV dosimetry[111]. This bone disagreement is expected because the high-Z component in bone (i.e., calcium and phosphor) causes a relatively high proportion of photoelectric interactions that are not modeled by density-scaled convolution algorithms. The problem posed by bones was also reported in the more comprehensive study on commissioning an Elekta XVI kV imaging beam in Pinnacle^3 in Alaei *et al.*, (2012)[7]. In this later study, there was no attempt to compare TLD doses to Pinnacle^3 calculations near bone interfaces.

Proposed bone correction algorithm

Ding *et al.*, 2008 developed a method to improve the accuracy of Alaei *et al.*'s convolution computations in, near, and through bones[50]. In this method, the 3D dose distribution is first obtained by conventional convolution-superposition algorithms and then processed to improve the accuracy near bony structures. The 3-D dose distribution is multiplied by a series of coefficients whose values depend on the position of the voxel with respect to the bone interface—upstream, inside, and downstream of the bone, respectively. As the beam approaches the bone, there is a dearth in backscattered photons due to photons being absorbed via photoelectric effect in the bone. The coefficient is therefore slightly lower than unity and decreases as it approaches the bone interface. Inside the bone, the greater mass-attenuation coefficients in bone compared to tissue brings the coefficient to a value of 2–6. Downstream of the bone, the beam has been highly attenuated in the bone. The coefficient is therefore significantly lower than unity, depending on the thickness of the bone.

The values of the coefficients are determined by comparing TPS and Monte Carlo calculations inside a reference geometry. The method was tested by comparing dose profiles in a patient head CT computed using Monte Carlo and the proposed correction algorithm; while the algorithm improved the accuracy of the TPS computations tremendously, the correction algorithm still underestimated the dose by a factor of up to 26% in the distal bone interface. The problem with this approach was that the patient geometry dependence of the correction coefficients had not been investigated, as only a single case was used for validation. This was further investigated by Pawlowski *et al.*, (2011), where an effective bone-depth was calculated at regular angle intervals and used to obtain patient and beam-specific multiplication factors[133]. Using these factors, the dose distributions inside 10 different patient cases was computed with a mean accuracy of 2.6 $\pm$ 13.5% compared to Monte Carlo computations.

If the method proposed by Ding[46, 47, 45, 49] and improved by Pawlowski[133] can be adapted to work within a commercial TPS, it will solve the issues involved in computing

the kV CBCT dose using an adapted TPS. These correction factors currently have to be calculated empirically on a case-by-base basis using lengthy Monte Carlo computations— Pawlowski reports a length of four to five days per patient. The main advantage of using commercial TPS to compute the patient and beam-specific patient dose deposited by kV CBCT imaging procedure is its clinical feasibility—that is, it requires no additional software, equipment or knowledge to operate and includes the imaging dose. While it is promising, the proposed bone-correction technique does not currently hold many advantages over conventional Monte Carlo simulations.

1.2.4   Conclusions

In this section, we described current and proposed dose measurement and estimation techniques for kV CBCT imaging procedures. The current standard estimation technique, the CTDI, is highly problematic. Many of the theoretical assumptions required for CTDI to represent the average patient dose are not true in kV CBCT beams. While the CTDI is useful for comparing machine output from one imaging protocol to the next, it does not provide a patient-specific spatially absorbed dose, and the conversion to effective dose depends on "one-size-fits-all" factors published by the ICRP.[78, 79, 81] Other experimental techniques are better since they offer insight on patient-specific skin dose or anthropomorphic phantom internal dose. Unfortunately, they do not provide the patient-specific internal dose distribution.

Theoretical dose estimation methods should, in principle, bridge this gap and provide full 3-D spatial distributions of the absorbed dose inside the patient. However, the methods currently proposed still have issues which limit their clinical feasibility. Adapting commercial TPS offers the most clinical feasibility by making use of software already available in every medical physics clinic. Unfortunately, the convolution-superposition algorithms they use cannot accurately model the attenuation through bone, and therefore are liable to systematic

errors near or through bony structures. Monte Carlo simulation techniques provide the best estimate we have of the "real" dose, but are time-consuming and require highly specialized techniques.

There is therefore room for the development of an alternative method more accurate than adapted commercial TPS, yet easier to implement clinically than conventional Monte Carlo simulations. In the following section, we describe the kV dose computation method that is proposed as an alternative by this thesis.

1.3 kVDoseCalc

1.3.1 kVDoseCalc overview

Introduction

There are three main categories of dose computation sofware: correction-based, model-based, and Monte-Carlo.[121]

Correction-based software, which are also known as empirically-based, use extensive measurements of dose depth-dose, inline and crossline profiles in homogeneous materials to estimate the dose in a volume. Patient-specific inhomogeneities and variations across the patient's contour are handled by corrections like the effective radiological pathlength method or the Batho Power law method. Correction-based methods can be used either for kV or MV treatment planning; one such example for kV beams is recent work by Marco-Rius *et al.* to calculate the dose delivered in small animals[114]. Correction-based algorithms can be very accurate calculating dose to simple geometries, but are unable to model the complicated scatter conditions caused by contours and inhomogeneities, so are unsuitable for patient-specific dose calculations.[121]

In contrast, model-based software describe either Monte Carlo or commercial treatment-planning algorithms, such as Pinnacle[3] or Varian's analytic anisotropic algorithm (AAA) that we previously described in section 1.2.3. The commercial algorithms rely on dose mea-

surements taken at commissioning to obtain beam-specific variables. They are more accurate than correction-based approaches, but not as much as complete Monte Carlo approaches. Finally, Monte Carlo algorithms model the photon flux and dose distribution from first principles by using a stochastic approach. They offer the best accuracy if sufficient statistics are obtained, but this can be quite a lengthy process.

In this thesis, the method we use is a kV dose computation software originally developed in-house by Alexei Kouznetsov and Mauro Tambasco—kVDoseCalc[103]. kVDoseCalc uses both deterministic and stochastic algorithms to calculate the photon flux and dose at a series of points of interest (POIs). It is therefore a hybrid of both Monte Carlo and deterministic calculations. In this section, we provide an overview of kVDoseCalc and the work done by collaborators before the beginning of this thesis. We then present the steps which were required to characterize a kV CBCT beam and the different steps we took to achieve this objective.

Summary

kVDoseCalc contains a graphical user interface (GUI) that makes it relatively easy to use. These are the main steps required to calculate the dose:

(1) A CT image in DICOM (Digital Imaging and Communications in Medicine) format describes the volume of interest.

(2) The x-ray source is described as a spatial distribution of photons with a certain energy, origin, and direction.

(3) The user defines the materials of interest in the volume (e.g., tissue, bone, lung). These are used to weight the microscopic atomic interaction cross-sections for photoelectric, coherent and incoherent scattering from the ENDF/B-VI microscopic atomic interaction cross-section library[129]. Thus, the material-specific interaction cross-sections are calculated for every possible energy (1–150 keV). The choice of the ENDF/B-VI cross-sections was made

by the original designers of the kVDoseCalc algorithm.[103] However, in principle other cross-section libraries could be used.

(4) The CT image contains HU information (electron density), but the software requires material physical densities. Therefore, the user specifies ranges of HU in the CT image that correspond to known physical densities (g/cm^3). Ranges of physical densities are set to correspond to a specific material. The entire DICOM image is segmented into various materials and physical densities.

(5) The primary and scattered differential angular flux densities are calculated at the POI using deterministic and stochastic algorithms (see section 1.3.1) to solve the linear Boltzmann transport equation (LBTE).

(6) The primary and scattered dose is calculated at the POI using the material-specific cross section from (3) integrated over the spectrum of the differential energy flux and the energy transfered to the medium by the relevant particle-matter interactions.

Description of the Source

To estimate the dose at the POI, kVDoseCalc requires that the kV x-ray source be described by a source term. This source term, $q(\vec{r}, E, \hat{\Omega})$, represents the fraction of photons with an energy E, coming from the position $\vec{r}$, and with an orientation $\hat{\Omega}$. From a computing perspective, the source is entirely arbitrary; in practice, the user is constrained through the GUI to a relatively simple description of the kV source.

At the start of this project, the source model was limited to a conical source with a single spectrum (see Fig. 1.10). Some conical kV x-ray sources exist, such as in superficial or orthovoltage therapy. Since CBCT fields are square, kVDoseCalc required extensive changes to the source description GUI and the source model. A full description of the medical physics and mathematical formalism of the final source model is available in Chapter 3. Figure 1.11
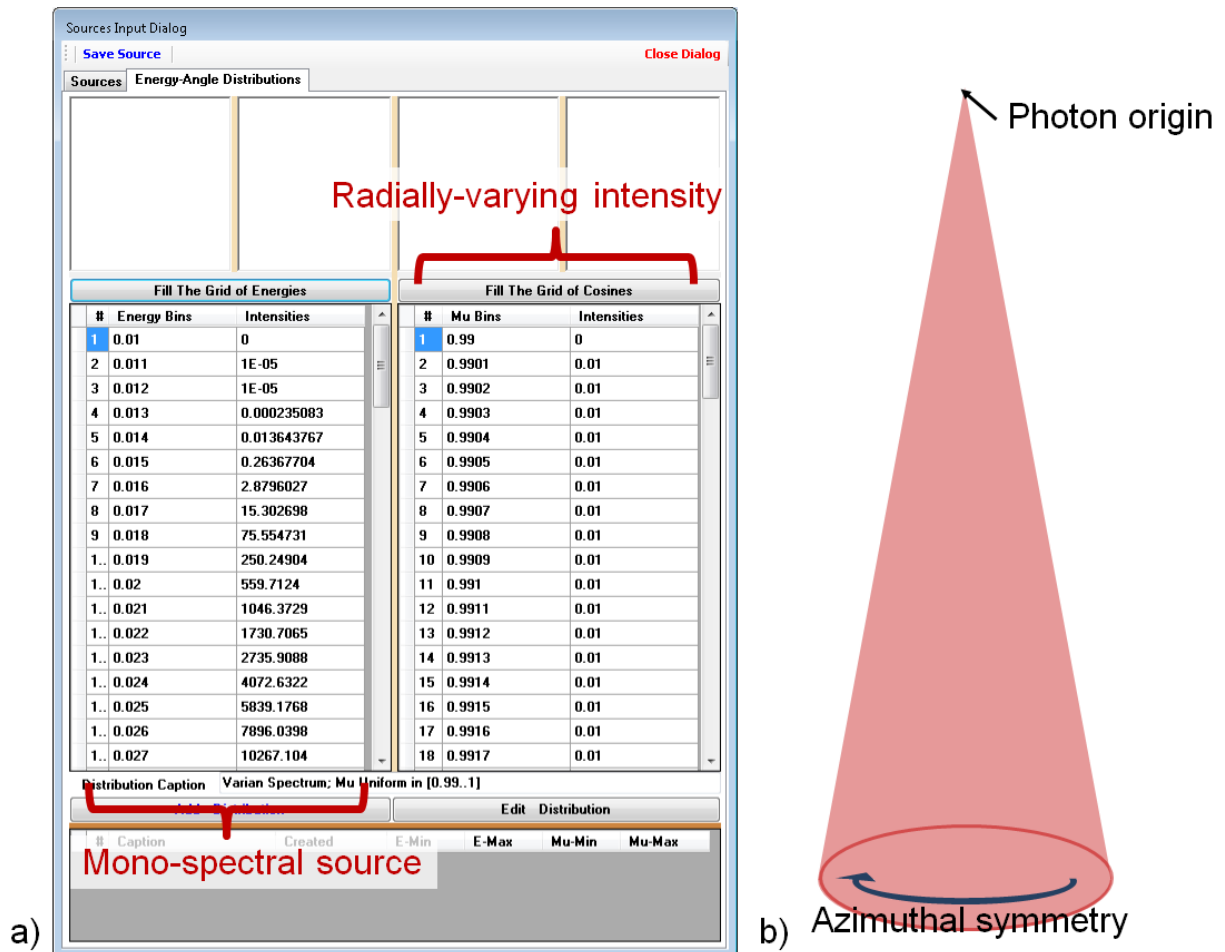
Figure 1.10: Early conical source description (a) and model (b) in kVDoseCalc. The spectrum is defined in the column to the left. The user can specify a radial fluence variation using the right column.
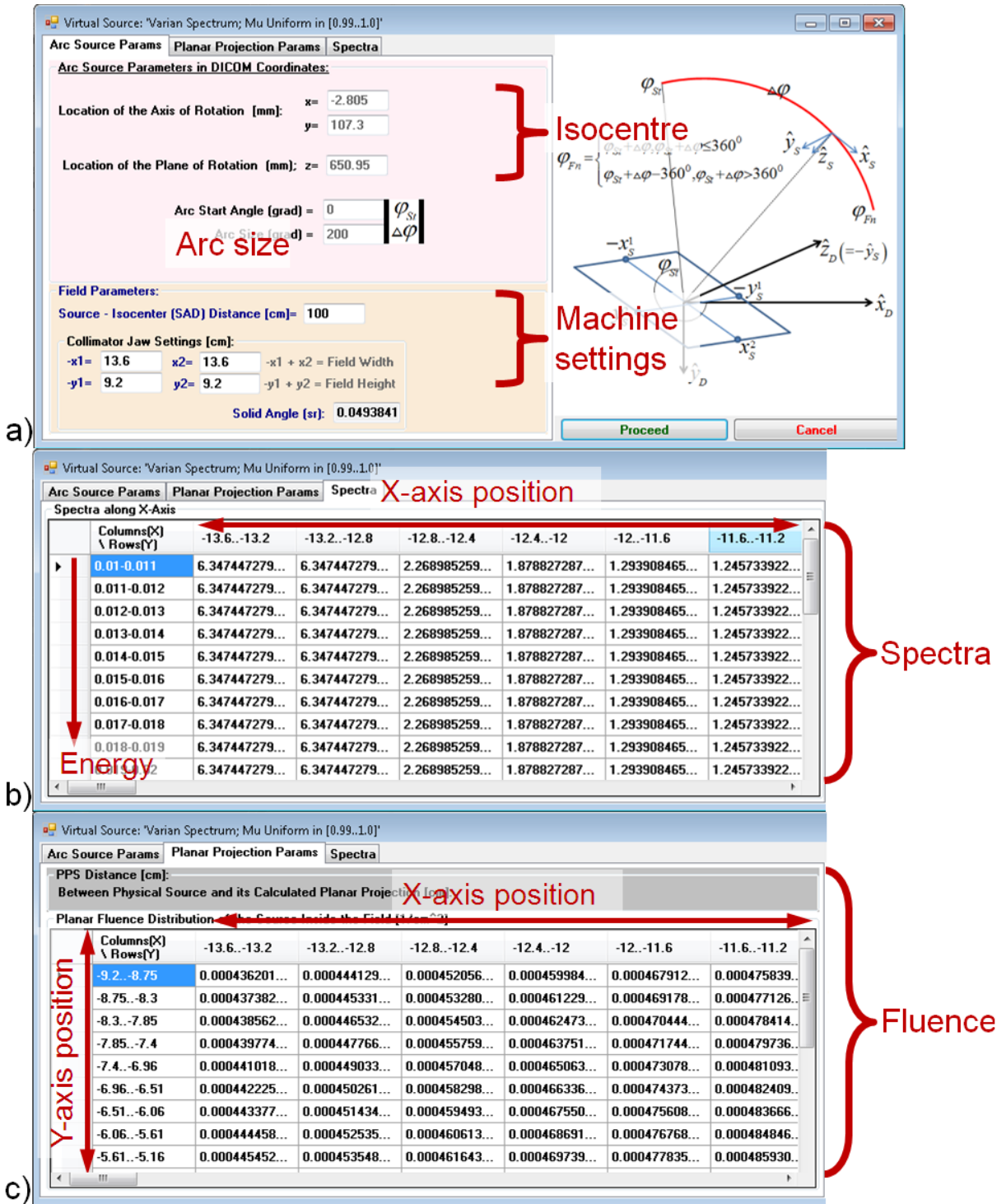
Figure 1.11: Final square source description in kVDoseCalc. The user specifies details of the scan parameters such as the isocentre position, jaw settings, and arc size (a). Then, the user defines spectral variations along the transverse axis (b) as well as a 2-D planar fluence array (c). These values are used to create the histories in kVDoseCalc's biased Monte Carlo transport algorithm.

shows how the user defines the spatial and spectral variations of the beam.

The spatial and spectral variations of the fluence are used to solve the LBTE and generate the histories of the particles in the calculation of the differential angular flux density (see section 1.3.1).

Material segmentation

CT images are used in radiation therapy planning because they provide volumetric electron density information through HU. With an appropriate HU-to-electron density curve, the HU provides enough information for accurate MV x-ray dose calculation because the Compton effect dominates. In kV beams, the increased importance of the photoelectric effect in high-Z materials requires the segmentation of the CT image into different material compositions. In kVDoseCalc, this is a three-step process.

First, the user defines the materials of interest in the volume. For each material, the user specifies the number density of every element in units of 10^{24} atoms/cm^3 (Fig. 1.12a). The number density n^i of the i-th element of a material is defined by the expression

$$n^i = \frac{P^i}{A_r^i} \rho N_A, \tag{1.13}$$

where ρ is the physical density (g/cm^3) of the material, N_A is Avogadro's number, P^i is the fraction of the material mass due to the i-th element, and A_r^i is the relative atomic mass of the i-th element. Second, a HU-to-density table converts HU ranges to physical density ranges (Fig. 1.12b). Finally, a table assigns materials to physical density ranges (Fig. 1.12c).

In the case of artificial phantoms, these physical densities are known for all of the materials. However, estimating the density of tissues inside a patient is much more difficult. Ultimately, there is no alternative to relying on published data such as the ICRU publication 46[82], a limitation that is shared by algorithms which require more than the CT-provided electron density. These atomic number densities are used to calculate the material and

energy-specific interaction coefficients required to solve the LTBE[103, 129].

1.3.2 Photon flux transport

The photon differential angular flux density is evaluated at the POI in three separate components: primary/unscattered, first-collision, and multiple-collision. The primary component is calculated deterministically, while both scattered components are calculated using a biased Monte Carlo stochastic algorithm. Unlike conventional Monte Carlo simulations where trajectories are chosen in a truly random manner, biased Monte Carlo algorithms are design to sample trajectories which will are more likely to deposit dose at the POI over those which are less likely.

Primary component

The primary component represents photons that have never interacted with the medium. Since primary photons cease to exist at their first interaction, it is relatively easy to apture their first interaction in the medium. The differential angular flux density is attenuated through the beam divergence expressed by the inverse-square law, and by linear attenuation through the material.

First-collision component

The first-collision component represents photons interacting at the POI that have only interacted once within the medium. In principle, the first-collision component differential angular flux density at the POI can be evaluated relatively simply: it will be equal to the primary differential angular flux density at the first interaction point (calculated as per the primary component), times the coherent and incoherent scattering cross-section for the specific scattering angle needed to reach the POI (second point of interaction), attenuated exponentially through the material between the scattering point and the POI. However, obtaining an analytical equation for the scattered flux at the POI requires integrating over
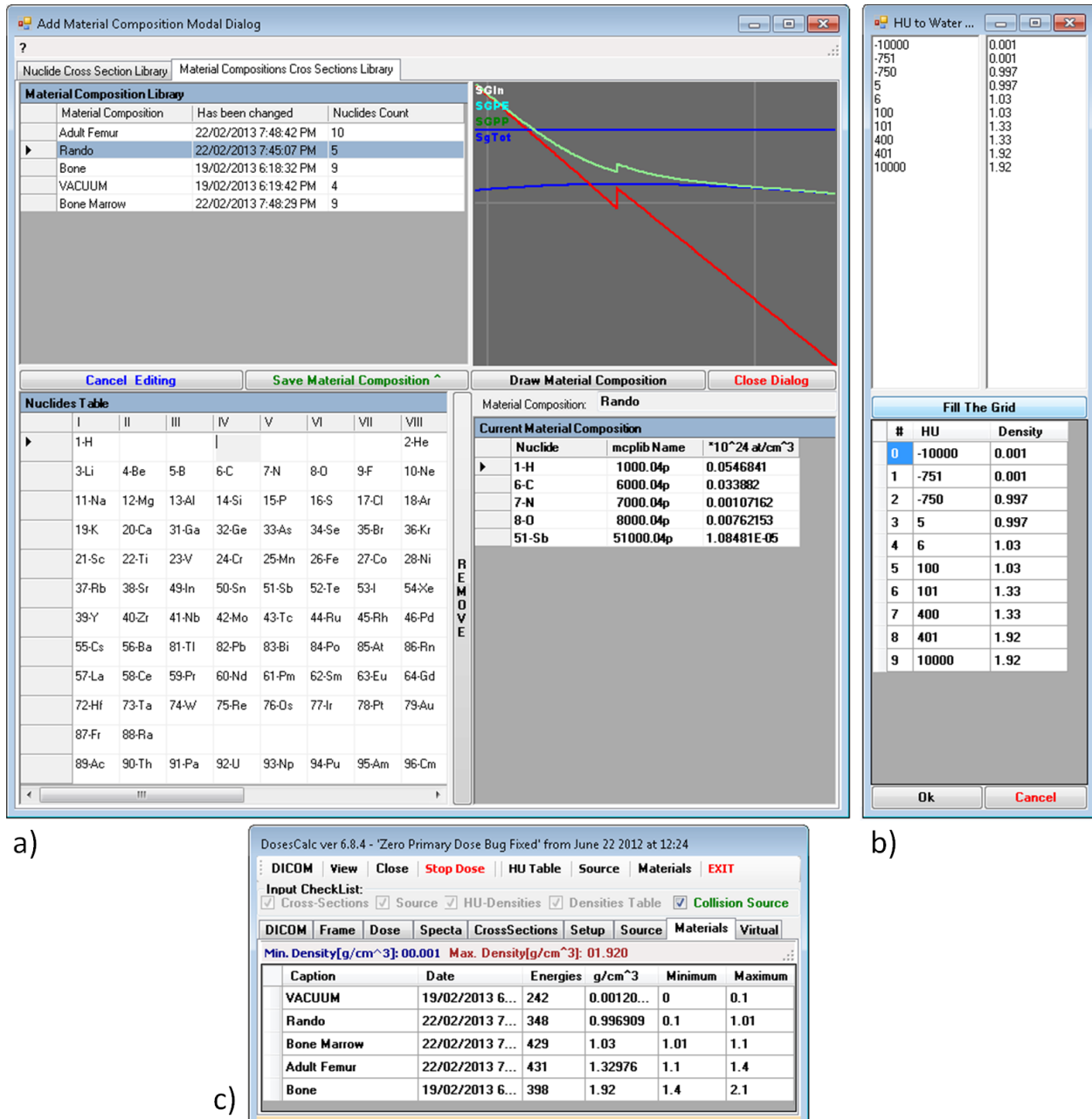
Figure 1.12: Process of material segmentation in kVDoseCalc. First, material atomic densities are defined (a). Then, a HU-to-physical density conversion table is applied (b). This conversion table is currently arbitrarily defined by the user, further investigation is required to find the optimal values for patient computations. Finally, materials are assigned to ranges of physical densities (c). These materials correspond to the atomic densities from (a) which contain all of the interaction cross-section information needed for radiation transport throughout the volume of interest.

the entire volume, for all energies and scattering angles.

Instead, kVDoseCalc evaluates the first-collision differential angular flux density at the POI by Monte Carlo simulation. Instead of calculating the entire radiation transport through the medium, scattering points are generated around the POI and the transport equation is solved for individual scattering histories. To reduce the calculation times, kVDoseCalc uses importance sampling, a common Monte Carlo technique[124]. Since photons that scatter far away from the POI are more likely to interact before reaching the POI, sampling the whole volume equally would lead to excessive computational resources being spent generating histories from scattering events which account for a relatively small portion of the incident flux. Instead, the importance sampling function decreases exponentially with distance from the POI (taking material composition into account), giving a greater weight to photons that scatter close to the POI and vice-versa.

Multiple-collision component

Obtaining a transport equation for the first-collision component of the differential angular flux density was relatively simple, since it depends on the easily-calculated primary component. However, with each successive scattering event, modeling the transport becomes more complex. In kVDoseCalc, this is avoided by generating a population of representative origin points for the multiple-collision component of the flux at the POI. This scattering point population is generated by following the histories of individual photons through Monte Carlo simulations for each investigated geometry and source combination. Since a photon scattering in any of these points could reach the POI, all of the scattering points act as a source of the multiple-collision component of the flux. Unlike the first-collision component of the flux, where scattering points are generated around the POI for every new POI, the same scattering points are used to calculate the multiple-scattered flux for any POI, regardless of the position. Hence, the scattering points population is calculated only once for a characterized x-ray source/CT image combination and saved in a separate file. Since the majority

of the transport calculations are done in advance, this approach calculates the multiple-collision differential angular flux density much more rapidly than conventional Monte Carlo simulations.

Kerma calculation

We have shown how kVDoseCalc calculates the incident photon flux at the POI, but the quantity we are really interested in is the dose rate at the POI. As we explained earlier in section 1.2.2, electrons are absorbed locally for kV energy beams so we have charged particle equilibrium (CPE) at every point in the medium. Furthermore, x-ray producing bremsstrahlung interactions are negligible ($\leq 0.1\%$) at this energy-range, even in the relatively high-Z bone[11]. Therefore, the dose $D(E)$ deposited by photons of energy E is equal to the kerma $K(E)$, as per the following expression

$$D(E) \overset{CPE}{=} K(E) = \Phi(E)\frac{\mu_{en}(E)}{\rho}E, \qquad (1.14)$$

where μ_{en}/ρ represents the mass-energy absorption coefficient (i.e., the fractional energy lost by interactions in the medium) and $\Phi(E)$ represents the flux at the POI. Like previously mentioned, kVDoseCalc models three types of interactions: photoelectric, coherent, and incoherent scattering. All of the energy is absorbed during a photoelectric interaction, so $\mu_{en} = \mu$.

Compton scattering interactions are more complicated, since the energy lost in the collision depends on the scattering angle. In kVDoseCalc, the Klein-Nishina (Compton) cross sections are calculated in every material. They are integrated over every possible scattering angle to count the contribution of every possible amount of energy imparted to the medium. Doing this yields a flux-to-kerma rate coefficient factor that can be used to convert direction from the flux (which is known) to the dose (which is the quantity of interest). These are calculated in every material and for every photon energy.

Monte Carlo validation

Kouznetsov and Tambasco validated the software computationally against the industry-standard Monte Carlo code packages EGSnrc[95] and MCNP[187] in a heterogeneous block phantom[103]. The kV x-ray beam was described as having a constant fluence over a diameter of 10 cm, placed 100 cm from the surface of the phantom. The quality was a 125 kVp Varian® OBI® obtained from Ding *et al.* by Monte Carlo simulations[46]. The dose was computed inside a heterogeneous phantom comprised of tissue, lung, and cortical bone as defined by the ICRU-46 publication[82]. Since the same beam and geometry were defined for all three computation methods, the only source of disagreement was the dose calculation method itself. However, all three computation techniques agree within 1.5% in all points. This result shows that the software is able to accurately model the physics of kV x-ray transport in a highly attenuating heterogeneous geometry.

However, this was achieved for a very simple beam geometry. In reality, the accuracy of the dose calculation will only be as accurate as the description of the volume and the kV x-ray source. Thus, the objective of this thesis is the development of a virtual point source model and empirical source characterization method to accurately compute the dose deposited by kV CBCT procedures in a clinically feasible manner.

1.3.3 Thesis overview

The aim of this thesis is to provide a clinically feasible characterization and source model to compute the absorbed dose deposited by kV x-rays. More specifically, I model and validate the method for kV CBCT imaging procedures as they represent a potentially important source of unaccounted dose in radiation therapy. However, the method described in this thesis is not limited to CBCT imaging and has been applied successfully in other applications such as conventional CT scanners, and for square beams in superficial and orthovoltage

therapeutic x-ray units.

At the beginning of this project, our only resource was the previously described kV-DoseCalc: a kV x-ray dose computation software previously validated with well-established Monte Carlo simulation techniques MCNP and EGSnrc[103]. However, at this time it was only possible to define a beam in kVDoseCalc with a single spectrum defining the whole beam, and a circular shape where photon intensity depended solely on the radius. Unfortunately, these properties did not describe many clinical beams with the possible exception of superficial or orthovoltage therapeutic x-ray units. Therefore, an overhaul of the software and the way in which it modeled a kV x-ray beam was required.

Approach philosophy

In order to achieve the purpose of this thesis, the first and foremost task was to devise a method by which to describe and characterize a clinical kV x-ray source. There are two main ways in which this problem could be approached: First, the source could be modeled from first principles using Monte Carlo simulation techniques, such as was done by Ding *et al.*[46, 45]. Alternatively, one could use experimental measurements to characterize the beam, such as done by Alaei *et al.* when commissioning an Elekta kV XVI unit using the commercial TPS Pinnacle[3][4, 5, 7]. The common element to both of these kV x-ray source characterizations is that the chosen source model and characterization method plays to the strength of the dose computation method (kVDoseCalc).

Likewise, I decided early in the project that the characterization method and source model we would choose would play on the strengths of kVDoseCalc. While the model is not exclusive to kVDoseCalc and could theoretically be applied to other dose computation methods, it was developed with the limitations and advantages of kVDoseCalc in mind. The main advantage of the model is that it is defined entirely by empirical values and does not require any proprietary knowledge from the manufacturer. Therefore, it does not depend on

Monte Carlo simulation techniques. To show that this model did not require complex Monte Carlo modeling techniques, I decided to never require Monte Carlo techniques at any step of the source characterization and modeling process.

The philosophy of this thesis is that a medical physicist should be able to characterize and model a kV x-ray source using a minimum number of empirical measurements obtained with routine clinical equipment without specialized equipment or computational techniques.

Spectrum characterization

The first step of this project was to develop a method to characterize a kV x-ray beam spectrum. We developed a simplified spectrum characterization method requiring only the nominal kVp and measured HVL. We generate spectra using a third-party freeware (Spektr[153]) and vary the inherent aluminum filtration in an iterative process until the calculated HVL of the beam matches the measured HVL. Chapter 2 outlines this method, and shows how it was validated by a sensitivity analysis and ionization chamber measurements. The work described in this chapter has been published in the peer reviewed journal, *Medical Physics*, under the title *A simplified approach to characterizing a kilovoltage source spectrum for accurate dose computation*[138].

Fluence characterization

The second step of the project was to build on the spectral characterization and create a complete model of the kV x-ray beam. This included modeling spatial variations of the spectrum and fluence. Chapter 3 describes in detail the full virtual point source model and characterization method proposed in this thesis. It lays down the complete intellectual groundwork of our approach. We use the method to characterize imaging beams including bowtie filters. To validate the approach, we compare the computed dose to ionization chamber measurements in homogeneous and heterogeneous block phantoms. The work pre-

sented in this chapter has been published in the peer reviewed journal *Medical Physics*, under the title *Experimental validation of a kilovoltage x-ray source model for computing imaging dose*[137].

Validation and proof of concept for CBCT imaging

Finally, the last step was to use the previously validated method to characterize complete CBCT imaging procedures. In chapter 4, we provide a proof of principle by comparing computations to measurements in a CTDI-like homogeneous cylindrical phantom and—more importantly—in a patient-simulating anthropomorphic phantom. The work in this chapter represents a full proof of concept—we show that it is possible to load a CT of a patient and compute the dose deposited by a kV CBCT within reasonable accuracy. We also outline the issues which will need to be resolved before the method can be applied clinically. This work manuscript will be submitted in early 2014 in the peer reviewed journal *Medical Physics*. It will be titled *Experimental validation of a kilovoltage CBCT dose computation method*.

Applications, conclusions and future work

The characterization method and virtual point source method that are the subject of this thesis were designed and validated to calculate the kV CBCT dose. However, it can be used to describe any kV x-ray source and has wide applicability in kV dosimetry. In collaboration with others, the method outlined in this thesis was successfully used to describe a kV orthovoltage unit and a conventional CT scanner. Chapter 5 briefly discusses these results, and presents overall conclusions and future work.

Chapter 2

Spectrum Characterization

2.1 General Introduction

The work presented in this chapter represents the initial steps in creating a viable and clinically feasible virtual point source model for kVDoseCalc by focusing first on a simple way to characterize the kV beam spectrum. We propose a method in which the HVL and kVp are used in conjunction with third-party freeware in order to derive the full spectral information of the beam. An analysis on the sensitivity of dose computations with regards to HVL and kVp reveals that they represent sufficient characterization of the beam for accurate dose computation within experimental uncertainty. We use this method to characterize the spectrum of three kV imaging energies in our centre and validate our characterization by comparing dose computations to percent depth-dose profiles and transverse axis profiles in a homogeneous and heterogeneous phantom.

The remainder of this chapter has been published in *Medical Physics*, a peer reviewed journal[138]. I was the first author of this work, and the contributing authors were Dr. Alexei Kouznetsov and Dr. Mauro Tambasco. Dr. Mauro Tambasco suggested the spectrum characterization method and the sensitivity analysis. I designed and performed the sensitivity analysis and the experimental measurements, and proposed the earliest version of the new virtual point source model allowing for square fields. With assistance from Dr. Alexei Kouznetsov, I designed a new GUI in kVDoseCalc allowing the isocentre plane fluence to be input by the user, which Dr. Alexei Kouznetsov then implemented. I wrote the first draft of the manuscript, and all authors helped review and revise the manuscript before its ultimate publication.

In the process of writing the manuscript of the following chapter, I noticed a minor error affecting the reported accuracy of the dose computation within the bone-equivalent material. I investigated the source of the error and the corrections were published as an erratum in *Medical Physics*[139]. This erratum is presented in section 2.3 after the main text.

2.2 A Simplified Approach to Characterizing a Kilovoltage Source Spectrum for Accurate Dose Computation

Y Poirier[1], A Kouznetsov[1], and M Tambasco[2]

[1] Department of Physics and Astronomy, University of Calgary, Calgary, Alberta T2N 4N2, Canada

[2] Department of Physics and Astronomy and Department of Oncology, University of Calgary and Tom Baker Cancer Centre, Calgary, Alberta T2N 4N2, Canada

2.2.1 Abstract

Purpose: To investigate and validate the clinical feasibility of using half-value layer (HVL) and peak tube potential (kVp) for characterizing a kilovoltage (kV) source spectrum for the purpose of computing kV x-ray dose accrued from imaging procedures. To use this approach to characterize a Varian® On-Board Imager® (OBI) source and perform experimental validation of a novel in-house hybrid dose computation algorithm for kV x-rays.

Method and Materials: We characterized the spectrum of an imaging kV x-ray source using the HVL and the kVp as the sole beam quality identifiers using third-party freeware Spektr to generate the spectra. We studied the sensitivity of our dose computation algorithm to uncertainties in the beams HVL and kVp by systematically varying these spectral parameters. To validate our approach experimentally, we characterized the spectrum of a Varian® OBI system by measuring the HVL using a Farmer-type Capintec ion chamber (0.06 cc) in air, and compared dose calculations using our computationally validated in-house kV dose calculation code to measured percent depth-dose and transverse dose profiles for 80 kVp, 100 kVp, and 125 kVp open beams in a homogeneous phantom and a heterogeneous phantom comprising tissue, lung, and bone equivalent materials.

Results: The sensitivity analysis on dose computation accuracy to changes in beam quality parameters (i.e., HVL, kVp, and field size) shows that typical measurement uncertainties in the HVL and kVp (± 0.2 mm Al and ± 2 kVp, respectively) lead to dose computation errors of less than 2%. Furthermore, for an open beam with no added filtration, HVL variations affect dose computation accuracy by less than 1% for a 125 kVp beam when field size is varied from 5×5 cm^2 to 40×40 cm^2. The central axis depth dose calculations and experimental measurements for the 80 kVp, 100 kVp, and 125 kVp energies agreed within 2% for the homogeneous and heterogeneous block phantoms, and agreement for the transverse dose profiles was within 6%.

Conclusions: The HVL and kVp are sufficient for characterizing a kV x-ray source spectrum for accurate dose computation. As these parameters can be easily and accurately measured, they provide for a clinically feasible approach to characterizing a kV energy spectrum to be used for patient specific x-ray dose computations. Furthermore, these results provide experimental validation of our novel hybrid dose computation algorithm.

2.2.2 Introduction

Kilovoltage (kV) image-guided radiotherapy (IGRT) techniques such as cone-beam computed tomography (CBCT), fluoroscopy, and radiography are commonly used for radiation treatment volume localization[21]. These IGRT procedures offer many advantages such as allowing patient repositioning to account for set-up errors and inter-fractional shifts of the target volume[176]. Furthermore, the volumetric information from daily CBCT allows for adaptive treatment re-planning during treatment following changes in patient anatomy such as tumor shrinkage[163].

Although IGRT techniques are valuable in radiation therapy, these procedures introduce additional absorbed radiation dose to patients. As kV imaging x-rays have relatively low energies, the maximum dose is absorbed at the skin surface and in higher atomic number

(Z) materials such as bone. When added to megavoltage treatment dose and its associated scatter and leakage, the imaging dose could push the dose received by organs at risk (OAR) beyond their tolerances leading to a greater risk of inducing normal tissue complications. The added imaging dose may also lead to an increased risk of stochastic effects such as a secondary cancer[20, 105]. Despite the potential risk from the added dose from IGRT procedures, to the authors' knowledge there are currently no commercially available tools for routine clinical patient-specific calculations of absorbed imaging dose. Ding *et al.*[44] reported that daily CBCT for a simulated prostate treatment leads to total OAR doses of 76.7 cGy to the rectum and 141.3 cGy to the femoral heads. *In vivo* thermoluminescent dosimeter measurements by Wen et al.[182] showed that the total dose to the pelvic area can range from 130 cGy to 400 cGy for peripheral tissues and hip joints, respectively. Palm *et al.*[131] found that the average absorbed dose arising from CBCT procedures using the Varian® On-Board Imager (OBI®) (Varian Medical Systems, Inc, Palo Alto, California, USA) systems ranges from 3 to 35 mGy per fraction, depending on the site imaged and the CBCT acquisition settings. Hence, there is a need for a clinically feasible method for accurately computing dose deposited by in-room kV image-guided systems. Such a tool could be used to modify an imaging procedure/frequency and/or a radiation treatment plan to avoid exceeding OAR dose tolerances as well as keep track of the dose during the course of adaptive radiotherapy. Since radiation therapy patients are imaged using a CT simulator for the purpose of treatment simulation and planning, a CT image of the patient is already available to the physicist for this purpose.

Kouznetsov and Tambasco recently developed a novel approach to rapidly and accurately compute radiation dose at a point or series of points of interest (POI)[103]. This in-house method uses a hybrid computation algorithm combining deterministic and stochastic calculations for the primary and scattered components of the beam; respectively. The method was validated computationally by comparing it with the industry standard Monte Carlo N-

Particle Transport Code (MCNP) and EGSnrc using an idealized circular beam projection of a single spectral source[103].

In this study, the method is validated experimentally, and it is used to investigate the clinical feasibility of using the half-value layer (HVL) and the tube potential (measured in kVp) to characterize the source spectrum in a way that does not rely on specialized equipment or complex Monte Carlo modeling. The intent is that the beam quality could be locally determined by a physicist while the beam fluence could either be measured or taken from Monte Carlo published data.

In a recent study, Spezi *et al.*[156] modeled an open beam with a single averaged spectrum and they modeled a beam with added external filtration with varying spectra on the transverse axis. While the study by Spezi *et al.* focused on the spatial distribution of the photons, projecting the photons from three points (i.e., the target, the filtration cone and the bowtie filter), they did not investigate a clinically feasible approach for characterizing the spectrum of a beam, which is the focus of this study

For quality control purposes, it is common clinical practice to measure HVL and kVp to assess beam quality for kV imaging devices. Unfortunately, the measurement of HVL and kVp do not uniquely determine a spectrum, nor are they independent parameters as higher energy beams are more penetrating and thus have higher HVL. The use of published spectral data (e.g., measured or modeled by Monte Carlo) is generally not practical for dose calculations as filtration varies greatly from one x-ray tube to another, suggesting that machine-specific characterization is essential. In this study, we investigate whether HVL and kVp and their associated measurement uncertainties are sufficient to characterize the spectrum for the purpose of accurately computing x-ray dose. While these parameters do not uniquely determine an energy spectrum, they are the standard beam quality specifiers[111, 91]. This approach is tested using our previously validated hybrid kV dose computation method[103].

To study the effect of measurement uncertainty in HVL and kVp on computed dose accuracy, we performed an analysis of the sensitivity of computed dose distribution on variations in HVL and kVp. To validate our machine-specific characterization, we compared computed dose with ion chamber measurements for a Varian® OBI®. The comparison was done using a homogeneous and a heterogeneous block phantom.

We found that dose can be computed accurately by modeling the x-ray source using a Monte Carlo generated 2-D fluence distribution and characterizing the energy spectrum using the HVL and the kVp. Hence, future commissioning and clinical implementation of kV dose computation systems could be simplified by using the source spectrum modeling approach described in this study.

2.2.3 Materials and Methods

Beam Modeling

To fully model the x-ray beam, the spectral and spatial distribution of the photons must be known as the energy spectrum from a real x-ray source varies with position due to the heel effect and inherent or added filtration. The spatial distribution of the photons, or beam fluence, can be either measured or modeled through Monte Carlo simulation. We modeled the beam by projecting the fluence of a defined field size at the isocenter from a single target point. We neglected in-head scattering, geometric source size, and collimator scatter. In addition, we approximated the beam as having a single spectrum over its entire cross-section, while the fluence was position-dependent. The total dose rate from a kilovoltage unit depends on scanning parameters such as tube current, pulse width (mAs), and scan time. To compute absolute dose for a given kV imaging procedure these parameters would be needed as input for the specific imaging procedure/protocol that is performed.

To generate the spectra for our investigation, we used the computational tool Spektr developed by Siewerdsen[153] which is based on the approach by Boone *et al.*[24] In Boone's

approach, the spectra are generated by polynomial interpolation between published direct spectra measurements of different beam quality. This tool allows the user to generate an x-ray spectrum based on tube potential and inherent aluminum filter thickness. Hence, a spectrum corresponding to a specific HVL and kVp can be generated by varying the inherent filtration until the calculated HVL matches the measured value.

In this study, we have used the Monte Carlo generated fluence distribution for Varian® OBI® kV imaging systems from Ding *et al.*[46] As such, our approach to characterizing the x-ray source assumes that the fluence field for a given x-ray tube model (e.g., Varian® OBI®) is not machine-specific, allowing us to use a single characterization of the fluence for all kV imaging devices of the same model.

Sensitivity of X-ray Dose to HVL and kVp

The HVL and kVp were varied for the 125 kVp reference spectrum and the effect of these spectral changes on the calculated x-ray dose in the homogeneous and heterogeneous block phantoms (Fig. 2.1a) was examined. The goal of this experiment was to determine whether the HVL and kVp are sufficient to characterize an x-ray spectrum for accurate dose computation given the uncertainties in the measurement of these parameters. The reference spectrum for a 125 kVp Varian® OBI® x-ray source was taken from the EGSnrc/BEAMnrc Monte Carlo beam modeling performed by Ding *et al.*[46] According to Ding *et al.*, the HVL of this spectrum is 4.4 mm Al. We imported this spectrum into Spektr and used the software to analyze its HVL, and we found it to be 4.337 mm Al, which is very close to the value reported by Ding *et al.*[46]

We performed the sensitivity analysis for the 125 kVp beam by varying the HVL from 3.6 to 6.0 mm Al (Fig. 2.2a) in steps of 0.25 mm Al. We included one spectrum of exactly 4.337 mm Al in order to compare with the spectrum we used as a reference. From Fig. 2.2, we can see that the generated and reference spectra have the same general shape. However,
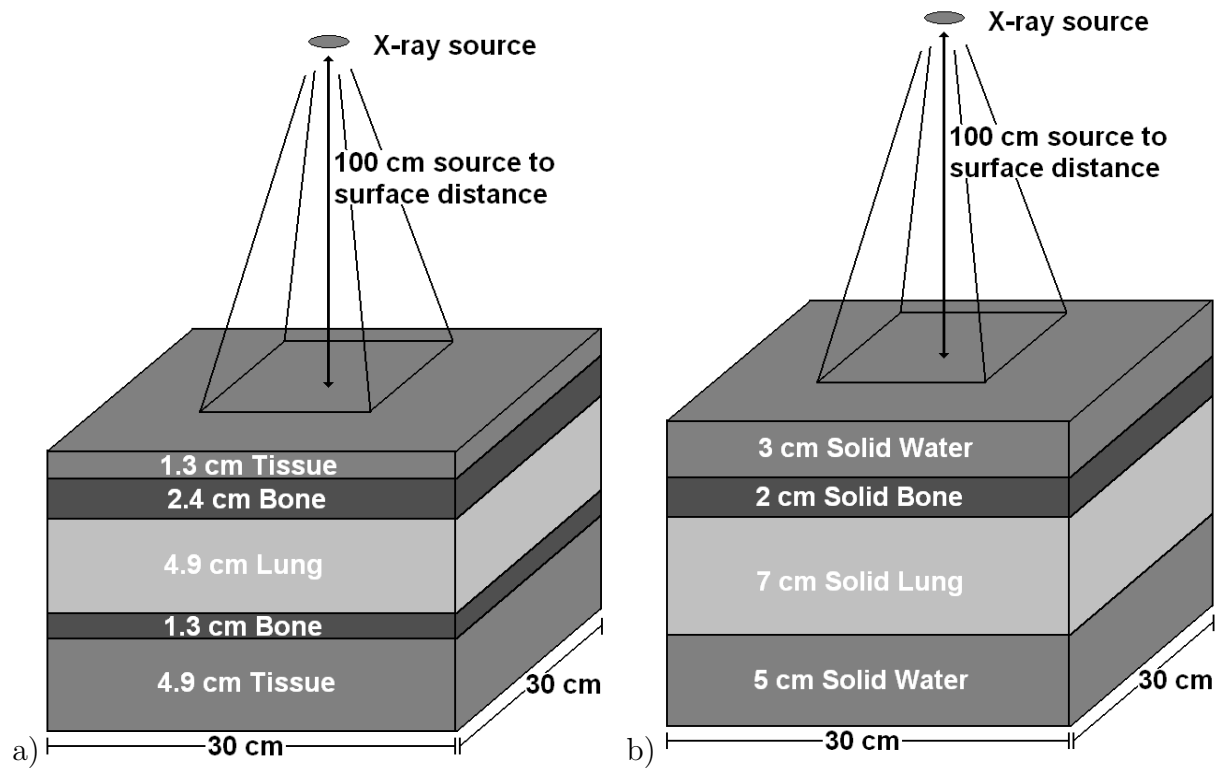
Figure 2.1: The heterogeneous block phantoms used in (a) the beam quality sensitivity analysis, and (b) the experimental validation of the source characterization.

the Monte Carlo generated reference spectrum fully resolves the characteristic peaks whereas the spectra generated by Spektr amalgamated these into two wide peaks.

We also investigated the sensitivity of x-ray dose to the x-ray tube's peak potential (kVp). While kVp cannot be measured directly from the x-ray beam, there exist a number of commercial meters that will report a beam's kVp within 2%[168, 74]. Therefore, we analyzed multiple spectra with tube potentials ranging from 120-130 kVp, each with a HVL of exactly 4.337 mm Al, to cover a range of spectra representative of the uncertainty in kVp one might expect from a diagnostic x-ray unit and kVp measurement device (i.e., 1-2 kVp).

Dose Calculations

The x-ray dose is computed according to the method described by Kouznetsov and Tambasco[103]. In this method, dose is computed at a point of interest (POI) by calculating the primary beam component deterministically and the scatter component of the beam stochastically. More specifically, the scatter component of the beam is separated into a first collision and a multi-collision contribution, both computed using biased Monte Carlo techniques incorporating the relevant basic interactions (i.e., photoelectric effect, coherent scattering, and incoherent Compton scattering).

In general, CT images are used to provide the spatial and Hounsfield Unit (HU) information of the volume in which dose is computed. To dissociate errors due to the imaging process (e.g., noise, imaging artifacts, and reconstruction errors) from errors due to the characterization process or our dose computation algorithm, we used idealized images of the homogeneous and heterogeneous block phantoms (Fig. 2.1), i.e., images free of noise, artifacts, and reconstruction errors, instead of real CT images. The images were constructed using MATLAB$^{®}$, and saved in the DICOM format. The dimensions and materials of the block phantoms were reproduced and consisted of 512×512×91 voxels (23.8 million total), each of size 0.081×0.081×0.30 cm^3.
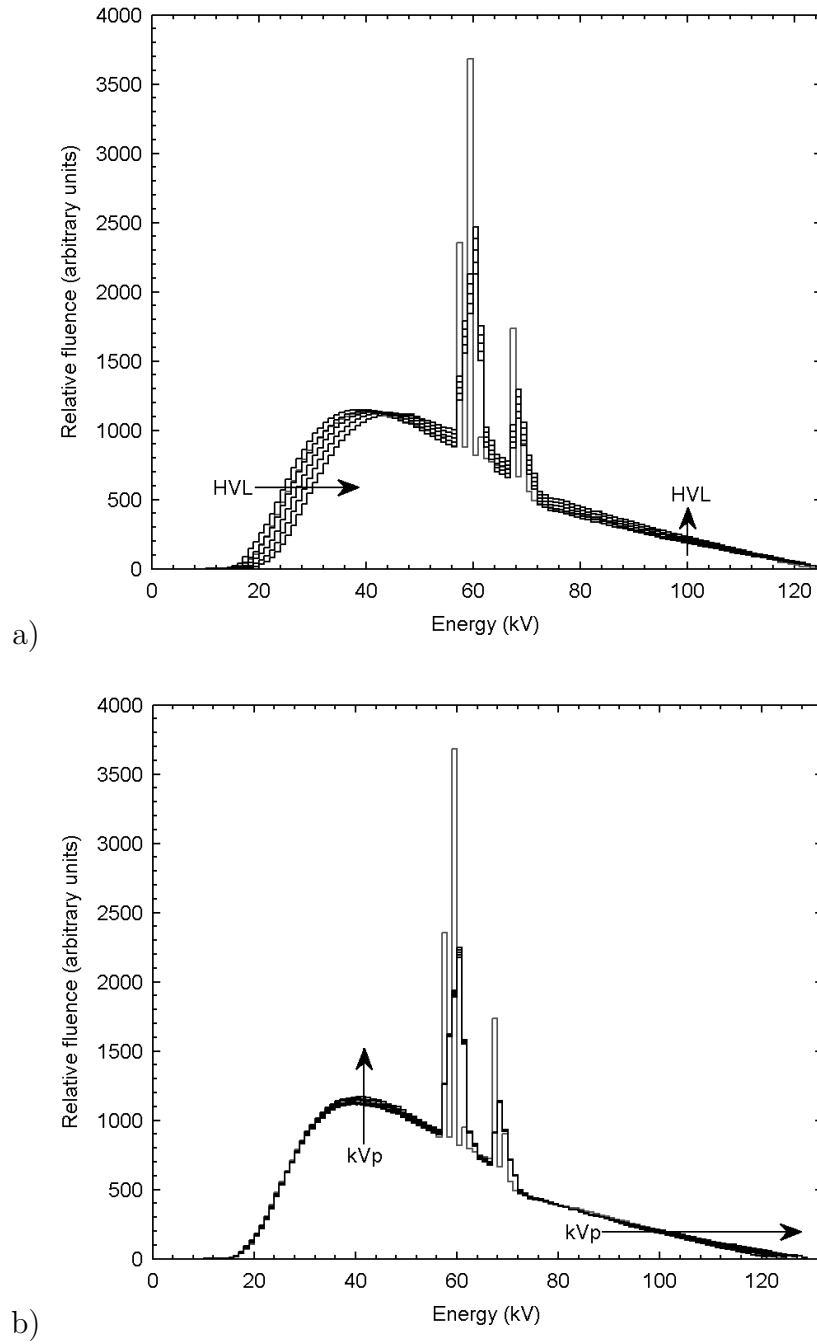
Figure 2.2: (a) Spectra of varying HVL and (b) varying kVp that were used in the sensitivity analysis. Arrows denote the direction of increase in the parameter illustrated.

In the approach developed by Kouznetsov and Tambasco[103], HU ranges were associated with physical density ranges, which were attributed to different materials. These materials were assigned an elemental composition by the user by specifying the elements and their corresponding nuclear densities. Final interaction macro cross-sections are calculated using the ENDF/B-VI micro cross-section library[129].

For all dose computations, dose from a single x-ray projection was computed in water for the homogeneous case and in lung, bone, and tissue for the heterogeneous case (Fig. 2.1a). The x-ray source was positioned along the central axis of the block phantoms 100 cm above their surfaces. The material compositions of the tissues in the heterogeneous phantom were obtained from ICRU report 46[82]. Tissue-mimicking materials were used for the experimental validation of our kV source spectrum characterization, and in our in-house computation software[103]. For the homogeneous block phantom, we used Gammex 457 Certified-Therapy Grade Solid Water$^{®}$ (Gammex 457 CTG Solid Water$^{®}$), Gammex, Inc, Middleton, Wisconsin, USA. For the heterogeneous block phantom (Fig. 2.1b), we also used Gammex Tissue Equivalent Materials for lung (Gammex 455) and cortical-bone (Gammex 450). For experimental ease, the dimensions of the materials were changed from the ones used for the heterogeneous phantom in the sensitivity analysis (cf., Fig. 2.1a and Fig. 2.1b). The material composition of these structures was obtained from the manufacturer as atomic mass percentages, and we used these to calculate atomic density (expressed as the number of nuclei/m^3, a necessary parameter for the dose computation algorithm) for all the material components.

X-ray dose was calculated using our in-house software[103] and four Intel$^{®}$ CoreTM 7 960 CPU at 3.20 GHz for each POI. An average of 24 seconds was required to compute dose at a POI. The number of POIs depended on the nature of the computation (percent depth dose versus profile dose), but it ranged between 40 and 70 for a total maximum time of approximately 28 minutes.
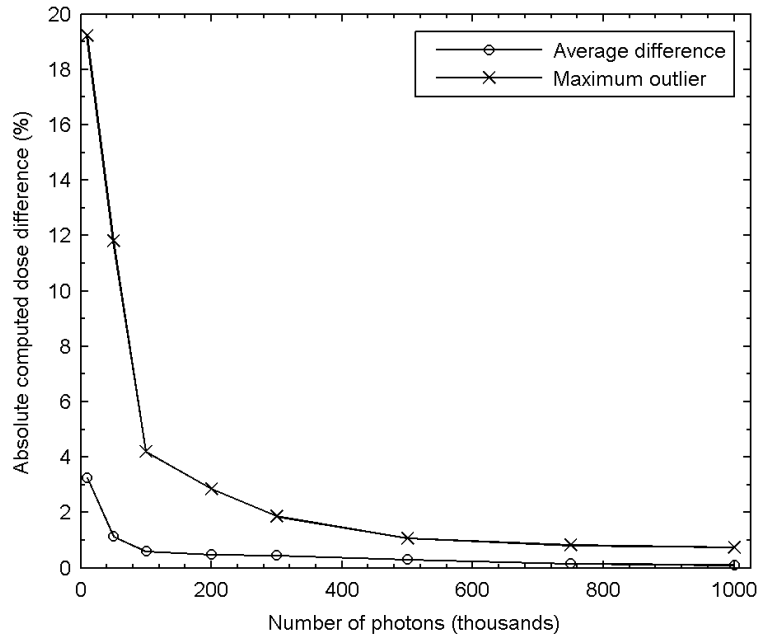
Figure 2.3: Effect of the number of photons on the computed dose. The dose is computed in water for 10 equally spaced points that are separated by 1 cm up to a depth of 10 cm. Both the maximum difference and the average difference are plotted.

The use of fewer photons speeds up computational time exponentially, but increases statistical noise for situations in which most of the beam has been attenuated such as at greater depths or in high-density material (e.g., bone). In this study, we used 1.5 million photons to calculate dose. Figure 2.3 shows the relative difference between computations performed using 1.5 million photons and computations using photons ranging from 10 thousand to 1 million photons. Figure 2.3 shows that the computational accuracy in the dose does not vary greatly (average variation within 1%) for calculations performed using 500 thousand to 1.5 million photons. However, some points vary by more than 2% when less than 500 thousand photons are used.

Experimental Validation

We made anterior-posterior x-ray projection measurements using the Varian® OBI® system with an open field and no added filtration. A field size of 10×10 cm^2 was used for the homogeneous block phantom measurements. For the heterogeneous phantom field sizes of 5×5 cm^2, 10×10 cm^2, and 20×20 cm^2 were used for the 125 kVp beam, and the 10×10 cm^2 field size was used for the 80 kVp and 100 kVp beams. The technique settings for the dose measurements were 80, 100 and 125 kVp with a 160 ms pulse length and a 160 mA tube current. These settings were chosen to maintain a high signal-to-noise ratio at depths greater than 11 cm while minimizing the risk of overheating the x-ray tube over the course of many measurements. All doses were taken to be the average of three measured doses. The standard deviation of the average of these three measurements was calculated to provide an estimate of the reproducibility of the measured dose; however, except for HVL measurements where small (0.1%) measurement uncertainties propagated to form larger HVL uncertainties, the resulting experimental uncertainties were too small to be visible graphically. As we normalized measured dose to a depth of 2 cm, we did not have to consider inter-session changes in the source output. Measurement uncertainty could be as much as 2 mm systematically in the case of a misaligned phantom or positional lasers, which could change the value of measured dose by up to 1%, which is relatively small due to the relative flatness of the beam. Similarly, random shifts of up to 1 mm due to movement of the phantom along on the x-axis could change the value of measured dose by up to 0.5%. According to Svensson, uncertainties arising from measuring megavoltage (MV) dose with ion chambers can reach 2.1% due to fluctuations in chamber response, exposure rate, and local calibration[160]. If these uncertainties are added in quadrature, they would represent an overall dose measurement uncertainty of 2.4%.

The HVL of three OBI® systems at the authors' institution were evaluated. The measurements were made with a 0.06 cc PR-06C Capintec farmer-style chamber (Capintec Inc., Ramsey, NJ, USA). The chamber was calibrated for photons in the kV energy range at 70, 100, 120 and 150 kVp. Since the calibration factor varied by less than 0.3% over the relatively large range of beam qualities, we simply neglected changes in response between calibration quality and in-phantom radiation quality. To determine the HVL, we used a three point semi-logarithmic interpolation technique[73]. With this technique, HVL is interpolated using Eq. 2.1 and measurements of doses D0, D1, and D2 corresponding to an unfiltered beam, and a beam filtered by aluminum thicknesses of T_1 and T_2, respectively[73]. These aluminum thicknesses were placed directly on the kV unit.

$$HVL = \frac{T_1 ln \left(2\frac{D_1}{D_0}\right) - T_2 ln \left(2\frac{D_2}{D_0}\right)}{ln \left(2\frac{D_1}{D_2}\right)} \tag{2.1}$$

The thicknesses T_1 and T_2 were chosen such that the HVL would be greater than T_1 and less than T_2. For the characterization of the 80 and 100 kVp beams T_1 and T_2 were 1.53 ± 0.02 and 3.00 ± 0.03 mm Al, respectively, and for the characterization of the 125 kVp beam, they were 3.07 ± 0.03 and 6.12 ± 0.06 mm Al, respectively.

To investigate the relationship between beam quality and field size and how they affect dose accuracy, the half-value layers for the 125 kVp beam were measured for field sizes ranging from 5 × 5 cm² to 40 × 40 cm² defined at a distance of 100 cm from the x-ray source. Uncertainties were obtained by propagating the uncertainty in the measurement values in Eq. 2.1 following the method outlined by Hill *et al.*[73].

Relative dose measurements were taken inside the homogeneous and heterogeneous (Fig. 2.1b) block phantoms using the same 0.06 cc PR-06C Capintec ion chamber used to measure the HVL. The ion chamber was placed inside a 2 cm thick slab of the relevant material (i.e., solid water, lung or bone) via a cavity that was drilled to the specific volume and geometry

of the chamber. The block phantom was placed on the Varian® linear accelerator couch with the gantry rotated at 90 degrees to have the kV source perpendicular to the top surface of the block phantom. The depth dose measurements were made by exchanging the 2 cm slab of filled material at each measurement depth with a slab of the same material containing the ion chamber. The profile measurements were made by shifting the entire structure laterally via the couch controls and using a ruler and the overhead laser to monitor lateral displacement. The profile measurements were made using the smaller field (10×10 cm^2) to preserve sufficient material for the contribution of dose from possible photon side-scatter.

As the chamber was calibrated for dose in water, we applied conversion factors when measuring dose to bone or lung-equivalent materials. These conversion factors were the ratio of mass-energy absorption coefficients for the relevant materials obtained from Ma and Seuntjens[112]. A publication by The American Association of Physicists in Medicine (AAPM) Radiation Therapy Committee Task Group 61 (TG-61)[111] advises performing HVL measurements in narrow-beam geometry to avoid errors due to collimator scatter. However, this contamination from scatter contributes to the x-ray dose absorbed by a patient; hence, we investigated the variation of HVL with field size to assess its effect. According to TG-61, the conversion factor from dose-to-water to dose-to-medium is given by[111]

$$C_w^{med} = \frac{B_{med}}{B_w} \cdot \left[(\bar{\mu}_{en}/)_w^{med} \right]_{air}, \tag{2.2}$$

where $(\bar{\mu}_{en}/)_w^{med}$ is the in-air mass energy-absorption coefficient ratio of the medium to that of the water averaged over the primary photon spectrum (using HVL as the sole beam quality identifier), and B_{med}/B_w is the ratio of the backscatter factor of the medium to that of the water. Values for these factors were obtained from Appendix B.3 of TG-61[111]. As there are no published values for Gammex Solid Water® Tissue Equivalent Materials for tissue, lung, and cortical bone materials used in the study, we used the values for normal tissue, lung, and bone, respectively.

2.2.4 Results and Discussion

Sensitivity of X-ray Dose to HVL and kVp

As expected, changes in beam quality lead to changes in absorbed dose inside the phantoms. This is evident in Figs. (2.4) and (2.5), which show that softer beams with a lower HVL or kVp (expressed as a variation over the base of the 125 kVp, 4.337 mm Al Monte-Carlo generated beam) deposit more dose near the surface while harder beams with a higher HVL or kVp deposit more dose at greater depths. The percent difference between the spectrum that had the same HVL and kVp as the baseline spectrum is less than 0.1% for all points in both the homogeneous and the heterogeneous block phantom; this suggests that Monte Carlo modeling of the source spectrum is not necessary for accurate dose computation and the use of Spektr[153] is sufficient.

It is generally known that beam quality depends on kVp, the maximum energy of a beam, as well as HVL, which is a common descriptor of beam quality. Since interaction cross-sections in the kV range generally decrease with energy[89], we expect beams with higher kVp and higher HVL to be more penetrating so that absorbed dose will increase with increasing depth depths compared to a less penetrating beam (and vice-versa). However, as HVL and kVp are used to characterize a beam for quality assurance purposes rather than quantitative dose computation, studies seldom focus on the degree to which these parameters affect dose computation accuracy. Figures 2.4 and 2.5 show that, beam quality depends on HVL and kVp.

When the HVL was varied (Fig. 2.4), the greatest percent dose difference between the generated spectra and the Monte Carlo generated spectrum was observed at the surface for both the heterogeneous (Fig. 2.4a) and the homogeneous (Fig. 2.4b) phantoms. At greater depths (more than 2.8 cm for the homogeneous phantom and beyond the bone layer for the heterogeneous phantoms) the percentage dose difference relative to the baseline spectrum

Figure 2.4: Computed relative dose differences between the Spektr generated spectra and the reference Monte Carlo spectrum[46] as a function of depth for varying HVL in (a) the heterogeneous phantom, and (b) the homogeneous phantom. Curves are labeled according to their associated variation in HVL.
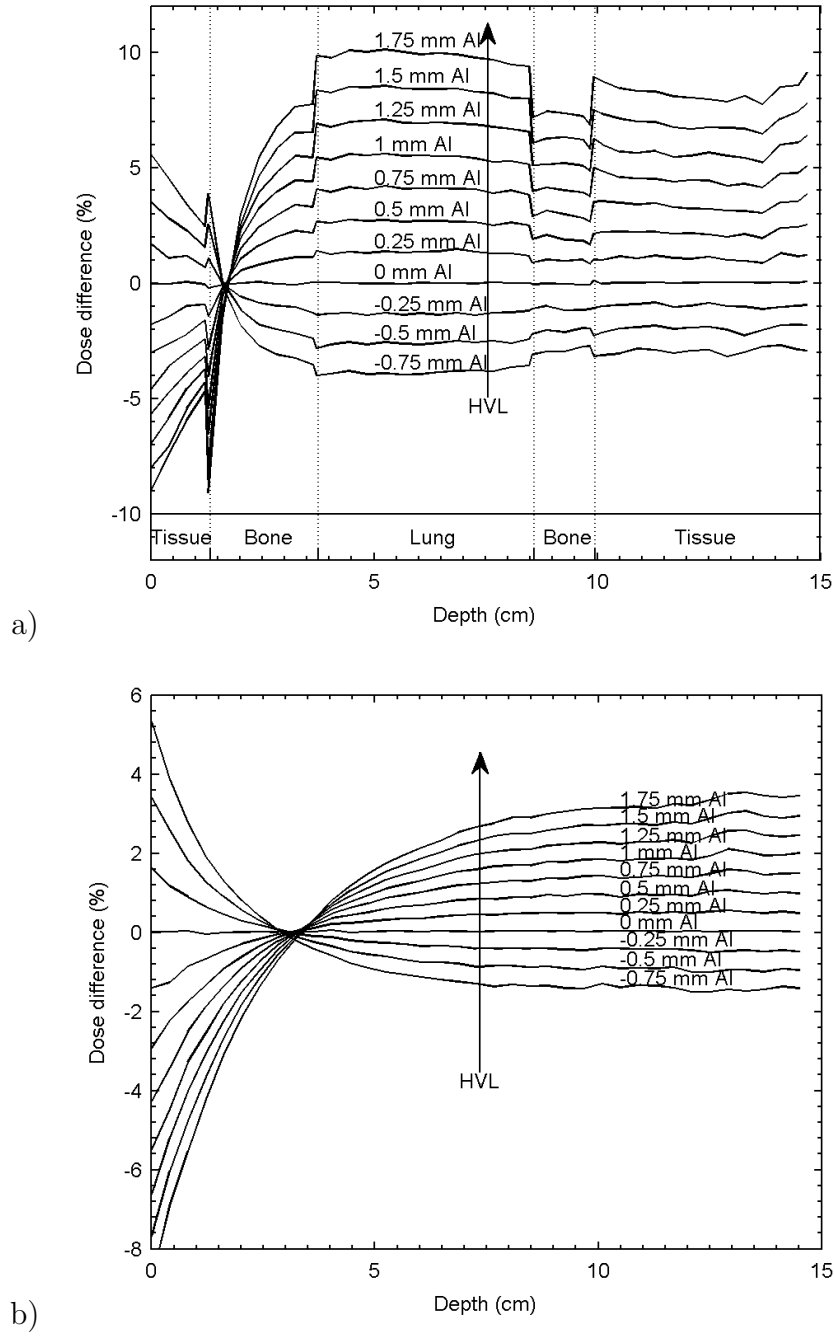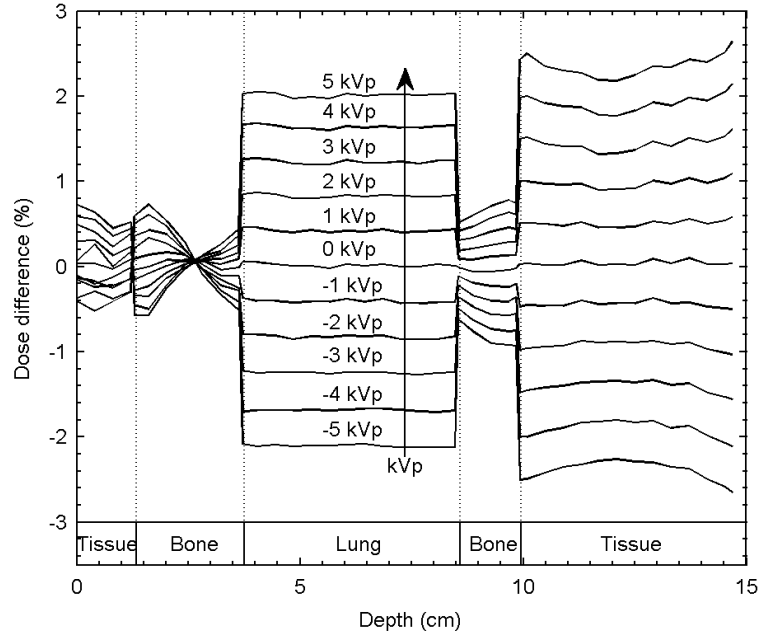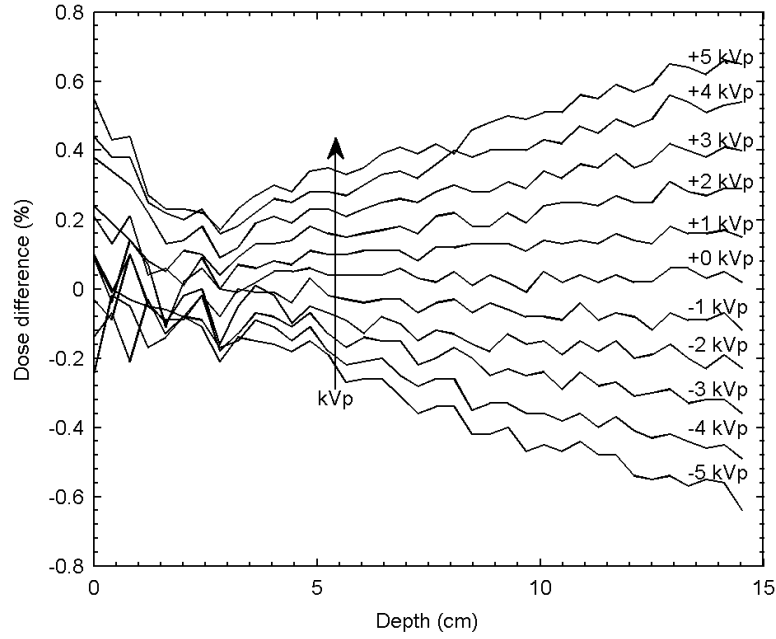
a)

b)

Figure 2.5: Computed relative dose differences between the Spektr generated spectra and the reference Monte Carlo spectrum[46] as a function of depth for varying kVp in (a) the heterogeneous phantom, and (b) the homogeneous phantom. Curves are labeled according to their associated variation in kVp.

becomes fairly constant for each material and HVL variation. When the kVp was varied (Fig.2.5), the difference within the heterogeneous phantom (Fig. 2.5a) become important only when the beam crosses the bone-lung and the bone-tissue interfaces where differences increase to 2 to 2.5%. Within the homogeneous phantom (Fig. 2.5b), the difference varies by less than 1% even for a 5 kVp variation.

As HVL is varied, the relative percentage dose difference exhibits a fairly constant behavior until it reaches a certain depth, and the crossover from negative to positive relative difference occurs at about the same depth, between 1.6 to 1.7 cm for the heterogeneous (Fig. 2.4a) and 2.9 to 3.4 cm for the homogeneous (Fig. 2.4b) phantoms, respectively. In the kVp analysis, the crossover occurs between 2.6 to 2.8 cm for the heterogeneous phantom (Fig. 2.5a) and does not occur within the homogeneous phantom (Fig. 2.5b). Beams with differing kVp are seen to be particularly affected by high-Z materials (Fig. 2.5a), whereas beams that possess a similar HVL are seen to have similar radiological properties in water-equivalent material regardless of kVp (Fig. 2.5b).

The various spectra were normalized to the same number of particles. Hence, a higher HVL leads to a greater proportion of high energy photons. Likewise, a higher kVp (keeping HVL constant) leads to both more high-energy and low-energy photons, but fewer photons in the mid-energy range. When the beam is heavily attenuated, such as at greater tissue depths or after crossing a bone layer, low energy x-rays are preferentially absorbed via the photoelectric effect thus hardening the beam. As a result, beams with a higher HVL (or kVp in the heterogeneous phantom) are left with a greater proportion of high-energy photons, explaining the higher dose at greater depths for these beams.

The fairly constant percent dose difference relative to the baseline spectrum is due to the interaction coefficient for Compton scattering, which is more dominant at energies greater than 60 keV and does not depend strongly on energy in the 60 to 125 keV range[89]. Thus, the behavior of the beam will mostly depend on the surviving number of high-energy photons

once the low-energy component has been attenuated. There was no strong relationship between kVp and dose deposition behavior in the homogeneous phantom. This may be because HVL is the main factor determining the penetration ability of the beam in the absence of a bone layer to preferentially absorb low-energy photons.

As uncertainties in HVL and kVp can be measured to within 0.1 mm Al and 1 kVp, respectively, the uncertainty in computed x-ray dose due to these source parameter uncertainties is within 0.5% for variations in both HVL and kVp. While these results are specific to the phantom and the beam quality used in the sensitivity analysis, they provide a good estimate of the relative importance of HVL and kVp on dose computation.

Figure 2.6 shows the average dose difference for HVL and kVp variations in the 125 kVp beam over the entire depth of the phantom (15 cm). The percent difference in dose computation in both phantoms is fairly linear with HVL and kVp variation. In the homogeneous phantom, the slope is 1.6%/mm Al for HVL variations and 0.1%/kVp for kVp variations, while in the heterogeneous phantom, the slope is 4.6%/mm Al for HVL variations and 0.5%/kVp for kVp variations, respectively.

HVL Direct Measurement

While there is some dependence of the HVL of the 125 kVp beam on field size, Fig. 2.7 shows that variations of HVL with field size are about 0.1 mm Al over the entire range of the fields (5×5 cm^2 to 40×40 cm^2). The significance of this result is that it shows that the characterization of the spectrum by the HVL does not change significantly with the field size and is within measurement uncertainty. As shown with the sensitivity analysis for beam quality (Fig. 2.4), small variations in HVL (0.1 to 0.2 mm Al) lead to small changes in dose computation (0.5 to 1%). Therefore, a single value of HVL is sufficient to calculate dose to within 1% independent of field size for the case of the 125 kVp beam. In future work, we will investigate the spatial variation of HVL with and without the addition of external filtration
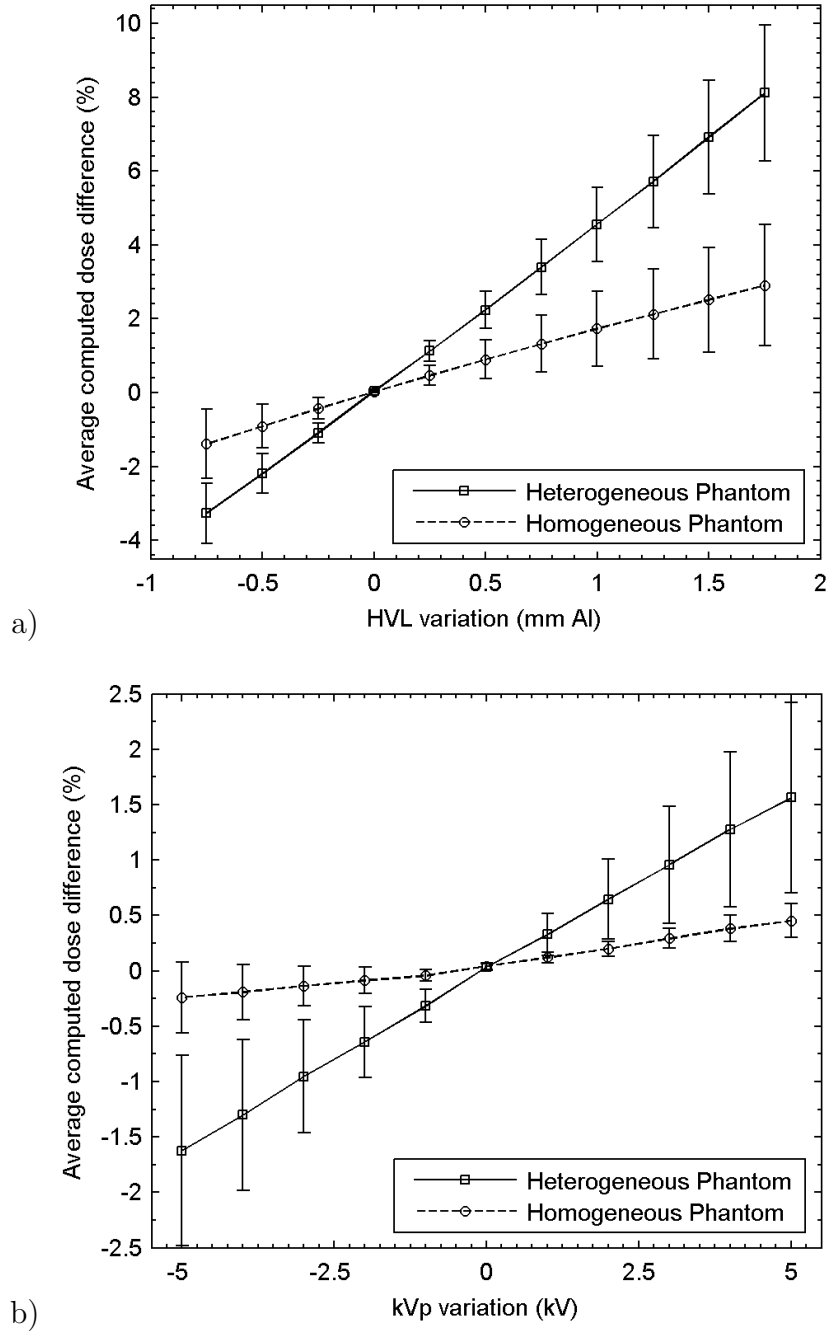
Figure 2.6: Computed average percentage dose difference over the entire depth of the phantom (15 cm) between the Spektr generated spectra and the reference Monte Carlo spectrum[46] as a function of depth in both phantoms for (a) variations in HVL, and (b) kVp. Error bars depict standard deviations.
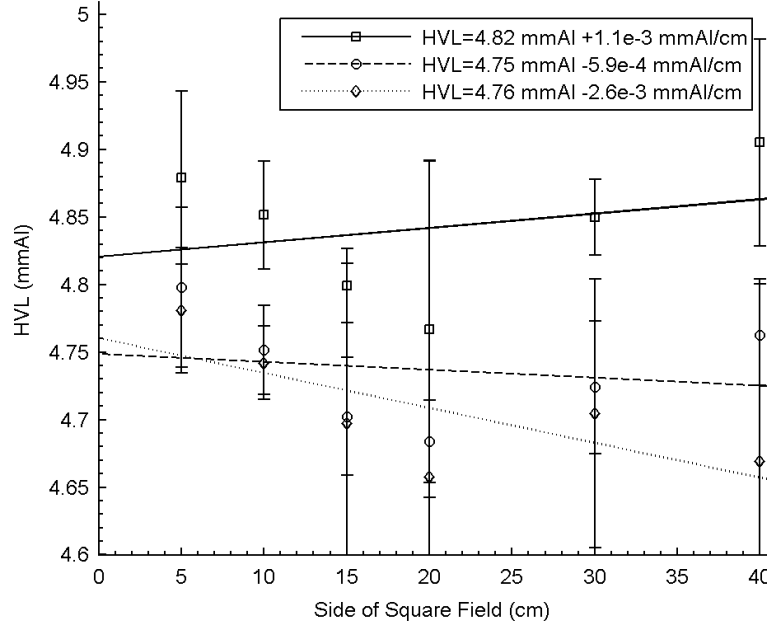
Figure 2.7: Measured HVL as a function of field size for three 125 kVp OBI® units. The HVL is measured at the centre of the beam.

such as half- or full-bowtie filters.

Experimental Validation

For both the homogeneous (Fig. 2.8) and the heterogeneous (Figs. 2.9 and 2.10) phantoms, relative dose measurements agreed with computation to within 2 and 4%, respectively, except for the positive off-axis direction of the dose profiles (Figs. 2.8b and 2.10). All profiles except the 125 kVp beam in the homogeneous phantom show dose agreement becoming progressively worse (up to 6%) along the positive off-axis distance direction. The authors suspect that the Monte Carlo generated beam fluence used to compute dose may be greater than the actual fluence of our OBI® source on the positive edge of the x-axis resulting in the discrepancies in that region of the field. Nevertheless, a 6% dose difference still represents reasonable agreement between the computed and measured dose profiles.

To the authors knowledge, there is currently no accepted standard for the accuracy of
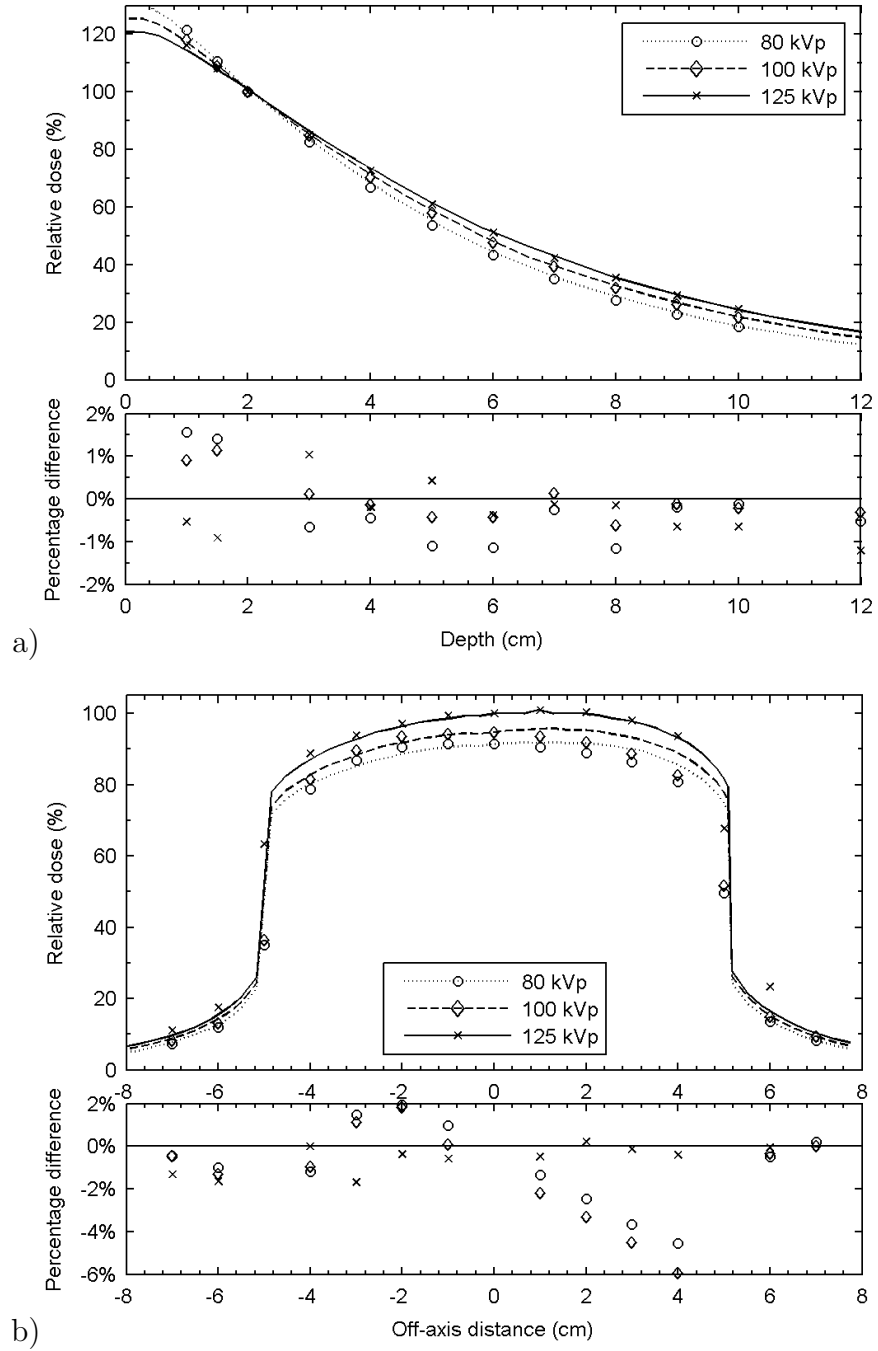
Figure 2.8: Percent depth dose for the homogeneous phantom at (a) the center of the beam and (b) transverse dose profile at a 2 cm depth. Doses are normalized to the 2 cm depth. Computed dose (line) is compared to the measured relative dose (circles).
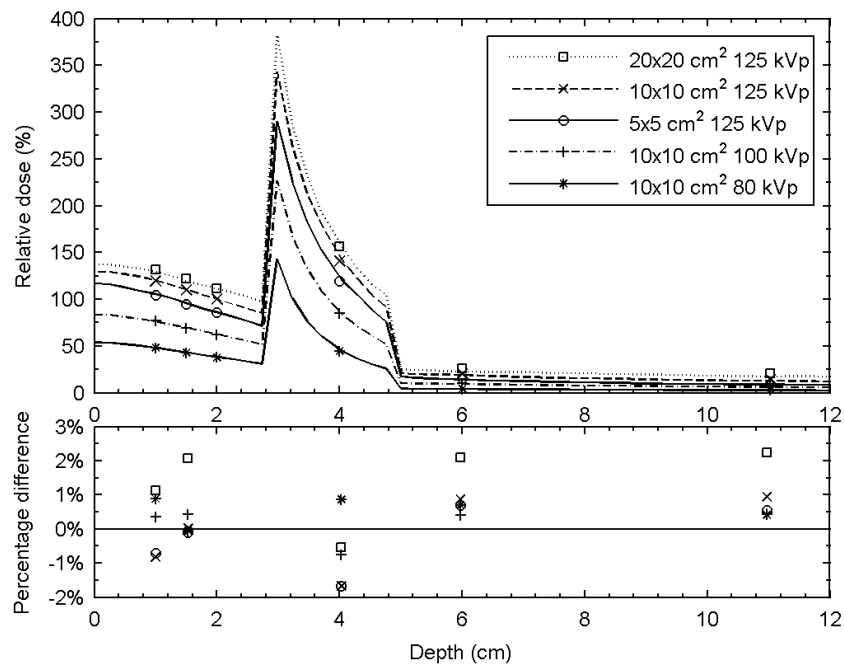
Figure 2.9: Percent depth dose for the heterogeneous phantom at the center of the 125 kVp beam. The dose was normalized to a depth of 2 cm. Computed dose (line) is compared to the measured relative dose (circles).
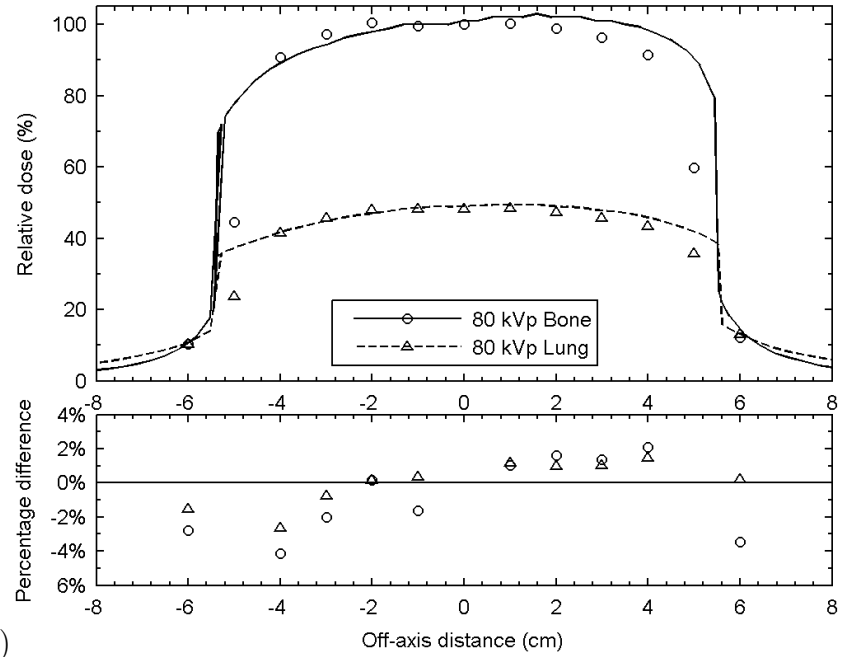
a)
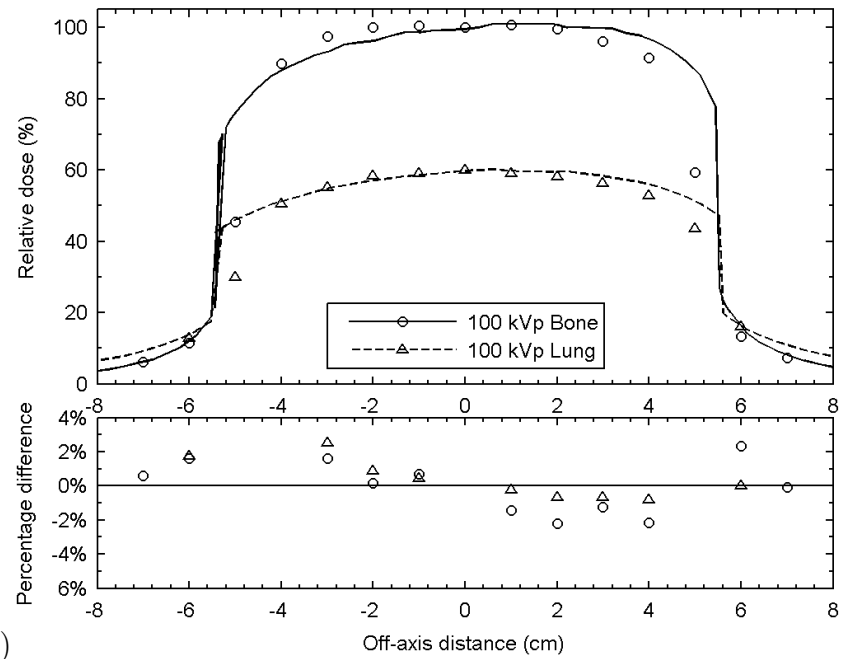
b)
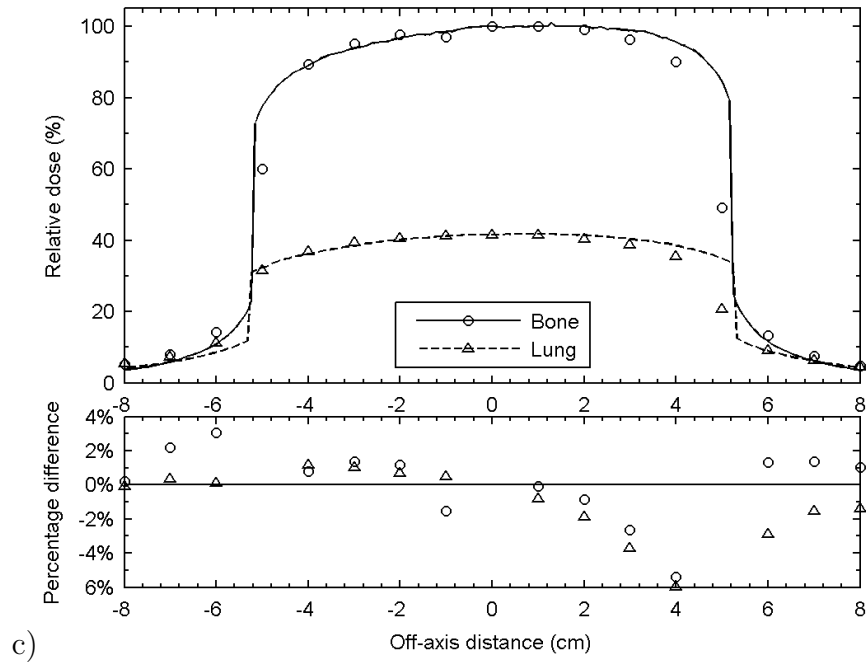
Figure 2.10: Transverse dose profile for the heterogeneous phantom for an (a) 80 kVp beam, (b) 100 kVp beam, and (c) 125 kVp beam in bone (4 cm depth) and lung (6 cm depth). The doses are normalized to the center of the beam in bone for all profiles. Computed dose (line) is compared to the measured relative dose (circles).

patient-specific IGRT dose calculations. If one is to eventually incorporate IGRT dose in treatment plans, it is not unreasonable to expect that existing guidelines for the accuracy of computed treatment planning dose would also be applied to imaging dose. The average uncertainties in our calculations in the heterogeneous phantom were 0.9 to 1.8%, with a maximum uncertainty of 6%. These uncertainties are comparable to the uncertainties in the accuracy of MV treatment planning dose calculations, which have been estimated to be between 2 to 4.4%[172].

Our in-house hybrid dose computation method was previously validated with MCNP and EGSnrc[103], and this study provides experimental validation and shows that the source spectrum can be characterized by HVL and kVp with accurate dose computation. In the future, further characterization of the beam fluence would be needed to investigate differences between x-ray tubes of the same model, and to account for spatial variations in the beam fluence arising from the bowtie filters commonly added to CBCT imaging systems used in radiotherapy. We are currently investigating the use of GAFCHROMIC^{TM} XR-QA2 (International Specialty Products, Wayne NJ), a radiochromic film that is sensitive to low doses (0.1 to 20 cGy) and low energies (20 to 200 keV), to characterize the spatially-varying change in HVL and beam fluence using the film characterization procedure described by Tomic *et al.*[167] Alternatively, the required set of fluence fields for a given x-ray tube type and added bowtie filter could be generated using Monte Carlo modeling of the tube, as done by Ding *et al.*[46]

In future work we will also perform further experimental validation of our spectral characterization and in-house hybrid dose computation method using an anthropomorphic phantom. In addition, future validation of our approach for CBCT imaging would need to account for spatial variations in the beam fluence arising from the commonly added bowtie filters, and validating our approach with different OBI$^{®}$ units.

2.2.5   Conclusion

In this study, we have investigated the feasibility of using a simplified method for characterizing the spectrum of an x-ray source as part of a novel approach for modeling a kV imaging device for machine-specific radiation dose computation. Our investigation of the sensitivity of dose computation accuracy on beam quality parameters (i.e., HVL, kVp, and field size) shows that the measurement uncertainty of 0.2 mm Al in HVL results in a dose uncertainty of less than 1%, making HVL a useful parameter to characterize beam quality for this purpose. We have also shown that a spectrum generated by interpolation based on HVL and kVp can be used to calculate dose to within 0.1% of the baseline Monte Carlo generated spectrum[46]. Hence, HVL and kVp are suitable parameters for characterizing a kV x-ray source spectrum for kV dose calculations. Furthermore, we have shown that HVL varies by about 0.1 mm Al with variations in field size, suggesting that one characterization of the source spectrum is sufficient for all field sizes if no additional filtration is used.

While the main goal of the study was to validate the proposed source characterization method, it is worth noting that we have also validated our in-house dose calculation algorithm by performing experimental relative dose measurements for three different tube potentials (80, 100, and 125 kVp). We have shown that the computed central axis depth doses agree with measurement to within 2% for both the homogeneous and heterogeneous block phantoms. The profile doses agree with an average deviation of 1.8%, and a maximum deviation of 2% and 6% for the for the homogeneous and heterogeneous phantoms, respectively. These results show that the HVL and kVp are sufficient to characterize beam spectra for accurate kV dose computation.

These results bring us one step closer to the development and validation of an accurate patient-specific dose computation system for kV IGRT imaging procedures. Future work will focus on further experimental validation of our kV dose computation system using an

anthropomorphic phantom, and modeling the CBCT source rotation and imaging filters in our in-house hybrid dose computation method[103].

2.3   Erratum: A simplified approach to characterizing a kilovolt-age source spectrum for accurate dose computation [Med. Phys. 39(6), 30413050 (2012)]

Y Poirier[1], A Kouznetsov[1], and M Tambasco[2]

[1] Department of Physics and Astronomy, University of Calgary, Calgary, Alberta T2N 4N2, Canada

[2] Department of Physics and Astronomy and Department of Oncology, University of Calgary, Calgary, Alberta T2N 1N4, Canada and Department of Physics, San Diego State University, San Diego, California 92182-1233, USA

We would like to draw your attention to a small error that we recently discovered in our published manuscript (Medical Physics, 2012, 39(6), pp. 3041-3050) describing the validation of a kV spectral characterization method. Equation 2.2 in the manuscript was used to convert dose-to-water to dose-to-medium in bone and lung-equivalent materials at a depth of 4–6 cm. However, this equation, taken from the AAPMs TG-61 report outlining dosimetry protocols in the kV energy range, was meant only for surface dose conversions. At a depth of 4 cm, the conversion of dose-to-water to dose-to-bone should consist simply of the ratio of mass-energy absorption coefficients ($(\bar{\mu}_{en}/\rho)^{w}_{med}$), and not include the bone-to-water backscatter factor ratio (B_{med}/B_{w}).

This error affects the measured point in bone-equivalent material depicted in Fig. 2.9 below by decreasing the agreement in local dose from $\leq 3\%$ to $\leq 6\%$. The measured points in lung-equivalent materials were unaffected because the backscatter factor ratio was used only for the bone slab comparison.

While the agreement of $\leq 6\%$ is larger than previously reported, it remains within experimental uncertainty. As the uncertainty in the position of the ionization chamber is within
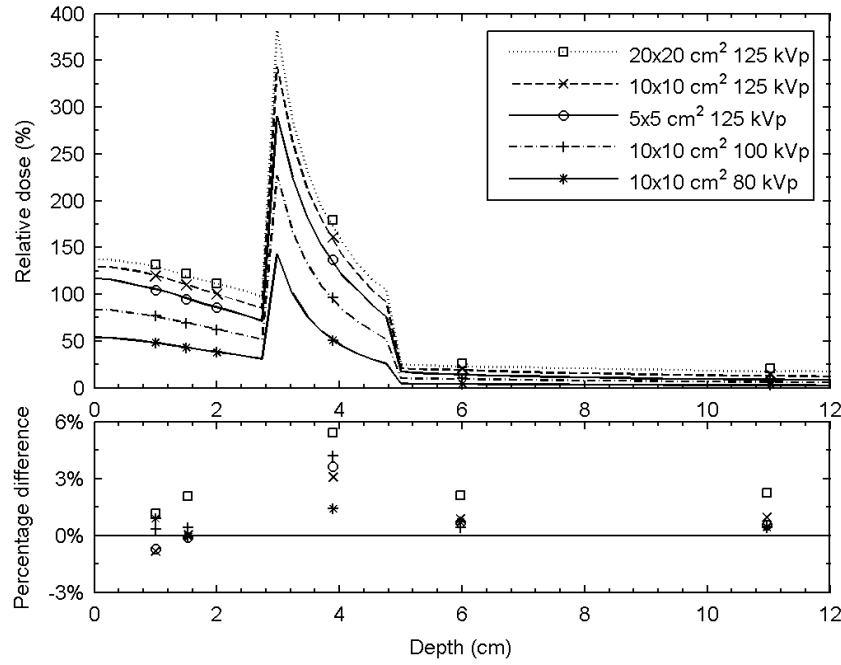
Figure 2.11: Percent depth dose for the heterogeneous phantom. The dose was normalized to a depth of 2 cm at the center of the 125 kVp beam. Computed dose (line) is compared to the measured relative dose (circles).

half of an in-slice side length of a voxel ($\pm$0.4 mm), and the local dose gradient is $\geq 7\%$/mm at the measurement point, there is a $\sim$5% uncertainty in local dose due solely to the position of ionization chamber.

Furthermore, additional uncertainties arise from ion chamber response (2.4%, section 2.2) and the proposed beam characterization method (1%, section 2.3). If we add these in quadrature, we obtain an experimental uncertainty of 5.5%, placing all corrected measurements within experimental uncertainty of the computed doses.

It should be noted that the corrected results for the bone slab do not detract from the conclusions of the paper, as they still provide validation of the computed doses within experimental uncertainty.

2.4 General Conclusions

The spectrum characterization method we presented in this manuscript was able to calculate the absorbed dose in a homogeneous and heterogeneous block phantom with reasonable accuracy. However, the use of a single third-party fluence for all three beams led to decreasing accuracy in transverse axis profiles for the lower energy beams. The beams used for CBCT usually comprise added bowtie filtration to decrease the patient dose; these beams are highly attenuated with a high variation in photon intensity and energy across their profile. Clearly, it is preferable to characterize beam-specific spatial variations of the fluence and spectrum to accurately compute the dose delivered by CBCT beams.

These concerns are addressed in the next chapter where we propose and validate a complete spatial fluence and spectral characterization method based on similarly simple empirical measurements. We use this characterization to construct the final form of the virtual point source proposed in this thesis.

Chapter 3

Fluence characterization and virtual source model

3.1 General Introduction

This chapter introduces the formalism of the source characterization method and virtual point source we use to compute the dose with kVDoseCalc. Like in the previous chapter, the HVL and kVp are used to characterize the spectrum; however, while a single spectrum defined the entire beam in the previous chapter, here we measure HVL across the transverse axis. Using this spatially-varying spectrum, we extract the fluence across the transverse and radial axes, which are then multiplied together to form the 2-D isocentre planar fluence. This characterization is used to construct a simplified virtual point source of the kV source, in turn used to carry out the dose computation. We validate the virtual point source and characterization method for radiographic exposures using square field sizes of four different filter/energy combinations corresponding to the default CBCT imaging procedures of the imaging unit used in our institution.

The remainder of this chapter was submitted in a peer reviewed journal, *Medical Physics*[137] on July 1, 2013. It is currently under review since July 23, 2013. I was the first author of this manuscript while Dr. Alexei Kouznetsov and Dr. Mauro Tamsbasco were contributing authors. I designed the characterization method and suggested the general form of the virtual point source. In consultation with Dr. Alexei Kouznetsov, I designed the general idea of the virtual point source and the GUI in which the user can input the various quantities required to construct the virtual point source. Dr. Alexei Kouznetsov carried out the modifications of KVDoseCalc's source code required to implement the virtual point source and GUI. I designed and carried out the experiments and measurements that we use to validate our ap-

proach. Dr. Mauro Tambasco provided support throughout the project, notably suggesting that the fluence measurements be done by ionization chamber measurements rather than radiochromic film. This suggestion was instrumental to the success of the study in light of the energy dependence of XR-QA radiochromic film. I wrote the first draft of the manuscript, and the contributing authors helped review and revise it throughout the submission process.

3.2 Experimental validation of a kilovoltage x-ray source model for computing imaging dose

Y Poirier[1], A Kouznetsov[1], and M Tambasco[1,2]

[1] Department of Physics and Astronomy, University of Calgary, Calgary, Alberta T2N 4N2, Canada

[2] Department of Oncology, University of Calgary, Calgary, Alberta T2N 1N4, Canada and Department of Physics, San Diego State University, San Diego, California 92182-1233, USA

3.2.1 Abstract

Purpose: To introduce and validate a kilovoltage (kV) x-ray source model and characterization method to compute absorbed dose accrued from kV x-rays.

Method and materials: We propose a simplified virtual point source model and characterization method for a kV x-ray source. The source is modeled by: 1) characterizing the spatial spectral and fluence distributions of the photons at a plane at the isocentre, and 2) creating a virtual point source from which photons are generated to yield the derived spatial spectral and fluence distribution at isocentre of an imaging system. The spatial photon distribution is determined by in-air relative dose measurements along the transverse x- and radial y-directions. The spectrum is characterized using transverse axis half-value layer (HVL) measurements and the nominal peak potential (kVp). This source modeling approach is used to characterize a Varian® on-board-imager (OBI®) for four default cone-beam CT beam qualities: beams using a half bow-tie filter (HBT) with 110 and 125 kVp, and a full bow-tie filter (FBT) with 100 and 125 kVp. The source model and characterization method was validated by comparing dose computed by our in-house software (kVDoseCalc) to rel-

ative dose measurements in a homogeneous and a heterogeneous block phantom comprised of tissue, bone and lung-equivalent materials.

Results: The characterized beam qualities and spatial photon distributions are comparable to reported values in the literature. Agreement between computation and measurement is $\leq 2\%$ in the homogeneous block phantom and $\leq 2.5\%$ in the heterogeneous block phantom. Profiles taken at depths of 2 and 6 cm in the homogeneous block phantom show an agreement within 4%. All profiles in water, in bone, and lung-equivalent materials for beams using a HBT, have an agreement within 5%. Measured profiles of FBT beams in bone and lung-equivalent materials were higher than their computed counterparts resulting in an agreement within 2.5%, 5% and 8% within solid water, bone, and lung respectively.

Conclusions: The proposed virtual point source model and characterization method provide accurate computation of absorbed dose in both the homogeneous and heterogeneous block phantoms, providing experimental validation for our kV dose computation software, kVDoseCalc. As the characterization relies on easily-measured parameters, it is relatively easy to implement in any clinical medical physics facility, and the constructed virtual source model can be used as input for dose calculation systems. The source model is also flexible and can be adapted for a variety of kV x-ray dose sources.

3.2.2 Introduction

Modern radiotherapy techniques localize the treatment volume to reduce patient setup uncertainty and allow for smaller treatment margins. Kilovoltage (kV) image-guided radiotherapy (IGRT) such as cone-beam computed tomography (CBCT), fluoroscopy, and radiography are common techniques used to achieve this[21]. Moreover, IGRT techniques are also useful in identifying changes in patient anatomy such as tumor shrinkage requiring treatment re-planning[163]. Unlike therapeutic megavoltage (MV) dose, patient-specific kV imaging dose is not routinely computed nor accounted for. Others have measured the

dose deposited by CBCT to be between 3-8 cGy per imaging exam[84, 99]. If added to the therapeutic dose, the accumulated imaging dose from daily IGRT techniques could become significant[70], possibly pushing dose to organs at risk beyond acceptable dose limits and causing deterministic effects or lead to secondary cancers[20, 105]. According to the AAPM's Task Group 75, patient dose arising from imaging procedures should be used with great scrutiny by carefully considering the potential risk from deterministic and stochastic effects of the dose to individual patients[126]. To make these decisions, the first step is an assessment of the spatial distribution of the imaging dose. For this reason, the development of a tool capable of computing patient-specific dose arising from kV imaging procedures would be useful for monitoring purposes.

It is possible to adapt a commercial treatment planning system to compute kV dose by generating kV-energy dose deposition kernels[7]. This method is relatively easy to implement in a clinical setting. However, since energy kernels used in superposition-convolution algorithms handle heterogeneities by scaling the electron density without taking atomic number (Z) differences into account, there is room for improving the accuracy in high-Z tissues such as bone. Monte Carlo algorithms like the one used by Ding *et al.*[46] are very accurate and useful for research purposes, but typically rely on modeling the imaging systems based on nominal values that discount variations between individual machines of the same model. Furthermore, they are computationally intense and difficult to implement without technical knowledge of Monte Carlo algorithms, which makes them less clinically feasible.

Kouznetsov and Tambasco have developed in-house software (kVDoseCalc) capable of rapidly and accurately computing the absorbed radiation dose to a series of points of interest (POIs)[103]. The computation is performed using a hybrid algorithm that comprises deterministic and stochastic components. kVDoseCalc was computationally validated against industry standard Monte Carlo N-Particle Transport Code (MCNP)[187] and EGSnrc[95] using an idealized cone beam projection of a point source[103]. It was also experimen-

tally validated in homogeneous and heterogeneous block phantoms for small beams with no added filtration[138]. However, this validation was performed with a single spectrum per field and using third-party photon fluence distribution obtained by a sophisticated Monte Carlo simulation[46].

The purpose of this study is to introduce and validate a new method for characterizing the x-ray beam and creating a corresponding virtual source model for a kV x-ray source that is machine-specific and based on variables that can easily be measured in the clinic. The model can be used to characterize a Varian® On-Board Imager (OBI®) (Varian Medical Systems, Inc, Palo Alto, California, USA) source using only ionization chamber measurements without need for Monte Carlo models or specialized equipment. The spectrum of a Varian® OBI® only varies appreciably along the transverse axis[46]. Therefore, we have only measured spectral changes along this direction. This approach is similar to the one taken by Spezi *et al.* in their description of an Elekta CBCT unit,[156] however we derive the beam spectra and spatial fluence distribution by experimental methods whereas those used by Spezi *et al.* were generated using Monte Carlo simulation of the x-ray machine.

The proposed x-ray source model was used to characterize a Varian® OBI® for various tube settings representing standard OBI® CBCT beam qualities. The spectrum was interpolated using the third-party freeware Spektr and measurements of the HVL across the transverse axis of the beam and the nominal tube accelerating potential (kVp)[153]; a method we validated in a previous study[138]. This approach was also used by Turner *et al.* to successfully characterize the spectrum of commercial CT scanners; however in their work the transverse-axis bowtie profile and spectrum are used to reconstruct an equivalent bowtie filter thickness which is used in their Monte Carlo x-ray photon source model[170]. To obtain the spatial fluence distribution, the spectra are integrated with the National Institute of Sciences and Technology (NIST) mass-energy attenuation coefficients with respect to energy to derive the incident spatial fluence distributions[17]. We performed experimental

validation of the proposed virtual point source model and its characterization using relative dosimetry in a homogeneous and a heterogeneous block phantom.

We show that our approach to modeling the kV x-ray source yields accurate dose computation. While our ultimate goal is to develop a tool that rapidly and accurately computes patient-specific x-ray dose from CBCT IGRT procedures, the source construction and modeling formalism proposed in this study could easily be applied to any machine with a kV x-ray source. Furthermore, the main appeal of the method is that it requires only ionization chambers available at any clinical medical physics facility. Therefore, the future commissioning and clinical implementation of kV x-ray dose computation systems could be greatly facilitated by following the approach presented in this study.

3.2.3   Materials and Methods

Source Modeling

X-ray source model

The model relies on the following assumptions: (1) All photons originate from a single point located at the same source position as the real physical source; (2) the spatial, angular and energy distribution of the photons is derived from in-air relative dose and HVL measurements at the isocenter plane; and (3) the 2-D photon fluence at the isocentre plane can be described as the product of the central axis photon distribution in the transverse x- and radial y-directions, which are independent of each other. This virtual source model and characterization geometry is depicted in Fig. 3.1.

The source of x-ray photons is expressed as $S(\vec{r}, \hat{\Omega}, E)$ where $\vec{r}$, $\hat{\Omega}$, and E, indicate their initial location, orientation, and energy, respectively. The orientation $\hat{\Omega}$ of a photon originating at point $\vec{r}$ and traveling through an arbitrary point $\vec{r}'$ is defined by $\hat{\Omega} = (\vec{r} - \vec{r}') / \|\vec{r} - \vec{r}'\|$. The virtual point source can be described by the following equation
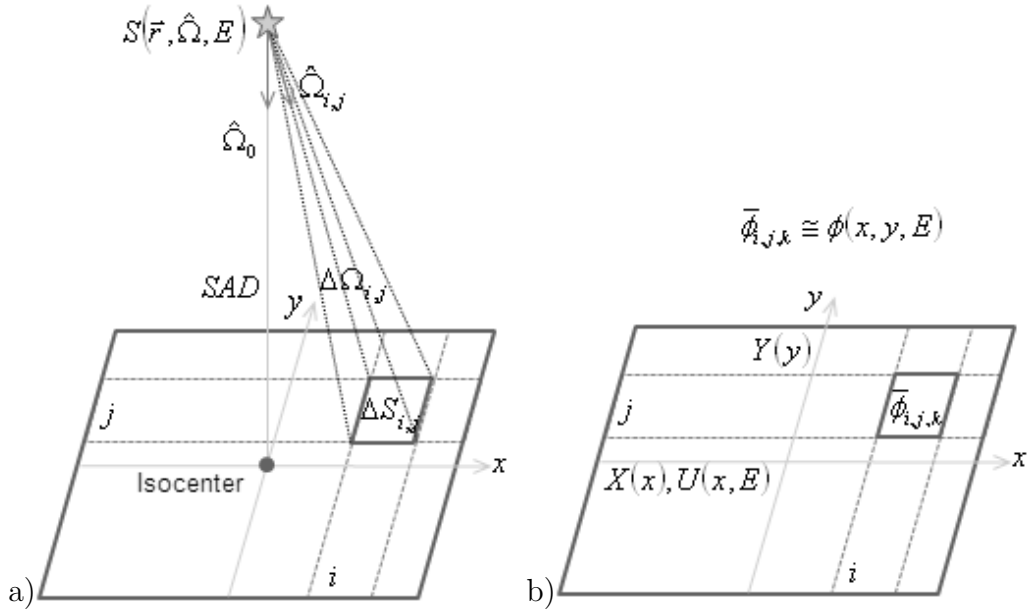
Figure 3.1: Depiction of the simplified source model (a) and the planar fluence characterization (b).

$$S(\vec{r}, \hat{\Omega}, E) = S_0 \cdot \delta(\vec{r} - \vec{r}_0) \cdot \frac{dP(\hat{\Omega}, E)}{d\Omega dE}, \qquad (3.1)$$

where $\delta(\vec{r} - \vec{r}_0)$ is a Dirac delta function indicating that photons all originate from the point $\vec{r}_0$, S_0 is the source rate (photons/s), and $dP(\hat{\Omega}, E)/d\Omega \cdot dE$ is a normalized differential probability distribution function representing the probability density of a photon of energy E being emitted in the direction $\hat{\Omega}$ from the source. The discretized version of $dP(\hat{\Omega}, E)/d\Omega dE$ ($\overline{P}_{i,j,k}$) was constructed using the radiation fluence which was determined through in-air relative dose measurements in the isocentre plane.

That is, values of $\overline{P}_{i,j,k}$, representing the fraction of photons of energy E_k going through the solid angle element $\Delta\Omega_{i,j}$, are estimated by evaluating the fluence of the x-ray beam at the isocentre plane through the small elements $\Delta S_{i,j}$. The average fluence $\overline{\phi}_{i,j,k}$ (photons/cm^2) is the average fluence of photons of energy E_k going through $\Delta S_{i,j}$ in the direction $\hat{\Omega}_{i,j}$ corresponding to the path between the source $(\vec{r}_0)$ and the middle of the element $\Delta S_{i,j}$ (Fig. 3.1). The values of $\overline{\phi}_{i,j,k}$ are experimentally determined in the next section; therefore, we can

101

derive the discrete normalized probability distribution of photons $\overline{P}_{i,j,k}$ from the following equation

$$\overline{P}_{i,j,k} = \frac{\overline{\phi}_{i,j,k} \cdot (\hat{\Omega}_{i,j} \cdot \hat{\Omega}_0)}{\sum\limits_{i,j,k} (\overline{\phi}_{i,j,k} \cdot (\hat{\Omega}_{i,j} \cdot \hat{\Omega}_0))}. \tag{3.2}$$

Overview of the virtual source model characterization

The x-ray virtual source model described above uses only empirical quantities that are easily measurable with standard equipment available at clinical medical physics facilities. As we have seen, the normalized differential probability distribution comprising the virtual point source is constructed from the projection of the measured differential energy fluence through element (i, j) in the isocenter plane projected from a single point. The planar differential energy fluence is described as a separable function as follows:

$$\phi(x, y, E) = X(x)Y(y)U(x, E)\phi_0. \tag{3.3}$$

The function $U(x, E)$ represents the spectrum of the beam. For the Varian OBI source considered in this study, the spectrum is assumed to vary only along the transverse (x) direction of the beam, as that is the direction in which the heel effect and the additional filtration (i.e., bow-tie filters) influence the beam. The relative intensity photon distribution of the beam (described by $X(x)$ and $Y(y)$) is taken to vary independently in the transverse x- and radial y-direction of the beam.These functions are normalized such that $\int X(x)dx = 1$, $\int Y(y)dy = 1$, $\int U(x, E)dE = 1$, and the constant (ϕ_0) is a unitless scaling factor. This calibration term relates relative to absolute fluence; however, in this study we only use relative absorbed dose for the sake of simplicity. These functions are defined in greater detail in the following sections.

Characterizing the transverse-axis variation of the spectrum

For accurate dose computation, the spectrum of a beam needs to be modeled sufficiently

accurately. In previous work, we showed that the HVL and kVp of a beam can be used to characterize the spectrum of an open kV x-ray beam to compute dose within an accuracy of $\pm 2\%$[138]. The spectrum is generated using a third-party Matlab® freeware (Spektr) by varying inherent aluminum filtration to match the measured HVL and the kVp[153]. In a previous study, we used a single spectrum for the entire field[138]. For a Varian® OBI® cone-shaped x-ray beam, the photon distribution and the beam quality along the transverse direction are influenced by the heel effect and added filtration such as the half or full bow-tie filter. In contrast, there is relatively little variation in the beam quality and photon fluence along the radial y-direction[46]. Hence, the function $U(x, E)$ describing spatial variations in the spectrum only varies with transverse-axis position x and energy E. The nominal kVp technique setting and HVL measurements along the transverse direction are used to characterize the spatially-varying spectrum.

Characterizing the photon distribution

Once the spatially-varying spectrum has been characterized, it is possible to characterize the spatial photon intensity distribution and fully describe an x-ray source according to our proposed virtual point source model. In a previous study, we used a photon distribution determined from stochastic Monte Carlo simulation by Ding *et al.*[46] for the Varian® OBI®. However, the use of third-party data limits one to the description of sources corresponding to energies and field sizes reported in the literature. While a full description of the spatial photon distribution can be obtained by Monte Carlo simulation, such as the model developed by Spezi *et al.*, which separates the photon distribution into three sources,[156] such simulations require technical knowledge that makes the approach less practical for clinical medical physicists. We propose a spatial photon fluence and spectral characterization that depends only on the measured relative absorbed dose in air. Since the wall thickness of most ionization chambers are thick enough to achieve charged-particle equilibrium for photons in the kV energy range,[111] the absorbed dose in air is equal to collisional kerma[11] and thus

given by the following equation:

$$D^{air}(x, y) = \int_0^{E_{max}} \phi(x, y, E) \left(\frac{\bar{\mu}_{en}}{\rho}\right)_{air} EdE.$$ (3.4)

The spatially-varying one-dimensional projection of the fluence in the transverse x and the radial y directions can be derived from in-air dose measurements according to Eq. (3.4) which represents the in-air Kerma for a beam described with the differential energy fluence $\phi(x, y, E)$. By replacing $\phi(x, y, E)$ using the separable function described in Eq. (3.3), it is possible to isolate the spatial components of the fluence. To find $X(x)$, we measured dose in the air along the transverse axis of the beam $(y = 0)$ and we expressed the in-air dose profile relative to dose at the centre of the beam $(x, y) = (0, 0)$, as shown in the following expression:

$$\frac{D^{air}(x, 0)}{D^{air}(0, 0)} = \frac{\int_0^{E_{max}} \phi(x, 0, E) \left(\frac{\bar{\mu}_{en}}{\rho}\right)_{air} EdE}{\int_0^{E_{max}} \phi(0, 0, E) \left(\frac{\bar{\mu}_{en}}{\rho}\right)_{air} EdE} = \frac{\int_0^{E_{max}} X(x)Y(0)U(x, E) \left(\frac{\bar{\mu}_{en}}{\rho}\right)_{air} EdE}{\int_0^{E_{max}} X(0)Y(0)U(0, E) \left(\frac{\bar{\mu}_{en}}{\rho}\right)_{air} EdE}.$$ (3.5)

Since the integrals in Eq. (3.5) are only with respect to energy (E), the spatial photon distributions $X(x)$ and $Y(y)$ can be pulled outside the integrals, leaving only $U(x, E)$. This gives the follow equation which expresses the $X(x)$ fluence in terms of measurable values:

$$\frac{X(x)}{X(0)} = \frac{D^{air}(x, 0)}{D^{air}(0, 0)} \frac{\int_0^{E_{max}} U(0, E) \left(\frac{\bar{\mu}_{en}}{\rho}\right)_{air} EdE}{\int_0^{E_{max}} U(x, E) \left(\frac{\bar{\mu}_{en}}{\rho}\right)_{air} EdE}.$$ (3.6)

Similarly, the spatial photon distribution $Y(y)$ in the radial y-direction can be expressed by Eq. (3.7) below because the spectral function $U(x, E)$ is independent of y.

$$\frac{Y(y)}{Y(0)} = \frac{D^{air}(0, y)}{D^{air}(0, 0)}.$$ (3.7)

Discrete function representation

As it is not feasible to measure $X(x)$, $Y(y)$, and $U(x, E)$ at more than a few points without specialized scanning equipment, the discrete function $\bar{\phi}_{i,j,k}$ (Eq. 3.8) is obtained

104

Table 3.1: Characterized beam qualities.

Filter	Energy
Full bow-tie	100 kVp
	125 kVp
Half bow-tie	110 kVp
	125 kVp

by interpolating between measurement points. We performed this interpolation using the cubic spline interpolation function in Matlab®. We chose a resolution of, 2.5 mm for the x-direction, 5 mm for the y-direction, and 1 keV increments for energy. The interpolated discrete values of X_i, Y_j, and $U_{i,k}$ are used as input for characterizing the virtual point source in kVDoseCalc.

$$\overline{\phi}_{i,j,k} = X_i Y_j U_{i,k} \cong \phi(x, y, E)/\phi_0. \tag{3.8}$$

Experimental measurements

We characterized the Varian® OBI® source using four beam qualities (Table 3.1) which were chosen because they are the default settings for OBI® 1.4 CBCT imaging techniques. We measured dose deposited by the OBI unit using a 160 ms pulse length and a 160 mA tube current to maintain a high signal-to-noise ratio at depths greater than 11 cm while minimizing the risk of overheating the x-ray tube over the course of many measurements. All measurements were performed using a 0.65 cc PR-06C Capintec farmer-style chamber (Capintec Inc., Ramsey, NJ, USA) calibrated in the kV energy range, and a Standard Imaging Supermax electrometer (Standard Imaging, Middleton, WI, USA) set in the low-dose sensitivity range with a potential bias of +300 V applied.
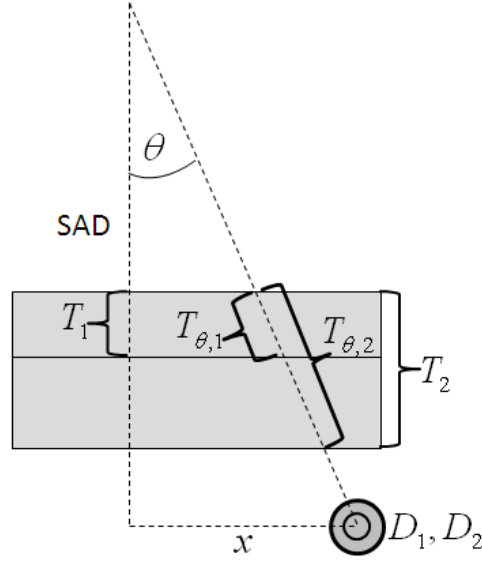
Figure 3.2: Measuring geometry for HVL at an off-axis distance x and a source-to-axis distance SAD showing the longer pathlength $T_{\theta,1}$ and $T_{\theta,2}$ taken by photons going through the thicknesses T_1 and T_2 of attenuating material.

Transverse-axis HVL measurements

The HVL was measured in the centre of the beam and at intervals of 2 cm along the transverse x-axis at a surface-to-axis distance (SAD) of 100 cm for each characterized beam quality (Fig. 3.2). For each point, absorbed dose in air (D_n) was measured three times under three different filtrations (T_n): no filtration $(T_0 = 0, D_0)$, enough aluminum to reduce absorbed dose in air by less than 50% (T_1, D_1), and enough aluminum to reduce absorbed dose in air by more than 50% (T_2, D_2). The aluminum thicknesses used for our measurements varied between 2.0 mm Al to 12.0 mm Al depending on the position and the bowtie filter used. To position the kV source perpendicular to the transverse axis, the linac gantry was rotated to 90 degrees. The couch top was moved laterally using the digital couch readings to position the source at the different locations along the transverse axis. The HVL was computed from these measurements using the two point non-linearity interpolation technique (Eq. 3.9)[61]:

$$\text{HVL} = \frac{T_{\theta,2} \cdot \ln\left(2 \cdot \frac{D_1}{D_0}\right) - T_{\theta,1} \cdot \ln\left(2 \cdot \frac{D_2}{D_0}\right)}{\ln\left(\frac{D_1}{D_2}\right)}. \tag{3.9}$$

We used the method described by Hill *et al.* to account for the longer photon path-length through the attenuating material when measuring the off-axis HVL[73]. The effective thickness is given by $T_{\theta,n} = T_n/\cos(\theta) = T_n \times \text{SAD}/\sqrt{(\text{SAD}^2 + x^2)}$ for a given SAD and off-axis position x. The uncertainties in calculated HVLs were obtained by propagating the uncertainty in attenuating thicknesses and in-air dose measurements following the method outlined by Hill *et al.*[73]

Phantom relative dose measurements

Relative dose measurements were taken inside a homogeneous and heterogeneous (Fig. 3.3) block phantoms placed at a source-to-surface distance (SSD) of 100 cm using the in-room patient-positioning lasers. The block phantoms were comprised of Gammex® solid water® (Gammex® 457), solid bone® (Gammex® 456), and solid lung® (Gammex® 455, Gammex Inc, Middleton WI, USA). The 0.65 cc Capintec ionization chamber was placed within a 2 cm thick slab of the relevant material via a cavity that was drilled to the specific volume and geometry of the chamber using the setup described in section 3.1. The depth of the measurement was varied by displacing the slab containing the ionization chamber to the depth of interest, while the off-axis position was varied by moving the couch top laterally and using the digital couch readings to find the desired positions. The AAPM's Task Group 61 (TG-61) describes the protocols to be followed when performing dosimetry for x-ray beams in the 40-300 kV energy range[111]. Following the TG-61 guidelines, the relative dose measurements were normalized at a depth of 2 cm[111]. As the ionization chamber was calibrated to read absorbed dose to water, a calibration factor had to be applied when measuring dose in lung or bone-equivalent materials. This conversion factor is the ratio of mass-energy absorption coefficients in a medium over that of water, averaged over a spectrum free in air ($[(\bar{\mu}_{en}/\rho)_w^{med}]_{air}$). The values of the mass-energy absorption coefficients were taken
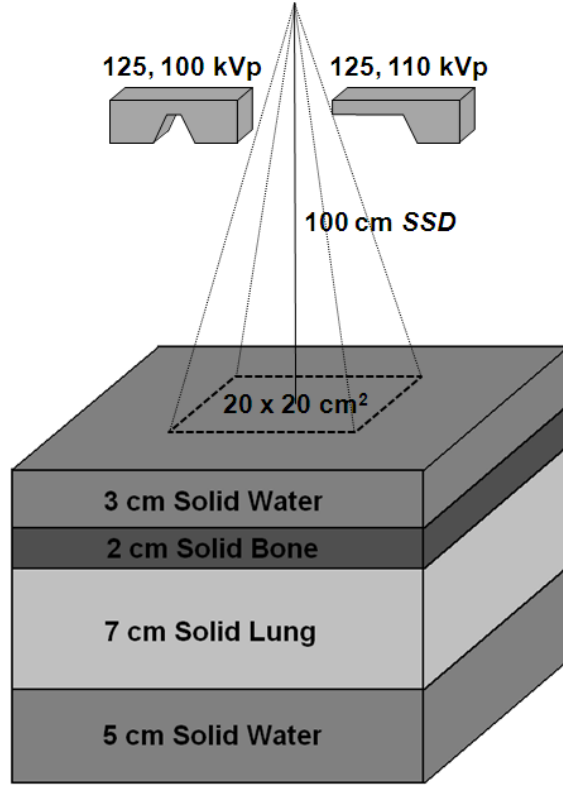
Figure 3.3: Experimental setup for the heterogeneous block phantom. The dimensions of the field, SSD, and the characterized beam qualities and associated bow-tie filters are depicted.

from Table 3.1 in Appendix B of TG-61. As there are no published values for Gammex solid water® tissue equivalent materials for tissue, lung, and cortical bone materials used in this study, we used the values for normal tissue, lung, and bone; respectively. We chose the mass-energy absorption coefficients for the beam qualities that most closely matched our four characterized beams in central-axis HVL and kVp.

Measurements with ionization chambers are subject to systematic and random uncertainties. The positional lasers used to position the centre of the phantom are calibrated monthly to a tolerance of 1 mm; this means that transverse axis-profile have a maximum systematic positioning uncertainty of 1 mm. The transverse position of the couch was set using the digital couch readings, which have a resolution of 1 mm. The measurement of central axis depth-dose profiles would not be affected because the beam is relatively flat

within ±1 cm of the central axis. While the top of the phantom is positioned using the same lasers, an uncertainty of 1 mm over an SSD of 100 cm would only lead to an uncertainty of 0.2% due to the inverse square-law. The positions in transverse-axis profiles are measured by using the digital couch readings which have a resolution of 1 mm, leading to a random ±1 mm uncertainty. Furthermore, there are statistical uncertainties arising from ionization chamber measurements themselves, which have been estimated at 2.1% in MV beams[160] while TG-61 estimates the uncertainty for relative and absolute dosimetry in kV beams to be 3.0% and 4.7%, respectively[111].

Measurements in this heterogeneous geometry are subject to many uncertainties due to the high attenuation of kV beams by high-Z materials. In the solid bone region, where the local dose gradient is $\pm6\%$/mm, the position of the ionization chamber can only be pinpointed in a CT scan and defined in kVDoseCalc to within half of the height of a CT voxel (0.81 mm for our CT images of the phantoms). Therefore, there is a 5% relative dose uncertainty due to the uncertainty of the ionization chamber position alone.

Unlike the solid bone slab, the measurements taken in the solid lung slab are not located in a high-gradient region. However, the measurements are very sensitive to the thickness of solid bone, which can only be modeled to the nearest half-pixel, leading to another 2.5% uncertainty. Furthermore, while we modeled it with a constant density, the solid lung material is very porous with numerous air pockets. According to the manufacturer, the nominal CT density is -690 ±80 HU, which we confirmed with our CT scan average of -720 HU with a standard deviation of ±35 HU. Likewise, the nominal physical density is 0.300 g/cm^3 while it was measured at 0.271 g/cm^3. In comparison, variations in HU inside the solid water slab were only ±10 HU. If we assume that reconstruction uncertainties account for 10 out of 35 HU, we can estimate a variation of local density of 9% throughout the volume.

Added in quadrature, we estimate the total experimental positional uncertainties in transverse profiles to be ±2.5 mm. Total experimental dosimetric uncertainties in relative depth-

dose profiles were ±2.1 %, ±5.5 %, and ±10 % in the solid water, bone and lung slabs, respectively.

Dose computation

An in-house software, kVDoseCalc, was used to compute the absorbed x-ray dose[103]. The software separates the absorbed dose at a POI into two components: the primary dose which is calculated deterministically and the scattered component which is calculated stochastically. The scattered dose is further separated into a first-collision contribution and a multi-collision contribution. These two stochastic components of the x-ray dose are computed using biased Monte Carlo techniques to model the relevant photon interactions: photoelectric effect, and coherent and incoherent Compton scattering[103].

kVDoseCalc uses the spatial and Hounsfield Unit (HU) information from a DICOM-format CT image to compute the dose. However, to dissociate errors due to the imaging process (e.g., reconstruction errors and statistical noise) from errors due to our virtual source model and its characterization, we computed dose in an idealized CT image of the homogeneous and heterogeneous (Fig. 3.3) block phantoms. We constructed the idealized images of the block phantoms using MATLAB® by assigning the corresponding nominal HU values to the voxels representing air, water, lung, or bone. The dimensions of both idealized images were $512 \times 512 \times 91$ voxels ($\sim$23.8 million total), each of size $0.81 \times 0.81 \times 3$ mm^3.

kVDoseCalc allows the user to define HU ranges associated with physical density ranges attributed to different material compositions (expressed in atoms/cm^3). The elemental compositions of the Gammex ® solid water®, lung® and bone® were provided by the manufacturer of these materials. The interaction micro cross-sections for all relevant energies (e.g., 1-150 keV in 1 keV energy bins) are calculated using the ENDF/B-VI micro cross-section library[129].

For all computed doses, the virtual point source was positioned along the central axis of the block phantoms at a distance of 100 cm from their surface. The computations were performed using four Intel® Core™ i7 960 CPU at 3.20 GHz for each POI using 1.5 millions seeded photons.

3.2.4 Results

kV source model

Figure 3.4 demonstrates the variation of the measured and interpolated HVL as a function of the transverse axis displacement for each evaluated beam modality. For a beam with no added filtration, one would expect a relatively constant HVL with slight beam hardening in the direction of the anode due to the heel effect. The addition of a bow-tie filter introduces significant filtration and beam hardening. We therefore expect HVL to rise sharply from the central-axis value where the bow-tie filter is thickest, as shown in Fig. 3.4. Near the edges of the beam, we measured the HVL at a distance of 5 mm from the edge of the beam to avoid artifacts due to volume averaging effects of the ionization chamber in the high gradient penumbra region of the beam. We use the measurements to extrapolate the HVL in the outer 5 mm near the edge of the field. While this may introduce an error in the characterization of the beam, the dose quickly drops off in this penumbra region due to reduced lateral scatter in the phantom as well as the reduced amount of photons from the source.

Figure 3.5 shows good agreement between our experimentally derived photon fluences for the 125 kVp beams and the corresponding fluences Ding *et al.*[46] reported using Monte Carlo modeling of a Varian® OBI® x-ray source. In the case of the transverse axis (Fig. 3.5a), the only noticeable difference is that the HBT fluence determined by Monte Carlo exhibits a small central-axis bump that we did not measure. Our radial axis fluences (Fig. 3.5b) agree with the Monte Carlo generated fluences within the Monte Carlo statistical noise for both bow-tie filters. Furthermore, the radial axis fluence determined experimentally does
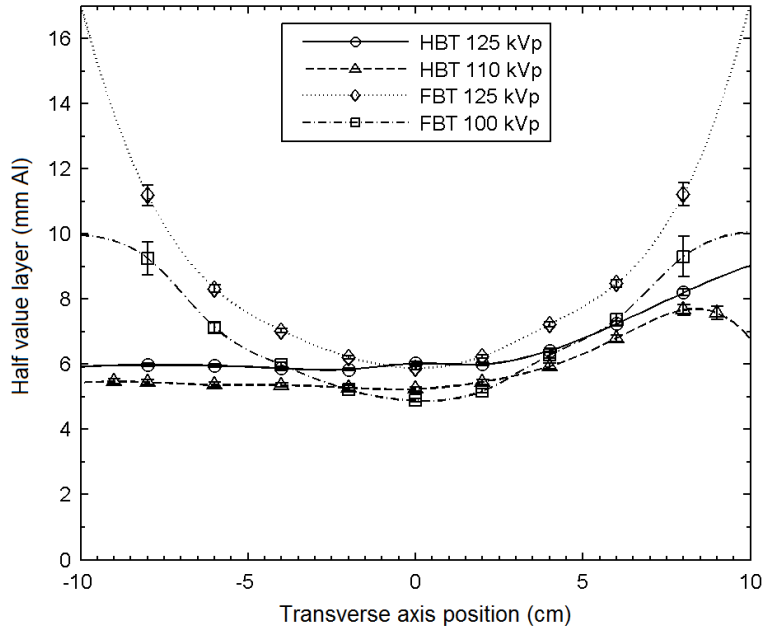
Figure 3.4: Measured (dots) and interpolated (lines) HVL for each beam quality investigated. This HVL data was used to obtain the spectra in the kV virtual source model.

not vary appreciably between different modalities. For all four characterized beam qualities normalized at the centre of the beam, we determined the greatest fluence difference to be only 0.2% between a 125 kVp and a 100 kVp beam at the farthest distance (10 cm) from the centre of the beam. Since the Varian OBI 1.4 default CBCT settings have a maximum field size of 10.3 cm (symmetrically) in this axis, a single characterization of the radial axis photon distribution Y(y) could be used for all four beam modalities in our beam model without loss of computational accuracy. Larger fields or kV imaging units from other manufacturers such as the Elekta XVI may require individual characterization of different beam qualities.

Homogeneous phantom measurements

For all the beam qualities, the agreement between computed and relative dose inside the homogeneous phantom is within 2% of the reference dose (Fig. 3.6).

a)

b)
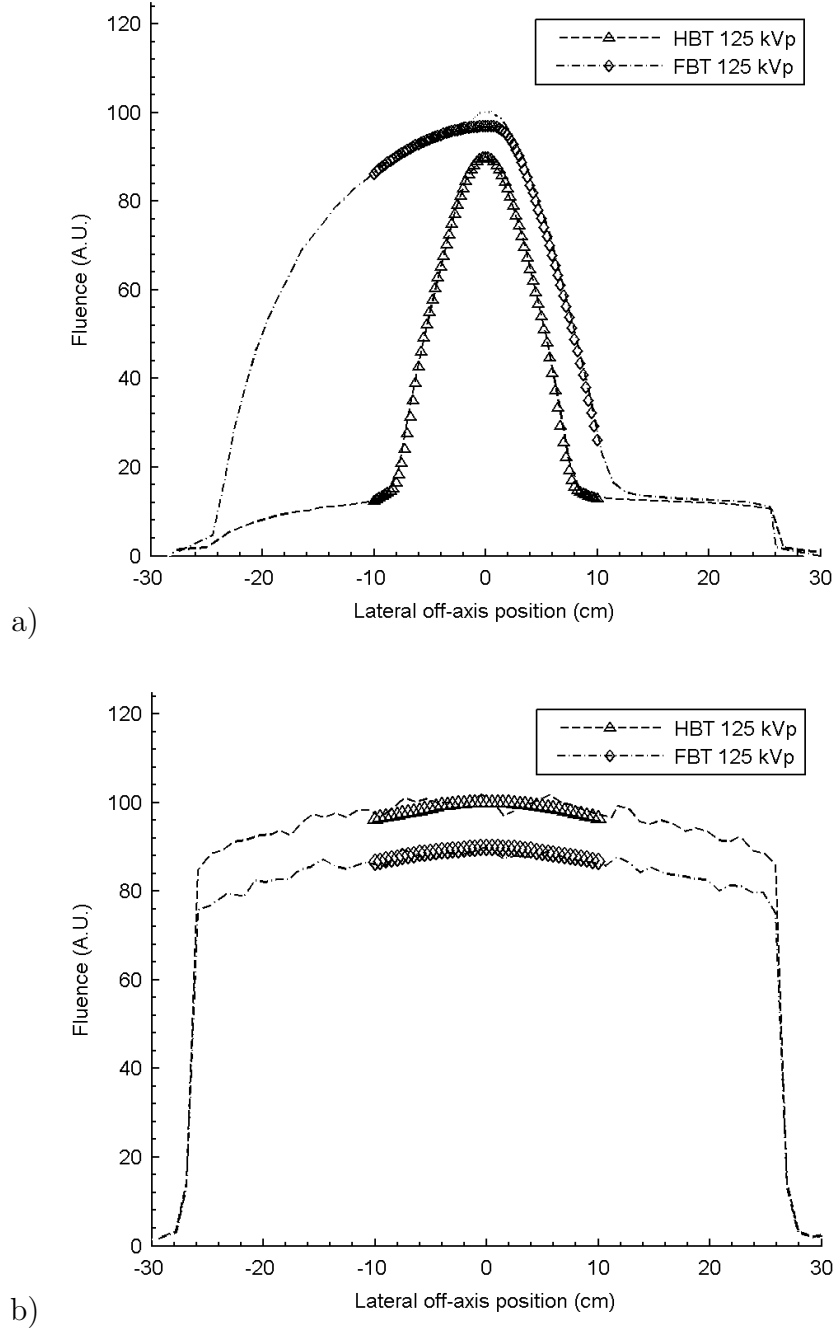
Figure 3.5: Comparison between fluence determined by Monte Carlo (line) by Ding *et al.*[46] and the fluence interpolated from our experimental measurement (symbols) along the transverse axis (a) and the radial axis (b).

Figure 3.6: Comparison between central-axis relative depth dose measurements (dots) and computed dose (lines) for all four beam qualities inside the homogeneous block phantom. All profiles were normalized to 2 cm depth for the 125 kVp HBT beam to distinguish them from one another.

Homogeneous phantom transverse-axis dose profile measurements agree with computation within 2% and 4% of the central dose in the low and high-gradient parts of the beam, respectively (Fig. 3.7).

The virtual point source model assumes that every photon originates from the a single point; in reality, the focal spot is not a point but has a finite size. Moreover, the photons do not originate solely from the focal spot of the x-ray tube, but also from interactions in the components of the tube head, which include collimators and possible filters (e.g., bow-tie filters). Spezi *et al.* report that photons from these additional sources can cause up to 10% of the absorbed dose in water, especially closer to the surface[156]. We therefore expect that our measurements would be higher than computation near the surface and lower than computation at depth, which is what is observed in Fig. 3.6.

Heterogeneous phantom measurement

The heterogeneous phantom central-axis depth-dose measurements agree with calculations within 2.5% of reference dose for all beam qualities (Fig. 3.8). As previously noted in section 3.2, the systematic uncertainty in the radiological depth traversed by the beam adds up to $\geq 10\%$ of local dose due to the uncertainty in the thickness of high-density solid bone and the uncertainty in density through the porous solid lung. Hence, the agreement between measurement and computation is within experimental uncertainty for all points.

Transverse-axis profiles for HBT beams show agreement within 5%, with the worst points being located in the high-gradient region (Fig. 3.9). FBT beams show agreement within 2.5%, 5%, and 8% for solid water, bone, and lung, respectively (Fig. 3.10). Measured FBT profiles in solid bone and lung are systematically greater than computed profiles, with distance to agreement ≤ 5 mm in bone and ≤ 7 mm in lung. The discrepancy is too high to be attributable to experimental error and is probably due to the simplified modeling of the beam. As previously mentioned, up to 10% of photons may originate from scattering from

Figure 3.7: Comparison between transverse-axis relative dose profile measurements (symbols) and computation dose (lines) with HBT (a) and FBT (b) inside the homogeneous block phantom. All profiles were normalized to the centre of the 125 kVP beam at a depth of 2 cm beam to distinguish them from one another.
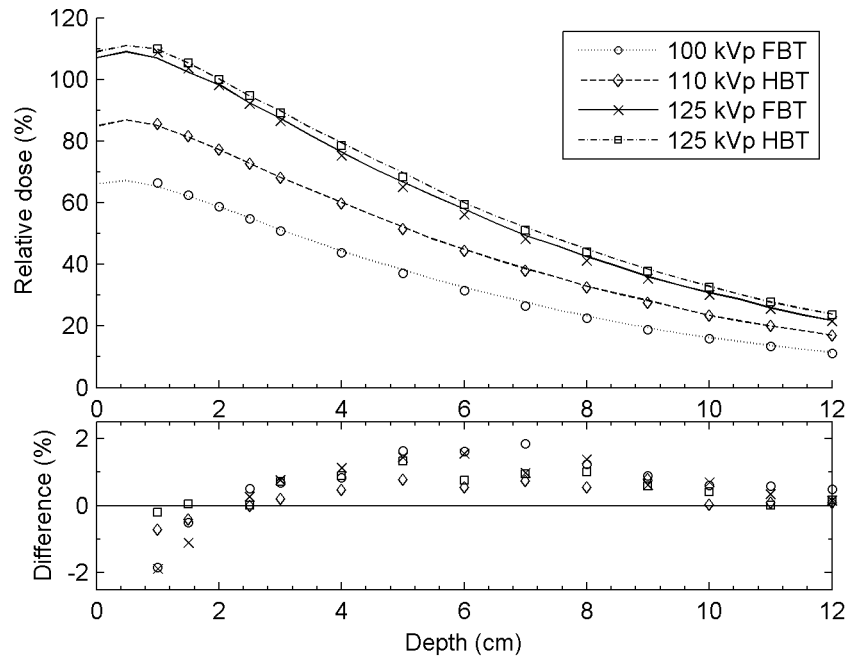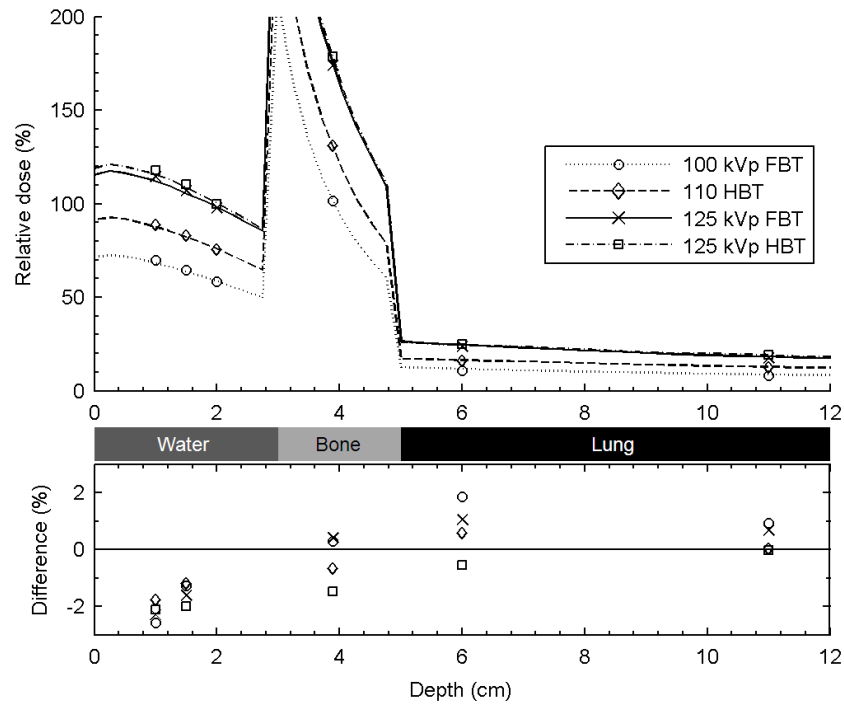
Figure 3.8: Comparison between central-axis relative depth dose measurements (symbols) and computation (lines) for all four modalities inside the heterogeneous block phantom. All profiles were normalized to 2 cm depth for the 125 kVp HBT beam to distinguish them from one another.
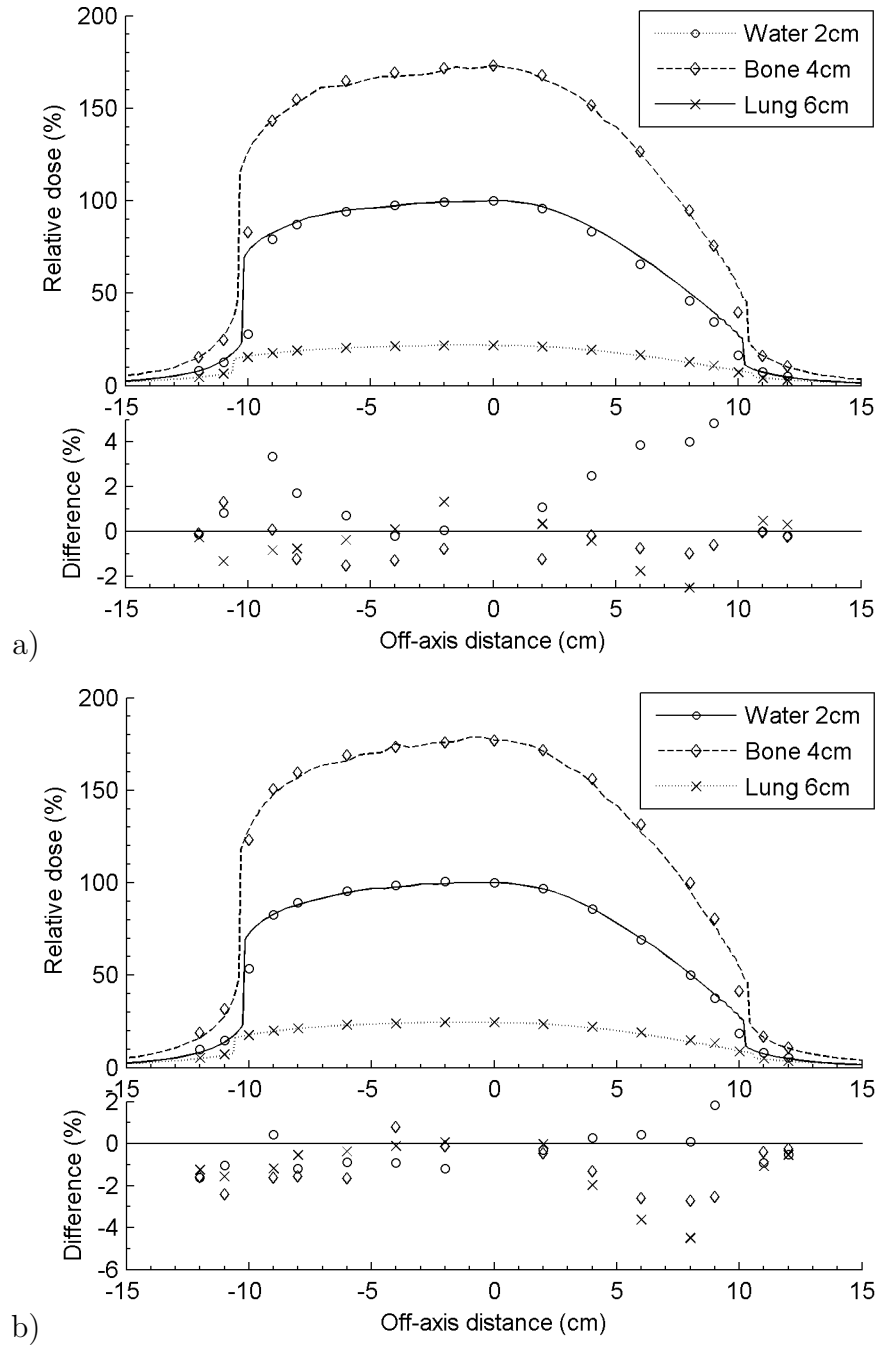
Figure 3.9: Comparison between transverse-axis relative dose profile measurements (symbols) and computation dose (lines) with HBT at 110 kVp (a) and 125 kVp (b) inside the heterogeneous block phantom. All profiles were normalized to the centre of the 125 kVp beam at a depth of 2 cm to distinguish them from one another.
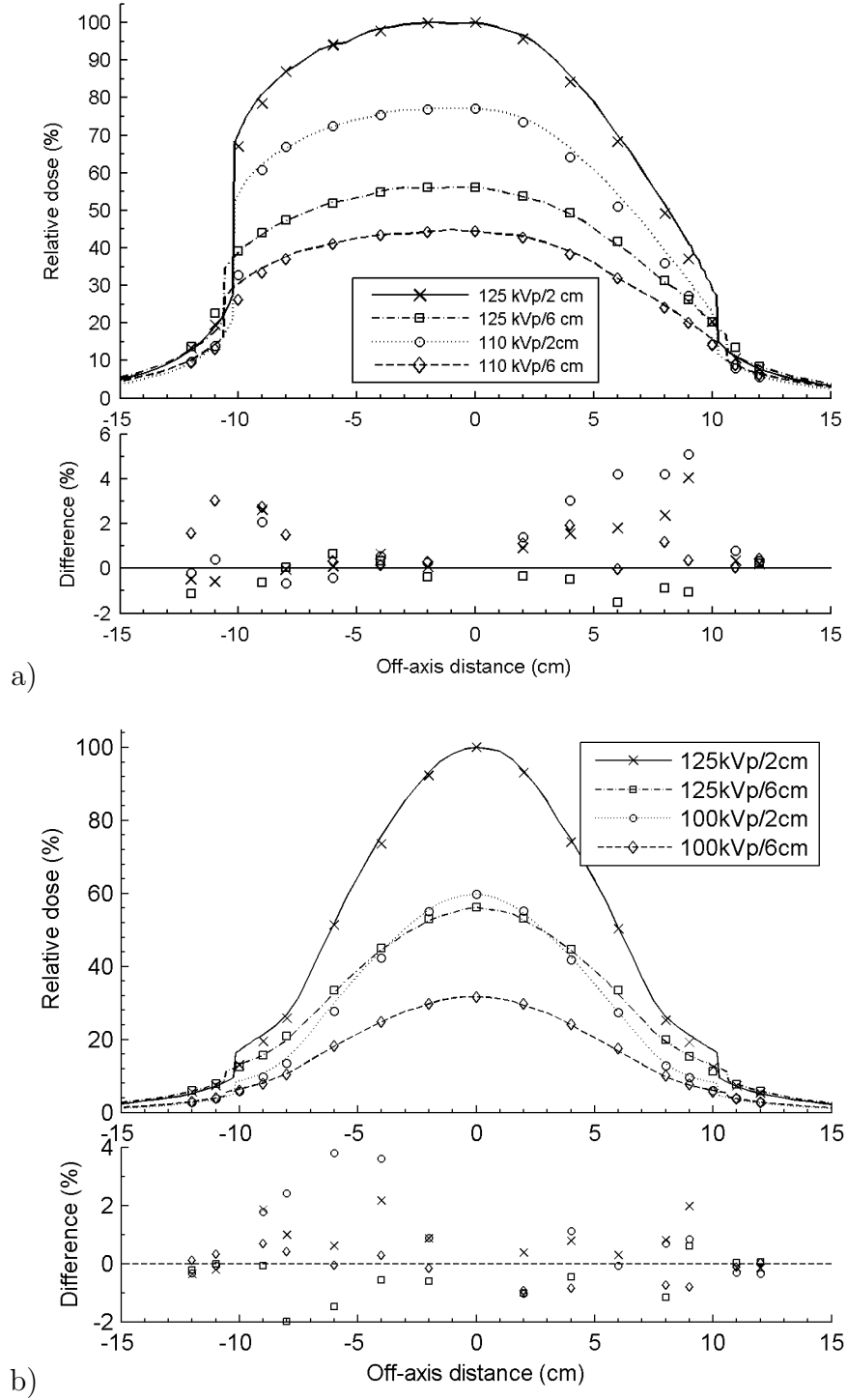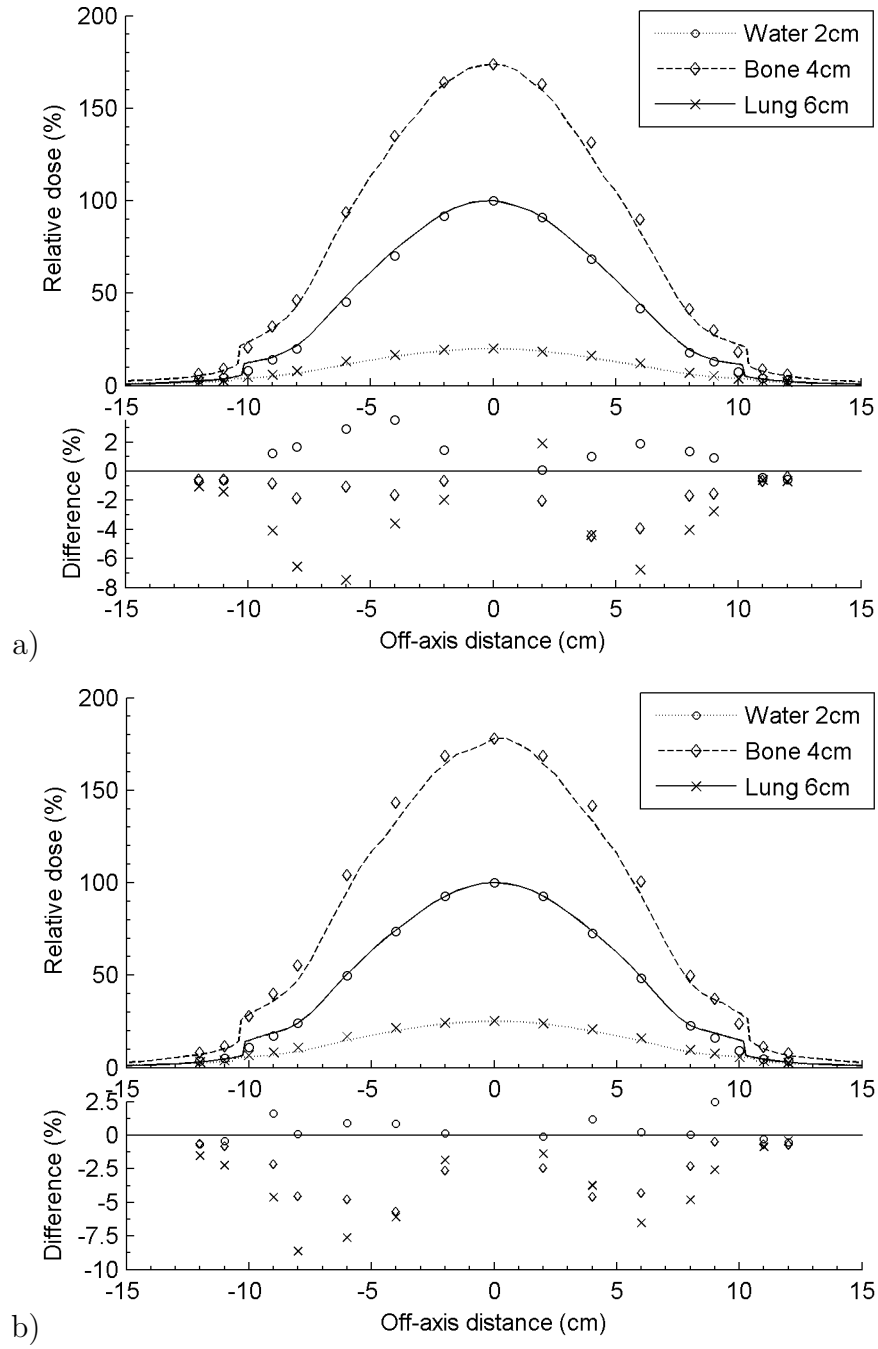
Figure 3.10: Comparison between transverse-axis relative dose profile measurements (symbols) and computation dose (lines) with FBT at 100 kVp (a) and 125 kVp (b) inside the heterogeneous block phantom. All profiles were normalized to the central axis of the 125 kVp beam at a depth of 2 cm to distinguish them from one another.

within the bow-tie filter,[156] and the focal spot has a small ($\sim$0.8 mm) finite size which we model as a point source. These extra-focal photons have slightly different scattering directions than our virtual point source predicts, and therefore would contribute to the discrepancies seen in the high-complexity heterogeneous geometry.

3.2.5 Discussion and Conclusion

The purpose of this study was to introduce and validate the formalism of a simplified virtual source model and characterization method for kV x-ray dose computation, that could be easily implemented in a clinical medical physics setting. Although we have used in-house software (kVDoseCalc) to validate our kV source modeling approach, the approach can be incorporated into other x-ray dose calculation systems. To use the software to compute doses delivered by clinical kV x-ray sources, it was necessary to develop a method to model and characterize the spectral and spatial photon distribution of the source. While validation of the simplified spectrum characterization method was conducted for unfiltered beams,[138] this study represents a full characterization of the kV x-ray source for use in kV x-ray dose computation.

To validate our simplified virtual point source model and characterization method, we have applied it to a Varian® OBI® 1.4 imaging unit. The agreement with experiment that we have achieved in this study is comparable or better than that achieved by adapting MV commercial treatment planning software to compute kV dose; particularly in the area outside the path of the beam where dose is deposited solely by scattered photons[7]. One can obtain slightly better agreement using standard Monte Carlo modeling[45] or a multi-focal source such as proposed by Spezi *et al.* ($\leq$ 2%),[156] but the former requires specialized knowledge of Monte Carlo modeling while the latter is not defined entirely by experimental measurements.

While validation in homogeneous geometries is essential, high-Z heterogeneities pose the greatest challenges in kV x-ray dose computation in anthropomorphic geometries. For this reason, the validation in the heterogeneous phantom, comprising 2 cm of highly attenuating bone-equivalent material and low-density lung-equivalent material, is of particular interest. Our computed percent depth-dose curves and transverse-axis profiles generally agreed with measurements within experimental uncertainty. To the best of the author's knowledge, such accuracy is not currently possible with megavoltage therapy treatment planning systems adapted for kV dose computations[5]. There are proposed algorithms which take into account the high-Z contribution of bone such as the one proposed by Ding *et al.*[133, 50]; unfortunately, these correction-based methods currently have to be applied externally in post-processing analysis, which reduces their clinical feasibility.

3.3   General Conclusions

This chapter introduces and validates the formalism used to describe a kV beam in kVDoseCalc for the rest of this work. Despite the high variations in fluence and spectrum accross beams comprising a bowtie filter compared to open beams, we were able to compute the transverse axis dose profiles with greater accuracy than achieved for open beams in the previous chapter. This shows that our beam-specific experimental fluence and spectral characterization method and virtual point source are superior to using that obtained from third-party Monte Carlo simulation.

The only beams for which the agreement between measurements and computation was worst ($\sim$5-8%) was for beams comprising a FBT in heterogeneous geometries, presumably due to the $\sim$10% of extra-focal photons which we neglect in our virtual point source[156]. It is likely that the accuracy could be improved by implementing a multi-focal virtual point source such as the one proposed by Speci *et al.*[156]; however, to characterize a multi-focal source would require more complexity than that offered by our method which relies solely on empirical measurements. Therefore, it would run afoul of this project's philosophical goal of a clinically feasible kV dose computation method.

As we show in the next chapter, whatever are the inaccuracies that we introduce by our characterization of FBT beams, they do not translate in significant disagreement in the computation of dose deposited by kV CBCT imaging procedures since we obtain good agreement even in a highly heterogeneous patient-simulating anthropomorphic phantom.

Chapter 4

Experimental validation of the source model for CBCT imaging

4.1 General Introduction

In this chapter, we use the source model developed in chapters 2 and 3 to experimentally validate our kV dose computation method applied to four default CBCT imaging protocols. We compare measurements to dose computations in two geometries: a homogeneous cylindrical phantom and the RANDO® anthropomorphic phantom. The anthropomorphic phantom is comprised of tissue and lung-equivalent materials, as well as real bones. It represents the closest approximation to measuring the dose inside a real patient for the purposes of experimental validation of our approach.

The remainder of this chapter is in manuscript form for submission to the peer reviewed journal, *Medical Physics*. I was the first author of this manuscript, and Dr. Alexei Kouznetsov and Dr. Mauro Tambasco were contributing authors. I designed the homogeneous cylindrical phantom and characterized the TLDs for use at kV energies. I also designed and performed all the experiments. Dr. Alexei Kouznetsov adapted the source code of kV-DoseCalc to allow rotating sources according to my specifications. He also produced a new, more efficient GUI in which the user provides the starting angle and arc size. Dr. Mauro Tambasco provided the original research idea behind the work done in this manuscript and suggested the use of a cylindrical homogeneous phantom. I wrote the first draft of the manuscript, and the contributing authors have helped with review and revisions.

4.2 Experimental validation of an in-house method for computing patient-specific kV-CBCT imaging dose

Y Poirier[1], A Kouznetsov[1], and M Tambasco[2]

[1] Department of Physics and Astronomy, University of Calgary, Calgary, Alberta T2N 4N2, Canada

[2] Department of Physics and Astronomy and Department of Oncology, University of Calgary, Calgary, Alberta T2N 1N4, Canada and Department of Physics, San Diego State University, San Diego, California 92182-1233, USA

4.2.1 Abstract

Purpose: To provide experimental validation of a previously developed kilovoltage (kV) x-ray source characterization/model and dose computation method for estimating the patient-specific absorbed dose from kV cone-beam computed tomography (CBCT) imaging procedures.

Method and materials: We simulated the default Varian® on-board-imager (OBI®) 1.4 CBCT imaging protocols using our previously developed and simple to implement x-ray point-source model and source characterization approach for use in our in-house kV dose computation software (kVDoseCalc). We compare the absorbed dose computations to doses derived from ionization chamber measurements acquired at several points in a homogeneous cylindrical phantom and from thermoluminescent detectors (TLDs) placed in an anthropomorphic phantom.

Results: Inside the homogeneous cylindrical phantom, the computed doses agreed with measurements within $\leq 2\%$ of local dose, except in regions of high dose gradient where the distance to agreement is 2 mm. The computed absorbed dose inside the anthropomorphic

phantom generally agreed with TLD measurements, with an average percent dose difference ranging from $2.4 \pm 6.0\%$ to $5.7 \pm 10.3\%$, depending on the characterized CBCT imaging protocol. The low-dose thorax and the standard-dose head scans showed the best and worst agreement, respectively.

Conclusions: Our previously developed method for characterizing and modeling a kV x-ray source and computing kV x-ray dose is capable of assessing patient-specific absorbed dose from kV CBCT procedures within reasonable accuracy.

4.2.2   Introduction

Cone-beam computed tomography (CBCT) is a common volumetric imaging technique used in image-guided radiation therapy (IGRT) to localize tumors and organs-at-risk and to verify the patient position. While the patient-specific absorbed dose deposited by megavoltage (MV) therapeutic and imaging beams can be routinely calculated using commercially-available treatment planning software (TPS), no equivalent commercial software currently exists for kV x-rays. The American Association of Physicists in Medicine (AAPM)'s Task Group 75 report raised concerns regarding the imaging dose accrued by patients during IGRT[126]. There is interest in developing a fast and accurate method to compute the patient-specific absorbed dose from kV imaging procedures and to possibly incorporate it in the radiation treatment plan.

Recent attempts to develop such a method include adapting the Pinnacle TPS (Philips Medical Systems, Milpitas, CA USA) for kV dose computation[7] and conventional Monte Carlo (MC) simulations to estimate the kV CBCT dose in a prostate patient[44]. The former approach is relatively easy to implement in the clinic since it uses existing comercially available software and equipment. Unfortunately, the method of scaling energy-deposition kernels with electron density underestimates the photoelectric effect and attenuation in bone by a factor of three to four[50]. In contrast, MC simulation techniques are very accurate,

but are computationally intense and require specialized software implementation that make them less feasible for routine clinical use.

Kouznetsov and Tambasco have developed an in-house software (kVDoseCalc) that allows one to use CT image data to rapidly and accurately compute the absorbed kV x-ray dose at a series of points of interest (POIs)[103]. This method was validated computationally using the MCNP[187] and EGSnrc[95] MC simulation techniques[103]. It was also validated experimentally for radiographic imaging procedures using open beams[138] and beams produced with added bowtie filters[137]. A machine-specific virtual point source model was developed by Poirier *et al.*[138, 137]. This source model is characterized from simple in-air ionization chamber measurements without the need for specialized equipment or knowledge of MC modeling techniques.

However, in previous studies our dose computation method was only validated for the stationary beams used in radiographic imaging. The purpose of this study is to provide experimental validation of the method for a rotating source. The validation was performed using a Varian® On-Board Imager (OBI®) 1.4 imaging unit (Varian Medical Systems, Inc, Palo Alto, CA USA) in homogeneous and anthropomorphic phantoms.

4.2.3 Materials and methods

Model and calculation overview

Software algorithm overview

We computed the absorbed kV x-ray dose using kVDoseCalc, a kV dose computation software developed in-house by Kouznetsov and Tambasco[103]. The software computes the dose by numerically evaluating the linear Boltzmann transport equation (LBTE) to find the differential photon angular flux density at a POI, and converts this to absorbed radiation dose using collisional-kerma factors based on the on coherent and incoherent angular distribution functions and photoelectric absorption interaction cross sections.

126

The differential angular flux density is separated into its primary and scattered components. The primary component of the differential angular flux density is calculated deterministically using exponential attenuation and the beam divergence as described by the inverse-square law $(1/r^2)$. The scattered component is further separated into a first- and a multiple-collision contribution, which are calculated using biased MC methods to generate a population of representative distribution of scattering points. The scatter component of the differential angular flux density at the POI is calculated by using these scattering points as a secondary radiation source in the numerical evaluation of the LBTE[103]. To evaluate the interaction cross-sections throughout the medium, the software requires a DICOM-format CT image in which Hounsfield units (HU) ranges are assigned a physical density (g/cm^3) and an elemental material composition $(atoms/cm^3)$. The interaction cross-sections from the ENDF/B-VI micro cross-section library[129] are used to calculate total interaction cross sections of each material. These interaction cross sections are used to compute the optical length of the photon trajectories required for the photon transport for the various components of the differential angular flux density. The dose is computed from the flux (the differential angular flux density integrated over all solid angles) through flux-to-kerma conversion factors which are also pre-calculated for each photon energy and material composition in the CT image by integrating the differential distribution of photon energy fluence with the mass energy-transfer coefficient of each possible energy and scattering angle.[103].

The virtual point source model is created from the user-specified spatially-varying spectrum and planar fluence at the isocentre plane. This virtual point source is used to create the photons which are transported in the biased MC calculations of the scattered component of the differential angular flux density. In this model, photons are generated with a given energy and trajectory from the source location (the focal spot on the x-ray tube anode) to the isocentre plane[137]. To model rotating CBCT sources, the software was modified to incorporate a starting gantry angle and arc size. Photons are assigned a random angle in

Table 4.1: Default settings for CBCT procedures using the Varian® OBI® 1.4 system.

Protocol	Standard-dose head	Pelvis spotlight	Low-dose thorax	Pelvis
Filter	Full bowtie		Half bowtie	
Field size (cm)	(x_1, x_2)=(13.6, 13.6)		(x_1, x_2)=(6.8, 23.5)	
	(y_1, y_2)=(9.2, 9.2)		(y_1, y_2)=(10.3, 10.3)	
Arc size	200°		360°	
Energy (kVp)	100	125	110	125
Exposure (mAs)	145	720	262	580

this angular range to assign random origins to each photon.

The dose computations were performed at each POI using 1.5 million seeded photons on four 3.20 GHz Intel® Core™ 7 960 CPU. The virtual point source was placed at a 100 cm surface-to-axis distance (SAD) from the isocentre for all computations so as to match the default CBCT imaging parameters of the Varian® OBI® 1.4 imaging system.

CBCT source characterization

The imaging source of a Varian® OBI® 1.4 imaging unit was characterized for four kV CBCT imaging protocols (Table 4.1) using our previously validated kV source characterization method and virtual point source model[137]. Briefly, this method involves measuring the HVL along the transverse axis and the in-air kerma profiles along the radial and transverse axis. These values were measured at 2 cm intervals for all four beam qualities using a 0.65 cc PR-06C Capintec farmer-style chamber (Capintec Inc., Ramsey, NJ, USA) calibrated in the kV energy range (60, 80, 100, 150 and 200 kVp) and a Standard Imaging Supermax electrometer (Standard Imaging, Middleton, WI, USA) set in the low-dose sensitivity range with an applied potential bias of +300 V. The pelvis spotlight CBCT procedure is usually calibrated using a half bow-tie filter, but we chose to characterize the pelvis spotlight protocol using a full bow-tie filter, as Varian® suggests it reduces the CTDI$_w$[162]. Furthermore, it allowed us to directly compare our results with similar measurements reported by Palm *et* al.[131].
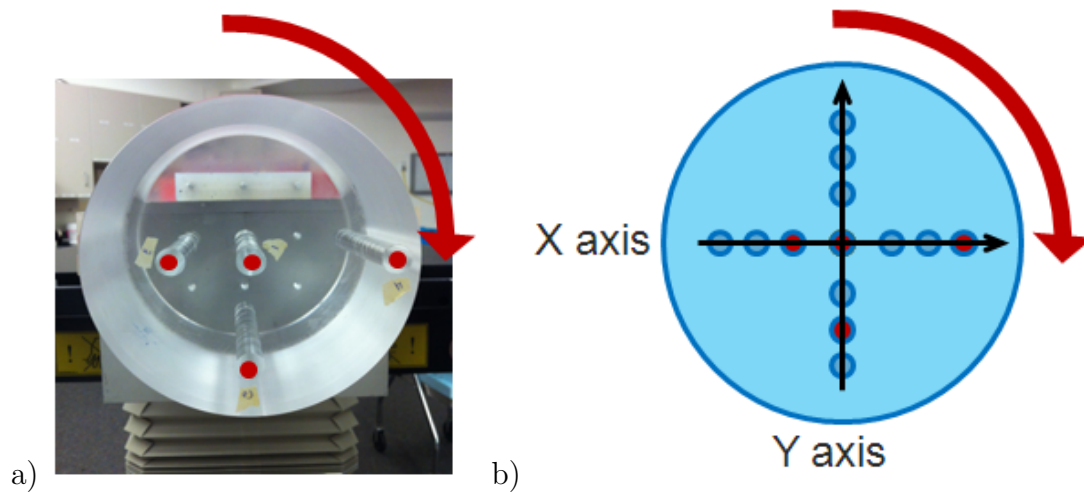
Figure 4.1: Cylindrical acrylic phantom (a) with dots showing possible ionization chamber positions at radii r = 0, 3.6, 5.2 and 6.6 cm, respectively. The phantom can be rotated in increments of 90° which allows dose measurements along the x and y-axes (b).

Validation

We irradiated two phantoms using the characterized OBI® 1.4 CBCT default imaging protocols to validate our approach. To provide validation in homogeneous and heterogeneous patient-mimicking geometries, we used a cylindrical acrylic phantom similar to a CTDI head phantom and an anthropomorphic phantom, respectively.

Cylindrical homogeneous phantom measurements

A 15.2 cm-diameter acrylic phantom was constructed for experimental validation in a homogeneous phantom. Holes were drilled to accommodate the Capintec 0.65 cc ionization chamber at the centre and at three different radii as shown in Fig. 4.1a. The phantom is designed to rotate in 90° increments to enable dose measurements at 13 different positions (Fig. 4.1b). A fitted acrylic sleeve accommodates the ionization chamber at the measurement points of interest, while the other holes are filled with whole acrylic rods.

The centre of the acrylic phantom was placed on a support so as to hang at the end of the couch, so that the beam would not be attenuated by the couch. We positioned the phantom

at the isocentre of the beam using the in-room patient positioning lasers (calibrated monthly to within 1 mm accuracy) and imaged for each characterized CBCT setting (Table 4.1). The dose was measured at each of the 13 points consecutively for all CBCT settings. To assess the error due to positioning and output fluctuations, we repeated the measurements over three days and found that the measurements were reproducible within $\pm$ 0.8%.

Cylindrical homogeneous phantom calculations

We constructed idealized DICOM images matching the physical dimensions of our homogeneous cylindrical phantom. The image was comprised of $512 \times 512 \times 91$ voxels ($\sim$23.8 million voxels) with dimensions of $0.81 \times 0.81 \times 3$ mm^3 in the x, y and z directions respectively. The phantom it represents was fabricated with acrylic material by our machine shop with a diameter of 15.2 cm and a length of 22 cm (more details under dose measurements: cylindrical phantom). We used the nominal acrylic molecular composition $C_5O_2H_8$ and the measured physical density of 1.16 g/cm^3 to calculate the atomic number density (atom/cm^3) for each element required by kVDoseCalc. We computed profiles along the x and y axes (Fig. 4.1b).

Anthropomorphic phantom measurements

We measured the absorbed dose inside the anthropomorphic RANDO phantom using high-sensitivity MCP-N (LiF:Mg,Cu,P) TLD chips (Radcard, Krakow, Poland). We positioned the 4.5 mm diameter and 1 mm width TLD chips in the pre-drilled holes in the RANDO phantom. They were held in place by two small acrylic cylinders positioned in a way that sandwiched the chips between them, minimizing any potential air-gaps. The locations of the TLDs (Fig. 4.2) were chosen to sample as many positions and tissues as possible within the two central slices of the relevant anatomical site (i.e., pelvis, thorax, or head). The sites were imaged using the appropriate default CBCT imaging technique (Table 4.1). We positioned the phantom by aligning the in-room positional lasers to external markers recognizable on the DICOM image used in the dose computation.
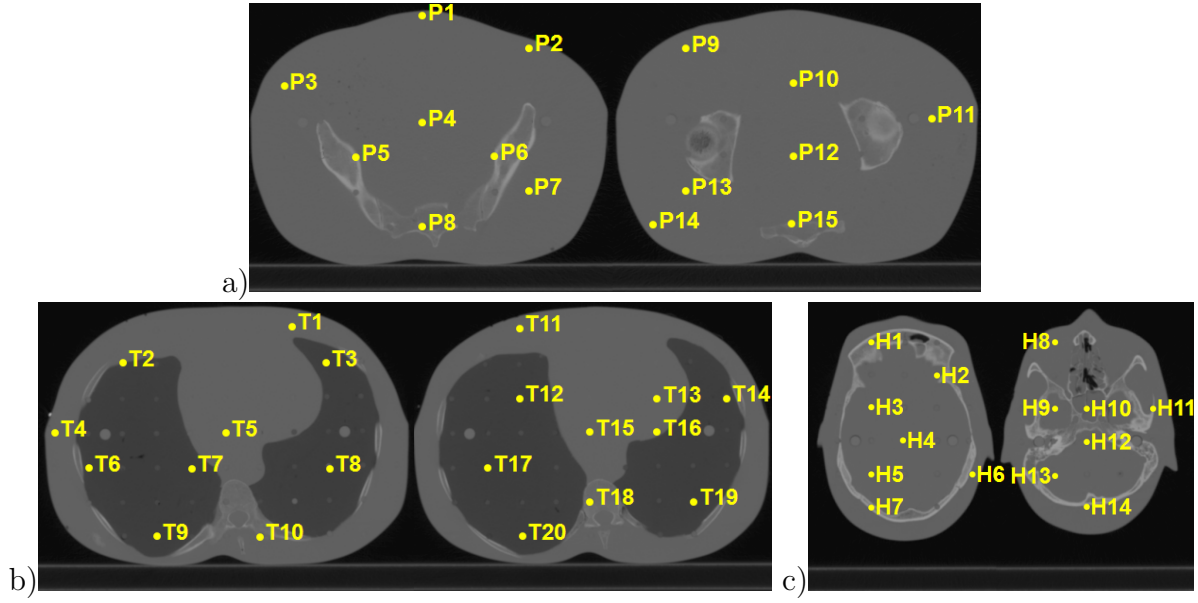
Figure 4.2: Measurement and computation points inside the anthropomorphic RANDO phantom in the pelvis (a), the thorax (b), and the head (c). Points are numbered from left to right, top to bottom.

Anthropomorphic phantom calculations

We computed absorbed dose inside the anthropomorphic RANDO phantom (The Phantom Laboratory, Salem, NY, USA) comprising tissue and lung-equivalent materials, and human bones. We imaged the RANDO phantom using a Brilliance Big Bore CT scanner (Phillips Healthcare, Best Netherlands) and imaging protocols standard in our institution: the head ($512 \times 512 \times 191$ voxels of size $0.70 \times 0.70 \times 2.5$ mm^3) and body ($512 \times 512 \times 236$ voxels of size $0.81 \times 0.81 \times 3$ mm^3) scans. The CT image was exported in DICOM format to use in kVDoseCalc. We assigned material compositions and physical densities to ranges of HU (see Table 4.2). The bones vary according to the imaging site (e.g., femurs in pelvis), so we only implemented the relevant bone types for the relevant sites. The manufacturer provided the nominal material compositions (expressed in mass percentage) and physical densities for the RANDO tissue and lung-equivalent materials. We used published values from the International Commission on Radiation Units and Measurements (ICRU)

131

Table 4.2: HU to materials conversion table

Imaged location	HU range	Material	Physical Density (g/cm^3)
Pelvis	-1000 − -300	Air	0.00120
	-300 − 50	RANDO (tissue)	0.997
	5 − 100	Bone marrow	1.03
	100 − 400	Femur	1.33
	400 − 10 000	Cortical bone	1.92
Thorax	-1000 − -750	Air	0.00120
	-750 −300	RANDO (lung)	0.352
	-300 − 50	RANDO (tissue)	0.997
	50 − 10 000	Cortical bone	1.92
Head	-1000 − -300	Air	0.00120
	-300 − 50	RANDO (tissue)	0.997
	50 − 10 000	Cortical bone	1.92

report 46[82] for the various bone material compositions and physical densities assuming adult bones.

While the number of photons seeded is sufficient to lower the statistical uncertainty of our computation below 1%, the TLDs have a finite size across which the dose may vary. We computed the absorbed dose over a uniform distribution of POIs corresponding to the physical size of the detectors (3 pixel radius ($\sim$2.46 mm) and 1 pixel length). The uncertainty due to the dose gradient over the detector measurement volume was assessed by the standard deviation over the average dose of these points.

Absorbed dose calibration

The output of the Varian® OBI® 1.4 imaging unit was evaluated using the in-phantom method outlined by the AAPM's Task Group 61 (TG-61)[111] guidelines on kilovoltage-energy dosimetry. We used the same ionization chamber and electrometer used to characterize the x-ray beams. The ionization chamber was placed at a depth of 2 cm in Gammex solid water with 6 cm of backscatter. The outputs corresponding to a calibration exposure of 160 mA and 160 ms (25.6 mAs) were measured for a calibration field (20$\times$20 cm^2) and the relevant CBCT fields (Table 4.1) for each energy and filter combination. We verified that the output linearity of the imaging unit was within 1% for the relevant imaging exposures

by measuring the dose with varying currents and time settings.

TLD characterization

According to the manufacturer, MCP-N TLD chips exhibit a sensitivity 30 times greater than conventional MTS-N (LiF:Mg,Ti) TLDs and have a detection threshold of 50 nGy making them ideal for measuring the low absorbed doses deposited by CBCT imaging procedures. Furthermore, while conventional MTS-N TLDs exhibit an energy response limiting their use in kV dosimetry applications, Duggan *et al.* showed that MCP-N TLDs are not significantly energy-dependent at low energies[55].

Unlike TLD powder, TLD chips can only be read once before they must be annealed to restore their sensitivity. Following the manufacturer's guidelines, the chips were annealed at 100 °C following an irradiation to eliminate noise due to low-energy electron traps. The TLDs were then read by a photomultiplier tube (PMT) at a temperature of 240 °C, after which they were annealed at a temperature of 240 °C. Each annealing was followed by a rapid cooling by placing the chips directly on an aluminum surface.

To assess the reproducibility of the TLD chips, they were irradiated five times at the centre of a 20×20 cm^2 beam in a phantom of therapy-grade Solid Water (Gammex® 455, Gammex Inc, Middleton WI, USA) at a depth of 2 cm and with 6 cm of backscatter. The phantom was placed at a source-to-surface distance (SSD) of 100 cm and irradiated with a technique setting of 160 ms and 160 mA (25.6 mAs) using the relevant energies and corresponding bow-tie filter. The response of the TLD chips stabilized after 3-5 irradiation/annealing cycles. We observed that the average sensitivity of the TLD batch could vary from one exposure to the next, but that the response of an individual chip against the average of the whole never varied by more than 3%. Therefore, three chips were kept aside during every experiment and exposed using the calibration dose to eliminate the uncertainty related to variations in sensitivity between annealing cycles. Once stabilized, the standard deviation of five consecutive exposures was used to assess the reproducibility of the TLD

readings, and was found to range from 1-3%. The dose response of each TLD chip was individually determined over a range of three different exposures (mAs) by a linear fit of the measured charge (Q) and the absorbed dose (D), as shown by the following expression

$$D = mQ + b, \tag{4.1}$$

where m and b represent the slope and intercept of the linear fit, respectively. Values for the absorbed dose D were obtained by ionization measurements under the same conditions. The uncertainty in the absorbed dose ΔD_i was estimated by the expression

$$\Delta D = Q\Delta m + m\Delta Q + \Delta b, \tag{4.2}$$

where Δm and Δb represent the TLD-specific fit uncertainties of the slope and intercept, respectively, and ΔQ represents the uncertainty in measured charge, where $\Delta Q/Q$ is the normalized standard deviation of the TLD readings discussed earlier. These characterizations were carried out for each energy shown in Table 4.1.

Tissue conversion factors

At low kV energies, electrons have a maximum range in the order of micrometers, so they can be considered to be locally absorbed[89]. Therefore, the dose measured by the TLD depends only on the incident photon fluence, and no tissue-specific calibration is required when the chips are placed in the RANDO tissue and lung-equivalent materials. Since the chips were characterized in Gammex solid water, they report absorbed dose to tissue-equivalent material. The TLDs were placed in RANDO cavities usually occupied by a tissue-equivalent spacing plug. Therefore, the dose to the tissue-equivalent material was measured and not the dose to bone or lung-equivalent materials. Therefore, there is no need to account for bone-to-tissue conversion factors. In the thorax, spacing plugs are comprised of lung-equivalent material so a lung-to-tissue factor is required to convert dose to lung to dose to tissue. We obtained this factor empirically by using kVDoseCalc to compute the dose in a voxel

located in a cylinder of lung-equivalent material, then replacing that same voxel with a tissue-equivalent voxel, and using the ratio of both quantities as the conversion factor.

4.2.4 Results

Cylindrical acrylic phantom

The agreement between ionization chamber measurements the dose computed with kV-DoseCalc within the cylindrical acrylic phantom is within 2% of the local dose for most points (Fig. 4.3). There is an abrupt dose drop-off at a radius of 6.8 cm in the pelvis and low-dose thorax beams (Fig. 4.3a and c). For 200° arc size scans (Fig. 4.3b and d), the measurements agree with computation to within 2% of local dose for the standard-dose head scan and within 4% for the pelvis spotlight scan.

Anthropomorphic phantom

We compared TLD dose measurements to kVDoseCalc computation in Figs. 4.4, 4.5. Figure 4.4 shows that the calculated dose correlates very well with measured values. The local percent difference is usually within 10%, and always within 20% except in the head and a single point for the pelvis protocol.

We calculated the average and standard deviation of the percent difference in local absorbed dose between measurement and computation, and found that it varies between 2.4 ± 6.0% and 5.7 ± 10.3% according to the site and imaging protocol. The low-dose thorax offers the best agreement with an average of -2.4% and a standard deviation of 6.0%, and with the measured and computed dose error bars overlapping for every point. The thorax is also the imaging site exhibiting the least variation in structures as the lung-equivalent material is fairly homogeneous, and the ribs and spine are the only significant bony structures. Conversely, the standard-dose head scan showed the most variation (-4.1 ± 26.9%) in agreement, because it is the geometry which exhibits the most heterogeneity (e.g., dense

a)

b)

136

c)

d)
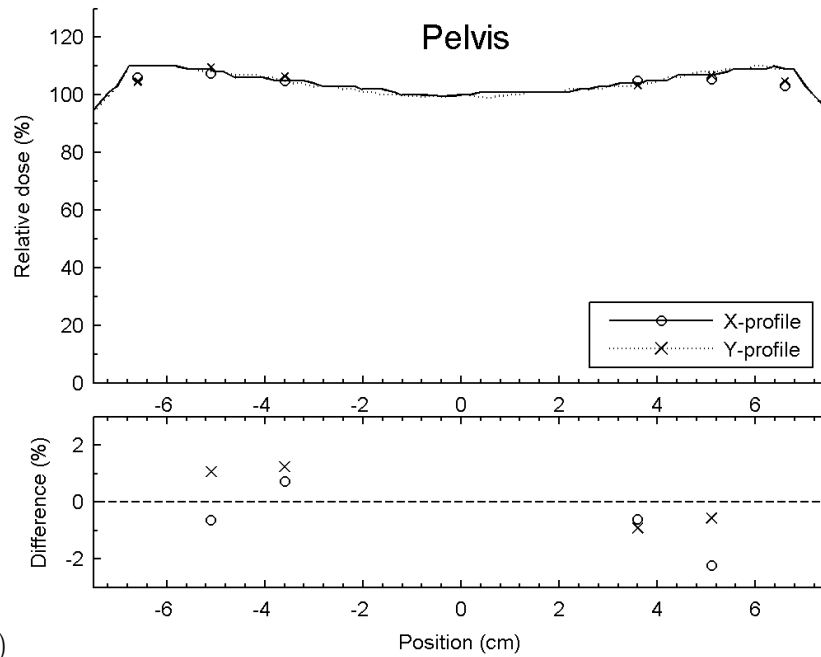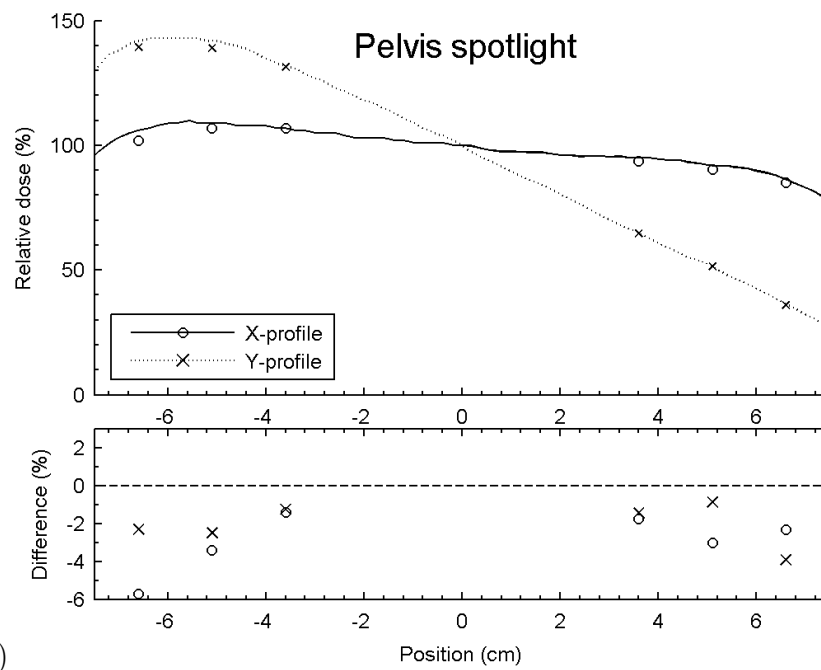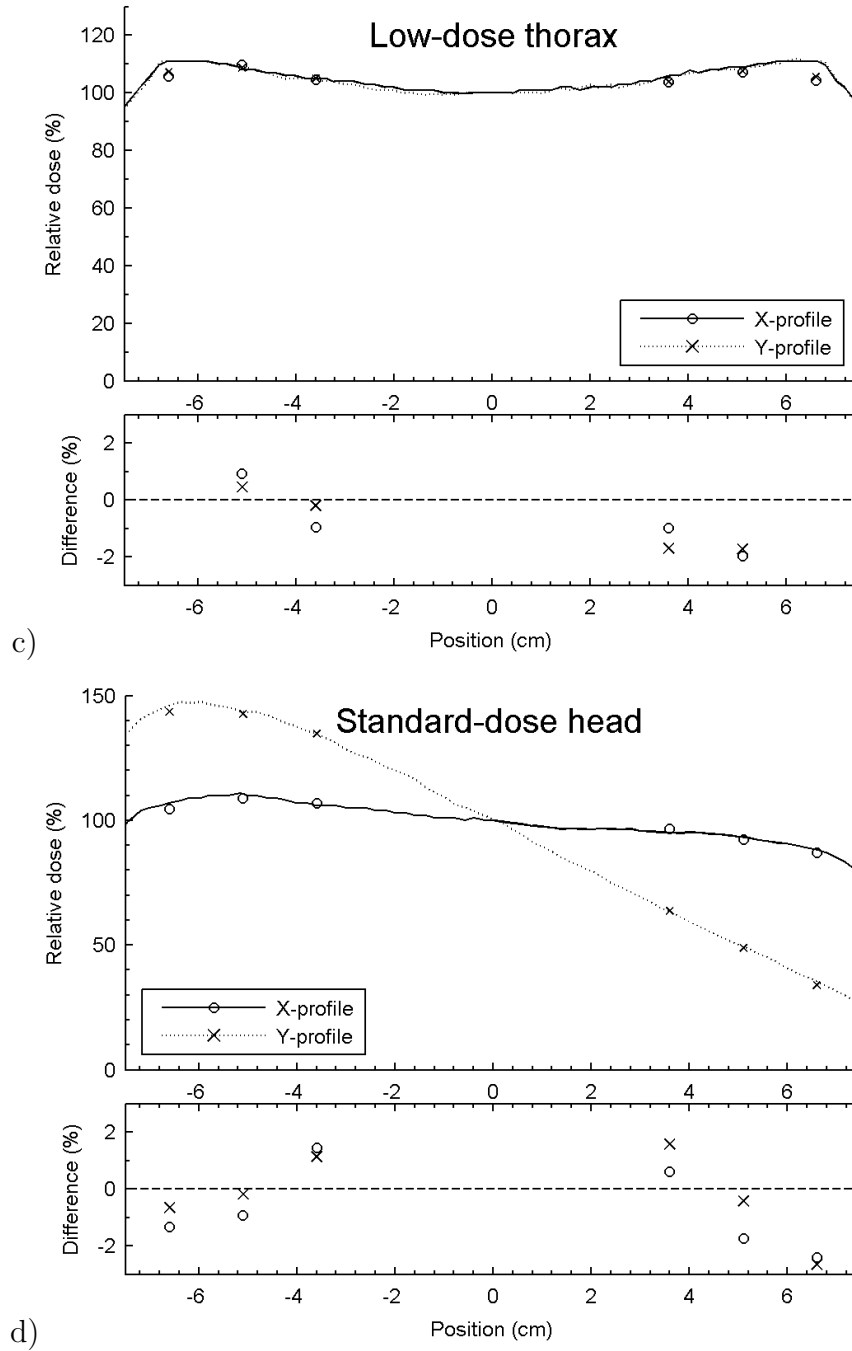
Figure 4.3: (a) to (d) Comparison between measured (circles and crosses) and computed dose (lines) relative to the centre of the cylindrical acrylic phantom for each imaging protocol shown in Table 4.1. Axes are defined according to Fig. 4.1. Positive differences mean that measurements are higher than calculations and vice-versa.
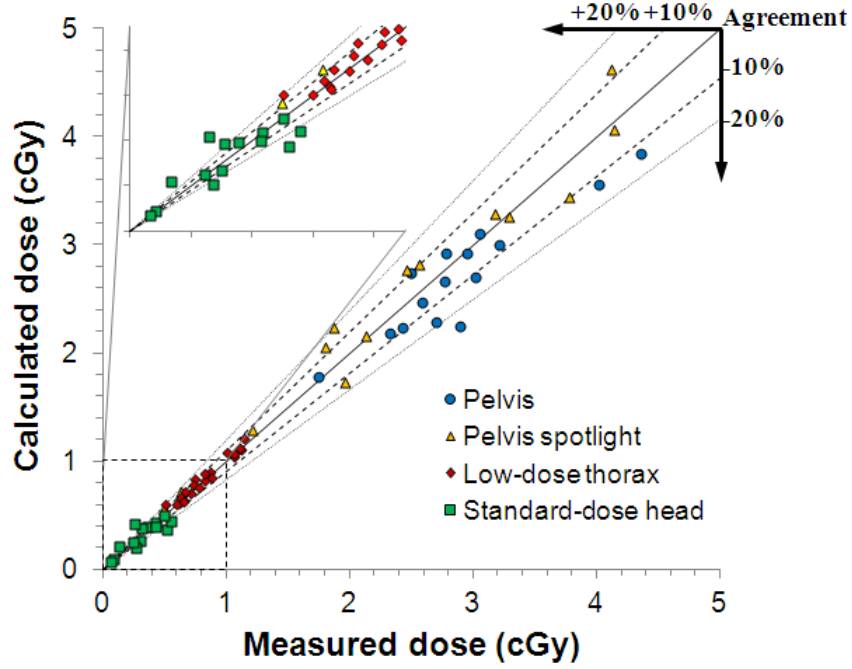
Figure 4.4: Comparison between measured and computed dose inside the anthropomorphic phantom for all imaging technique settings. The full line indicates a perfect agreement (slope =1), while the doted lines indicate discrepancies ranging from -20–20%. For all imaging techniques, except for the standard dose head, most of the measurements agree with kVDoseCalc computations within 10%. Only a single point for the pelvis protocol has a disagreement larger than 20%.

Table 4.3: Summary of the measured and computed dose in the anthropomorphic phantom.

CBCT procedure	Pelvis	Low-dose thorax	Pelvis spotlight	Std.-dose head
TLD (cGy)	1.78–3.84	0.60–1.12	0.56–4.62	0.07–0.50
kVDoseCalc (cGy)	1.75–4.35	0.51–1.12	0.50–4.14	0.07–0.56
Palm et $al.^{a)}$ (cGy)	2.4–3.1	0.9–1.7	0.5–6.0	0.1–0.6
$CTDI_w^{b)}$ (cGy)	1.77	0.47	1.44	0.39
Avg. agreement	$5.6 \pm 8.3\%$	$-2.4 \pm 6.0\%$	$-5.7 \pm 10.3\%$	$-4.1 \pm 26.9\%$
Pass/fail	8/15 (53%)	20/20 (100%)	8/14 (57%)	5/14 (36%)

a) Measured TLD dose in anthropomorphic Alderson phantom by Palm et $al.$, 2010[131].
b) Nominal values from the Varian® OBI® Reference Guide[162].

and shallow bones, air cavities). In contrast, the two pelvic scans (pelvis & pelvis spotlight) showed similar results (5.6 ± 8.3% and -5.7 ± 10.3% respectively) which suggests that the imaging site, and consequently the HU-to-materials conversion, is the most important factor determining the agreement between computation and measurement.
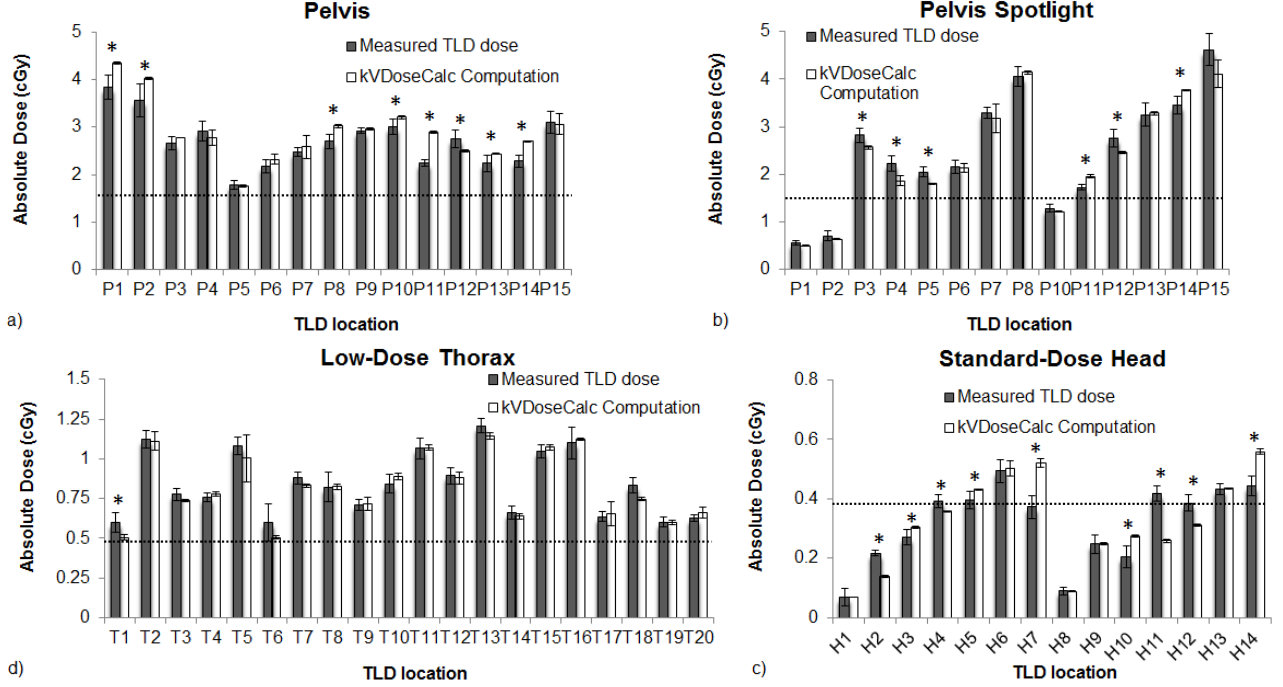
Figure 4.5: Comparison between measured absorbed TLD dose (white columns) and kVDose-Calc computations (grey columns) for the pelvis (a), pelvis spotlight (b), low-dose thorax (c) and standard-dose head (d) CBCT default parameters. The error bars of the measured values generally overlap with those of the computed values. Points for which the error bars do not overlap are marked with an asterisk (∗). Generally speaking, imaging techniques with a 200° arc (b and d) deposit less dose in the anterior and more dose in the posterior regions of the phantom, hence the somewhat monotonic increase of dose with measurement point in these figures. The dotted line indicates the nominal $CTDI_w$ dose for that imaging protocol as a means of comparison. The results are further summarized in Table 4.3.

A point-by-point comparison is shown in Fig. 4.5. While the agreement is generally good, it is not always within experimental uncertainty. We see that most of the error bars associated with the measured value overlap with those of the computed values, ranging from 36 to 100% of the values depending on the imaging protocol (Table 4.3). Figure 4.6 shows the location of the points in which error bars do not overlap.
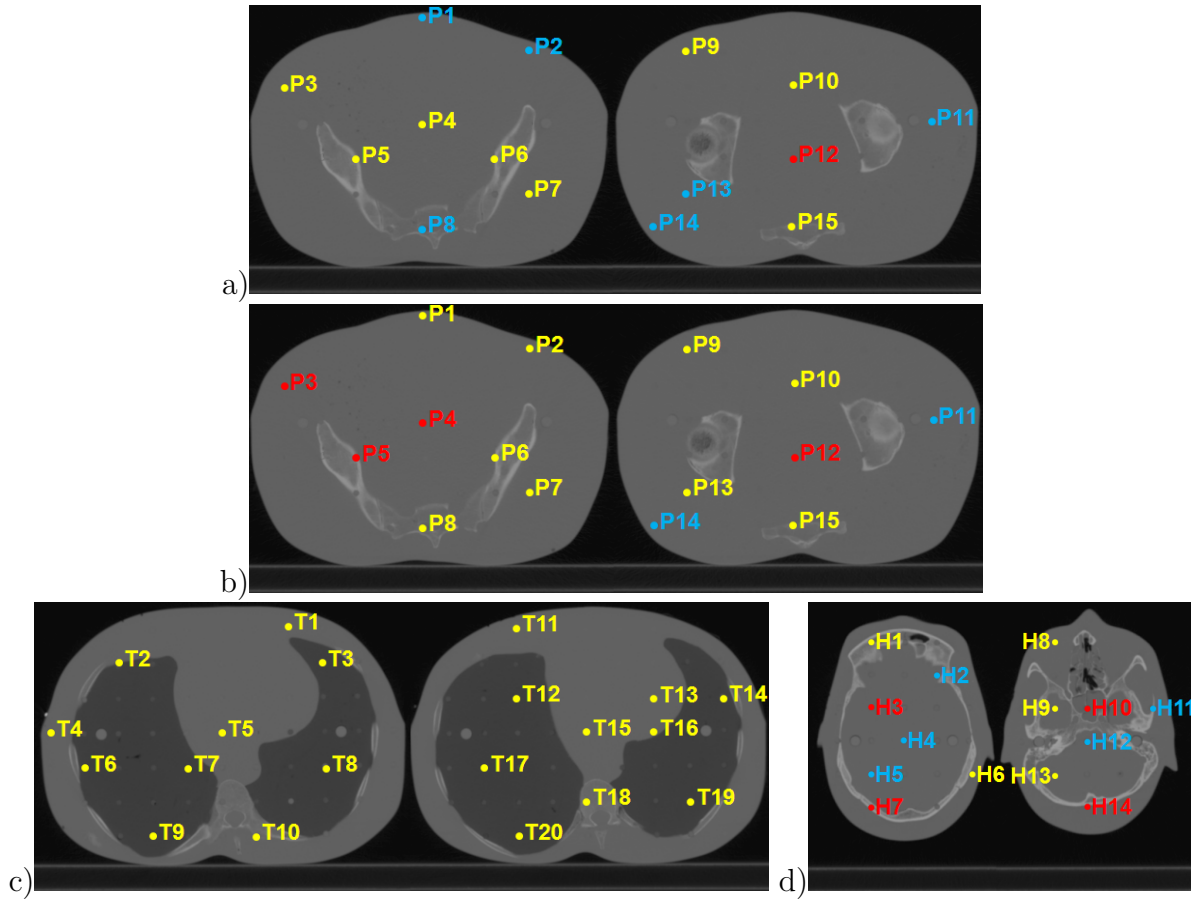
Figure 4.6: Points inside the anthropomorphic phantom where the computed and measured dose intervals of confidence do not overlap for the pelvis (a), the pelvis spotlight (b), the low-dose thorax (c), and the head (d) scans. Yellow points show where the intervals of confidence overlap, while blue and red points indicate where the computed dose is lower or higher than TLD measurements and the error bars do not overlap, respectively.

4.2.5 Discussion

Cylindrical homogeneous phantom

The percent difference between kVDoseCalc computation and measured dose relative to the centre in the homogeneous cylindrical phantom is ≤2% except in regions of high gradient for both 360° procedures. For these procedures, points measured at the outermost position (r = 6.6 cm, see Fig. 4.1) are sampling the high-gradient region of the field where the x_1=6.8

cm blade defines the edge of the high-intensity side of the beam. Thus, there is a dose volume averaging effect in the 6mm-diameter ionization chamber which leads to the measured dose being lower than computation, with a distance-to-agreement of ≤ 2 mm.

As we mentioned previously, our software computes the dose deposited the primary, first scattered and multiple-scattered photons separately. Our dose computation software, kVDoseCalc, had previously been validated only for radiographic exposures incident on flat surfaces where there were no contour effects. In contrast, this study involves a rotating beam incident on a round phantom. At the centre of the phantom, about 50% of the dose is deposited by the scattered component. An accurate computation of the dose in this region therefore requires not only an accurate characterization of the beam and geometry, but also an accurate computation of these multiple scattering events.

Our results show that kVDoseCalc can calculate the dose delivered by a rotating beam incident on a curved homogeneous surface, even in the presence of experimental and theoretical difficulties, with the same accuracy as previously achieved in flat phantom surfaces[137].

Anthropomorphic phantom

We compared TLD dose measurements to kVDoseCalc computations in the anthropomorphic phantom for four different default CBCT imaging protocols (Fig. 4.5). These comprise three different imaging locations, three energies, two bowtie filters (Table 4.1), and a number of different materials (e.g., RANDO tissue and lung-equivalent materials, cranial, spine and femoral bones). Despite the great variety in measurement conditions and a range of two orders of magnitude in the measured dose (0.07 to 4.62 cGy), we obtain excellent correlation between measured and calculated values (Fig. 4.4). For all four imaging protocols, the average of the local dose percent difference is close to zero, which shows that there is no obvious systematic difference between computation and measurement. While the error bars TLD measurements do not overlap with computed values in all cases, we should point

out that these error bars only represent uncertainties which can be evaluated quantitatively such as TLD reproducibility and uncertainties in the linear fit in the TLD characterization. They do not include uncertainties due to CT image artifacts and tissue segmentation, which are much more difficult to evaluate.

Palm *et al.*[131] measured the CBCT dose in a similar anthropomorphic phantom imaged using the same CBCT protocols, but in different locations. As shown in Table 4.3, our measurements generally fall within the same range as Palm *et al.*'s for all CBCT scans[131]. These results provide some further validation for our methodology.

We also confirm Palm *et al.*'s report that absorbed doses in the anthropomorphic phantom are generally about twice as high as the nominal $CTDI_w$, except for head scans[131]. This is explained by differences in sizes between a body CTDI phantom and RANDO. Indeed, the latter is $\sim 57\%$ smaller in volume than the former, so the beam experiences less attenuation. Conversely, the head CTDI phantom is only $\sim 90\%$ smaller in volume than RANDO's head, so the nominal $CTDI_w$ is a better estimate of the absorbed dose. This confirms previous reports that the CTDI is not adequate to estimate the patient-specific absorbed dose[27, 28, 23]. While the nominal value of the CTDI in the head falls within the same order of magnitude as measured doses in the anthropomorphic phantom, it fails to account for the large (0.07-0.49 cGy) dose variations throughout the volume.

There are other methods currently being developed to estimate the patient-specific CBCT dose, such as conventional MC algorithms[45] or an adapted MV commercial TPS[7]. A study by Alaei *et al.* compares TLD measurements, adapted MV TPS calculations and conventional MC computations inside an anthropomorphic phantom[7]. The agreement we obtained is slightly better than that obtained by adapted TPS (-8% to 8% average percent difference)[7], and comparable to that obtained by conventional MC modeling (0.3% to 7.9% average percent difference)[7]. Another MC validation in an anthropomorphic phantom was performed by Li *et al.* who modeled a conventional CT scanner. They found that the local

difference between MC simulation values and TLD measurements ranged from -17.2% to 13.0%, which are comparable to our results.

The main advantage of kVDoseCalc is that its characterization relies on a handful of empirical values which can be measured using equipment available to most radiation therapy clinics. It is therefore easier to implement than conventional MC simulation. While adapted MV TPS are interesting due to their clinical feasibility, they still require the measurement of many percent depth-dose and profile curves[7] which represent more measurements than required using our method to characterize and model an x-ray source.[137].

These results show a proof of principle of our approach. That is, it is possible to import a CT data set into in kVDoseCalc and calculate patient-specific dose from CBCT procedures with reasonable accuracy. This absorbed dose calculation is more accurate than the CTDI values usually used to estimate CT and CBCT dose.

Our method has been validated computationally against MC simulation techniques[103], we therefore know that we are accurately modeling the physics involved in kV x-ray dosimetry. However, the absorbed dose in a patient can only be accurately computed if the input parameters are accurate. We have previously validated both our x-ray source/beam characterization method and kVDoseCalc experimentally for a stationary beam incident on homogeneous and heterogeneous phantoms[138, 137]. The homogeneous cylindrical phantom measurements in this work show that kVDoseCalc can accurately compute the dose deposited by a rotating x-ray source defining a rotating beam incident on curved surfaces. Therefore, in principle one should be able to accurately compute the dose in an anthropomorphic phantom, as there are no additional conceptual difficulties. However, computing the dose in anthropomorphic phantoms or patients introduces procedural sources of error that are not specific to kVDoseCalc, in particular the issue of accurate tissue segmentation.

Tissue segmentation

Transport-based calculations, whether performed using conventional MC software or kV-DoseCalc, rely on the accurate description of the x-ray source and the irradiated volume. Our source model was validated in previous work using block phantoms that removed errors due to physical densities and material compositions[137]. However, real patients and anthropomorphic phantoms contain bones in which the physical density and effective Z varies significantly due to differences in high-Z phosphorus and calcium content[193]. While soft tissues also vary in density and material composition, they do so to a far lesser extent[184].

The difficulties in segmenting the irradiated volume into ranges of physical densities and material compositions introduces errors in both photon transport and fluence-to-dose conversions[177]. According to a study by Zhou *et al.*[193], using the common three-tissue HU-to-material segmentation scheme to compute the dose deposited by a 120 kVp beam can lead to errors of up to 100% in bone and up to 30% in adjacent soft tissues. They propose a 42-bones segmentation scheme for accuracy within 2.5% throughout the volume[193]. In addition to the conventional HU, images taken with a dual-energy CT scanner yield volumetric effective Z. Bazalova and Greaves have proposed a 39-tissues segmentation scheme based on both of these quantities for even greater accuracy compared to a 4- or 8-tissue segmentation scheme[13]. However, we should point out that this increased accuracy is presumed based on the assumption that dose computations using a more detailed model are necessarily more accurate. This assumption has not been experimentally validated.

We found that the fraction of points where measured and calculated dose error bars overlapped was best in the thorax (20/20) and worst in the head (5/14). The thorax contains few complex bony structures, while the head contains a larger variation in bone HU. Thus, we suspect that the agreement between measured and calculated dose, as well as the accuracy in calculating dose in patients, could be improved by implementing a more complex tissue segmentation scheme. At the moment, kVDoseCalc is not designed to accommodate such a

large number of tissues. The issue of tissue segmentation will be addressed in future work to improve the accuracy of kV CBCT dose computations, whether performed by conventional MC approaches, or by kVDoseCalc.

Despite the limitations of tissue segmentation, the approach validated in this study represents a convenient, clinically feasible method for calculating the absorbed dose in a patient-mimicking phantom within reasonable accuracy.

4.2.6 Conclusion

This study provided experimental validation of an in-house dose computation software (kVDoseCalc) to compute the machine and patient-specific dose deposited by kV CBCT imaging procedures. While the software had been previously validated computationally[103] and experimentally for open beams[138] and beams with additional bow-tie filters[137] in radiographic geometries, this is the first validation including a rotating x-ray source fully modeling CBCT imaging protocols. We showed that kVDoseCalc can be used to calculate the absorbed dose in a homogeneous cylindrical phantom and the anthropomorphic RANDO phantom within reasonable accuracy. This study represents a final proof of principle of the development of a fast and accurate patient-specific dose computation system for kV IGRT imaging procedures. Further studies will focus on exploiting the flexibility of our x-ray source characterization method and kVDoseCalc to characterize other kV x-ray sources such as superficial and orthovoltage therapy units, improving accuracy by implementing a more comprehensive tissue-segmentation, and developing methods to rapidly and accurately compute absorbed dose to not just POIs but over entire volumes.

4.3 General conclusions

This chapter provides the final validation of our source model and dose computation method. Compared to other anthropomorphic phantom validations, our approach is of comparable accuracy to the much more complex MC approaches, and more accurate than the simpler TPS-based approaches.

The work presented in this chapter is very sensitive to tissue segmentation. While the anthropomorphic phantom is comprised of heterogeneous structures–especially the bones–the tissue and lung equivalent materials are approximately homogeneous. Tissue segmentation in a real patient would certainly be more complex and requires future work.

The goal of this thesis, namely the development of a feasible kV x-ray source model and characterization method, has been achieved. However, there is room for improvement before the method can be applied in routine clinical use. These improvements will be the subject of future work and are described in the following chapter.

Chapter 5

Conclusions and Future work

5.1 Conclusions

In this thesis, we hypothesized that it was possible to model and characterize a kV x-ray source using only empirical quantities measured using equipment common to all medical physics clinics without need for specialized knowledge of Monte Carlo calculations. While the method was developed for the kV dose computation software developed by Dr. Alexei Kouznetsov and Dr. Mauro Tambasco, it is not specific to it and could in principle be used for other dose computation methods. The model depends on characterizing the spectrum of the beam using the nominal kVp and measured HVL at various positions along the transverse axis, and thereby deriving empirical values for the fluence.

The first part of this thesis focused on developing and validating a simplified spectrum characterization method. This method can characterize a spectrum using only the nominal kVp and measured HVL and can be useful in applications where the spectrum is relatively invariant and the only quantity of interest is the depth-dose profile, such as in section 5.2.3. We performed a sensitivity analysis of the effect of HVL and kVp variations on dose deposition which showed that the experimental uncertainty of these values did not lead to significant errors. Validation performed for radiographic imaging of homogeneous and heterogeneous block phantoms showed that, while the method provided reasonable accuracy in computing transverse-axis profiles, a more detailed approach would be required for modeling the addition bow-tie filters.

This more detailed approach was presented in Chapter 4, in which we explained the full formalism of our proposed virtual point source model and characterization method.

This method involved using the previously-validated spectrum characterization method to characterize the spectrum along the transverse axis of the beam, and the fluence is derived from in-air transverse kerma profiles. We validated the method with radiographic imaging of homogeneous and heterogeneous block phantoms.

Finally, we performed a validation for CBCT rotating beams in a homogeneous and a heterogeneous anthropomorphic phantom. The validation inside the homogeneous cylindrical phantom showed that the rotating x-ray source model and beam characterization in kVDoseCalc could accurately handle curved surfaces and rotating beams. Finally, the anthropomorphic phantom validation showed that our method could be used to calculate dose in a patient-mimicking geometry within reasonable accuracy.

In summary, we showed that the virtual point source model and beam characterization method proposed in this thesis could accurately model kV beams for radiographic and CBCT imaging procedures. The model is more accurate and simpler to characterize than converted TPS algorithms, and does not require the specialized techniques used in conventional Monte Carlo packages. The main advantage of the method is its simplicity and flexibility: using simple in-air dose measurements, one can characterize and model the kV x-ray source without need for specialized equipment. Furthermore, this model and characterization method are not unique to assessing dose from kV imaging, but can be used for assessing dose from superficial and orthovoltage radiation therapy as well (see section 5.2).

At the beginning of this project, kVDoseCalc had already been validated computationally, but it was for a simple geometry that was not representative of a real clinical setting. During the course of this thesis, the software was modified, experimentally validated, and shown to accurately compute the absorbed dose in a patient-mimicking phantom. While the main scientific contribution of this thesis is the x-ray source model and beam characterization method, this work also shows a proof of principle for the use of kVDoseCalc in a clinical setting. Although further improvements are required before kVDoseCalc is ready for routine

clinical use, it has already been helpful in solving a clinical issue (see 7.2.4).

Recently, a similar model was published by McMillan et al.[119] to describe kV CBCT x-ray sources. This model is similar in that it also characterizes the spectrum via kVp and HVL. However, in this proposed model, the effect of an added bowtie filter is modeled by an effective aluminum thickness through which the x-ray beam is attenuated. This effective bowtie filter both hardens and attenuates the beam, meaning that the fluence and spectrum of the beam are dependent on one another. In contrast, the model proposed in this thesis characterizes the spectrum and the fluence independently, although more studies would be required to determine which model allows the most accurate dose computations.

5.2   Other applications

Over the course of this thesis, I became involved in a number of studies in which the virtual x-ray point source model and beam characterization method were used in other applications. While I was heavily involved in all of these projects, my role was to support the investigation and provide advice rather than performing the majority of the work. For this reason, and since these studies are not directly related to the main focus of this thesis (i.e., modeling kV CBCT imaging beams), they were not included as chapters in the main body of the text. Nevertheless, they bear mentioning for successfully showcasing the flexibility and wide applicability of the method proposed in this thesis.

5.2.1   Conventional CT scanners

I aided Mitch Sommerville (another graduate student supervised by Dr. Mauro Tambasco) characterize the transverse axis fluence and spectrum of a Phillips Big Bore conventional CT scanner (Philips Medical Systems, Best, Netherlands) following the method outlined in Chapter 4. Third-party data was used to model the longitudinal z-axis of the

beam to avoid uncertainties due to the volume averaging effects in the ionization chamber which could become important due to the small thickness (four slices of 6 mm each = 2.4 cm) of the beam. Since kVDoseCalc is not currently designed to accommodate helical beams, we limited ourselves to modeling a single-slice axial scan of the homogeneous cylindrical phantom depicted in Chapter 4 for three energies: 90, 120 and 140 kVp. Ionization chamber measurements of the dose relative to the centre of the phantom agreed with kVDoseCalc computation within a maximum percent difference of 3.64%. This work was presented at the AAPM 2013 Annual Scientific Meeting in Indianapolis[154], and a completed manuscript is currently undergoing revision for submission to Medical Physics with the title *A measurement based x-ray source model for CT dosimetry computations.*.

5.2.2 Superficial Therapy

I aided Christopher Johnstone (another graduate student supervised by Dr. Mauro Tambasco) characterize an Xstrahl 150 superficial kV therapy unit following the method outlined in Chapter 4 for three cone sizes (2, 5 and 15 cm diameter) and four energies (80, 100, 120, and 150 kVp). Depth-dose and transverse axis profiles were measured in a water tank using an ionization chamber and compared to kVDoseCalc computations. We found that kVDoseCalc relative dose computations agreed with measurements within 3% of local dose in depth-dose profiles and 6% of local dose in transverse axis profiles. The depth-dose profiles were also compared to published data from the British Journal of Radiology supplement 25 (BJR 25)[92], where the maximum disagreement exceeded 6% of local dose at depths $\geq$ 3 cm and 10% at depths $\geq$ 5 cm. Since this published data currently represents the standard used to plan superficial therapy treatments, kVDoseCalc could be useful when treating structures at depths $\geq$ 3 cm. These results were presented at the COMP/CARO 2013 Joint Scientific Meeting in Montreal[90], and a completed manuscript is currently undergoing revisions in preparation for a submission to *Medical Physics*.

5.2.3 Radiochromic film dosimetry

In collaboration with Ferenc Jacso, Dr. James Grafe, Ian Nygren, Dr. Eduardo Villareal-Barajas and Dr. Rao Khan, I investigated the use of Gafchromic EBT3 radiochromic films for kV dosimetric applications, in particular depth-dose profile relative dosimetry. During the course of our investigation, we observed relatively large ($\leq 5\%$) discrepancies between ionization chamber and radiochromic film measurements. To provide additional confidence in our experimental results, we characterized the spectrum of an Xstrahl 300 orthovoltage kV therapy unit using the method outlined in Chapter 3 for 100, 150 and 200 kVp beams. Since we were not interested in accurate lateral dose profile computations, we assumed a flat fluence diverging due to the inverse-square law. kVDoseCalc relative depth-dose profiles fell between the extremes of ionization chamber and film measurements and agreed within 3.5% of all modalities. These results confirmed the validity of film dosimetry while underlining the experimental difficulties of kV dosimetry. They were presented at the COMP/CARO 2013 Joint Scientific Meeting in Montreal[85], and we are currently writing a manuscript for a submission in *Medical Physics*.

5.2.4 Standoff factor corrections

The field size in superficial and orthovoltage kV x-ray therapy is determined by applicator cones which can be either open or close-ended. In some patients, the applicator cannot be placed directly against the treated surface. These patients are treated at an extended SSD, and a stand-off correction is calculated using the inverse square law. In our clinic, our *in vivo* radiochromic film dosimetry program showed that some extended SSD patients were receiving a lower ($\sim 6\%$) dose than planned, even when calculating the stand-off factor. In collaboration with the same team as in 7.2.3, I modeled the 4 mm acrylic end-plate present in close-ended applicators in kVDoseCalc and computed in-air dose profiles. Figure 5.1 shows

that the results agree with ionization chamber measurements. The discrepancy is due to the fact that about 10% of the dose at the surface of the end-plate is deposited by photons scattering inside the end-plate. As the distance from the end-plate increases, the scattered component of the dose becomes less important and the in-air dose profile is better modeled by the inverse square law. The kVDoseCalc computations obtained from the application of the method in this thesis confirmed the experimental results and provided a theoretical explanation. These results were presented at the 2013 Alberta Cancer Foundation Annual Cancer Research Conference, and a manuscript describing these results was completed and has been accepted for publication in the *Journal of Clinical Applications in Medical Physics* under the title *Quantifying the divergence from the inverse square law and clinical significance for orthovoltage beams at extended SDD.* These results have been used to calculate an effective FSD to minimize dosimetric errors. This effective FSD is currently in clinical use.

5.3 Future Work

In this thesis, we characterized and validated our approach for default CBCT imaging technique settings. In practice, the user is able to change these settings (e.g., reduce imaging dose by using a smaller field size) while our characterization is beam-specific. The development of a dose computation tool truly analogous to a commercial TPS will need a more flexible approach requiring the characterization of different field sizes, output factors, and other similar quantities. A sensitivity analysis should be performed to determine how many fields need to be characterized for accurate computation of the dose. Furthermore, in chapter 3 and 4, we characterized the beams by measuring transverse axis HVL and kerma in-air profiles at intervals of 2 cm. While we have shown that this interval is adequate, there has been no investigation to determine if it is optimal.

In the same vein of thought, the kVDoseCalc GUI currently does not accommodate an interface for a reference dose calibration. In this thesis, calculated doses were converted
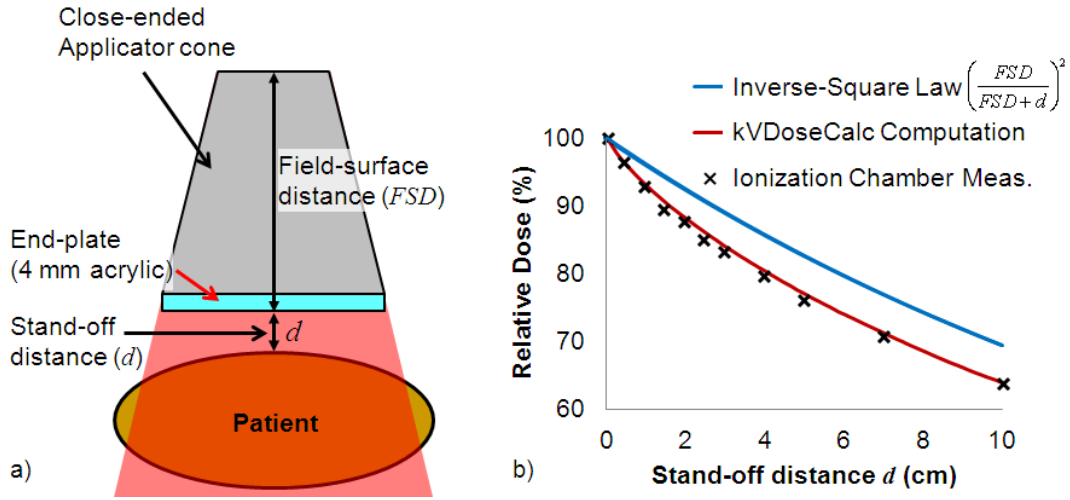
Figure 5.1: (a) Treatment geometry for orthovoltage therapy at an extended standoff. The distance from the endplate d is added to the applicator field-to-source distance FSD, with total distance from the x-ray source being $FSD + d$. Close-ended applicator cones of an Xstrahl 300 orthovoltage unit contain a 4 mm acrylic endplate in which photons scatter before entering the patient. (b) Relative dose in air as a function of d. Ionization chamber measurements do not follow the inverse square law $(FSD/FSD+d)^2$ prediction due to scatter in the endplate. kVDoseCalc computations agree with ionization chamber measurements and explain why the inverse square law fails to explain the behaviour of the stand-off factor in this geometry.

to relative doses, and a field-specific calibration factor was subsequently applied. This ad-hoc calibration factor is not appropriate for clinical applications, and a more comprehensive investigation of the relationship between field size and dose rate (i.e., output factors) will increase the clinical usability of the software.

In Chapter 5, we saw there was room for improvement in full bow-tie transverse-axis profiles computed in heterogeneous media. We hypothesized that the difference in width in the solid bone and lung-equivalent material was caused by approximation that all photons originate from a point-source, while in reality as many as 10% of the photons originate from scatter in the bow-tie filter[156]. By applying the characterization method described in Chapter 4 at two different SSDs, we could theoretically derive the component of the fluence originating from the focal spot on the anode separate from the rest of the fluence. We could

then investigate whether that leftover fluence could be approximated as originating from a single effective source point and whether this bifocal source model would increase agreement between computation and measurements in FBT heterogeneous transverse profiles.

As we mentioned earlier, the accuracy of dose computations inside a real patient will benefit from a more sophisticated tissue segmentation. For instance, Bazalova and Graves found that they needed to implement a segmentation scheme of 39 different tissues in order to obtain good accuracy[14]. Furthermore, they found that the segmentation based on mass density, which we used in Chapter 4, was insufficient for optimal tissue segmentation and proposed a scheme based on effective-Z instead[14]. A tissue segmentation scheme based on effective-Z requires a dual-energy CT scan, which should be investigated.

Currently, kVDoseCalc is capable of computing dose only to a series of POIs. In the future, the evaluation of full 3-D dose distributions will be required if the imaging dose is to be incorporated to the therapeutic dose in the radiation treatment plan. Dr. Tambasco and Dr. Kouznetsov are currently investigating the use of a sparse-grid based interpolation to estimate 3-D dose distribution from an optimal number of point calculations. This approach would greatly reduce the amount of computation required to obtain an accurate 3-D dose distribution compared to the conventional full grid used in most TPS.

Bibliography

[1] AAPM. *Comprehensive methodology for the evaluation of radiation dose in X-ray computed tomography. AAPM report no. 111. Report of AAPM Task Group 111: The future of CT dosimetry.* College Park, MD: AAPM, 2010.

[2] Y. Akino, M. Koizumi, I. Sumida, Y. Takahashi, T. Ogata, S. Ota, F. Isohashi, K. Konishi, and Y. Yoshioka. Megavoltage cone beam computed tomography dose and the necessity of reoptimization for imaging dose-integrated intensity-modulated radiotherapy for prostate cancer. *Int J Radiat Oncol Biol Phys*, 82(5):1715–1722, Apr 2012.

[3] P. Alaei, G. Ding, and H. Guan. Inclusion of the dose from kilovoltage cone beam CT in the radiation therapy treatment plans. *Med Phys*, 37(1):244–248, Jan 2010.

[4] P. Alaei, B. J. Gerbi, and R. A. Geise. Generation and use of photon energy deposition kernels for diagnostic quality x rays. *Med Phys*, 26(8):1687–1697, Aug 1999.

[5] P. Alaei, B. J. Gerbi, and R. A. Geise. Evaluation of a model-based treatment planning system for dose computations in the kilovoltage energy range. *Med Phys*, 27(12):2821–2826, Dec 2000.

[6] P. Alaei, B. J. Gerbi, and R. A. Geise. Lung dose calculations at kilovoltage x-ray energies using a model-based treatment planning system. *Med Phys*, 28(2):194–198, Feb 2001.

[7] P. Alaei and E. Spezi. Commissioning kilovoltage cone-beam CT beams in a radiation therapy treatment planning system. *J Appl Clin Med Phys*, 13(6):3971, 2012.

[8] American Society for Radiation Oncology. Fast facts about radiation oncology. http://www.astro.org/PressRoom/FastFacts/documents/FFAboutRT.pdf, Aug 2009.

[9] C. Andrs, A. del Castillo, R. Tortosa, D. Alonso, and R. Barquero. A comprehensive study of the Gafchromic EBT2 radiochromic film. a comparison with EBT. *Med Phys*, 37(12):6271–6278, Dec 2010.

[10] K. E. Applegate and N. G. Cost. Image Gently: a campaign to reduce children's and adolescents' risk for cancer during adulthood. *J Adolesc Health*, 52(5 Suppl):S93–S97, May 2013.

[11] F. H. Attix. *Introduction to Radiological Physics and Radiation Dosimetry*. John Wiley & Sons, Inc., 1986.

[12] D. Bakalyar. A critical look at the numerical coefficients in CTDIVOL. *Med Phys*, 33(6):2003, June 2006.

[13] M. Bazalova, J.-F. Carrier, L. Beaulieu, and F. Verhaegen. Tissue segmentation in monte carlo treatment planning: a simulation study using dual-energy ct images. *Radiother Oncol*, 86(1):93–98, Jan 2008.

[14] M. Bazalova and E. E. Graves. The importance of tissue segmentation for dose calculations for kilovoltage radiation therapy. *Med Phys*, 38(6):3039–3049, Jun 2011.

[15] BEIR, Committee on the Biological Effects of Ionizing Radiations BEIR V, National Research Council. *Health effects of exposure to low levels of ionizing radiation: BEIR V*. National Academy Press, Washington, 1990.

[16] BEIR, Committee on the Biological Effects of Ionizing Radiations BEIR VII, National Research Council. *Health risks from exposure to low levels of ionizing radiation: BEIR VII phase 2*. National Academy Press, Washington, 2006.

[17] M. Berger, J. Hubbell, S. Seltzer, J. Chang, J. Coursey, R. Sukumar, D. Zucker, and K. Olsen. *XCOM: Photon Cross Sections Database*. National Institute of Standards and Technology, Gathersburg, MD, 2010.

[18] L. Berlin. Radiation-induced skin injuries and fluoroscopy. *Am J Roentgenol*, 177(1):21–25, Jul 2001.

[19] A. Berrington de Gonzalez, R. E. Curtis, S. F. Kry, E. Gilbert, S. Lamart, C. D. Berg, M. Stovall, and E. Ron. Proportion of second cancers attributable to radiotherapy treatment in adults: a cohort study in the US SEER cancer registries. *Lancet Oncol*, 12(4):353–360, Apr 2011.

[20] A. Berrington de Gonzlez and S. Darby. Risk of cancer from diagnostic X-rays: estimates for the UK and 14 other countries. *Lancet*, 363(9406):345–351, Jan 2004.

[21] J. Boda-Heggemann, F. Lohr, F. Wenz, M. Flentje, and M. Guckenberger. kV cone-beam CT-Based IGRT: A clinical review. *Strahlenther Onkol*, 187(5):284–291, May 2011.

[22] J. Boivin, N. Tomic, B. Fadlallah, F. Deblois, and S. Devic. Reference dosimetry during diagnostic CT examination using XR-QA radiochromic film model. *Med Phys*, 38(9):5119–5129, Sep 2011.

[23] J. M. Boone. The trouble with CTDI100. *Med Phys*, 34(4):1364–1371, Apr 2007.

[24] J. M. Boone and J. A. Seibert. An accurate method for computer-generating tungsten anode x-ray spectra from 30 to 140 kV. *Med Phys*, 24(11):1661–1670, Nov 1997.

[25] S. Brady, T. Yoshizumi, G. Toncheva, and D. Frus. Implementation of radiochromic film dosimetry protocol for volumetric dose assessments to various organs during diagnostic CT procedures. *Med Phys*, 37(9):4782–4792, Sep 2010.

[26] D. J. Brenner. Estimating cancer risks from pediatric CT: going from the qualitative to the quantitative. *Pediatr Radiol*, 32(4):228–3; discussion 242–4, Apr 2002.

[27] D. J. Brenner. Is it time to retire the CTDI for CT quality assurance and dose optimization? *Med Phys*, 32(10):3225–3226, Oct 2005.

[28] D. J. Brenner. It is time to retire the computed tomography dose index (CTDI) for CT quality assurance and dose optimization. *Med Phys*, 33(5):1189–1190, May 2006.

[29] K. K. Brock and L. A. Dawson. Adaptive management of liver cancer radiotherapy. *Semin Radiat Oncol*, 20(2):107–115, Apr 2010.

[30] M. Broderick, G. Menezes, M. Leech, M. Coffey, and M. Appleyard. A comparison of kilovoltage and megavoltage cone beam CT in radiotherapy. *Journal of Radiotherapy in Practice*, 6(3):173–178, Sep 2007.

[31] K. R. Brown and E. Rzucidlo. Acute and chronic radiation injury. *J Vasc Surg*, 53(1 Suppl):15S–21S, Jan 2011.

[32] Canadian Cancer Society's Steering Comittee on Cancer Statistics. *Canadian Cancer Statistics 2011.* Toronto, ON, May 2011.

[33] D. M. Cannon and N. Y. Lee. Recurrence in region of spared parotid gland after definitive intensity-modulated radiotherapy for head and neck cancer. *Int J Radiat Oncol Biol Phys*, 70(3):660–665, Mar 2008.

[34] C.-N. Cao, J.-W. Luo, L. Gao, J.-L. Yi, X.-D. Huang, K. Wang, S.-P. Zhang, Y. Qu, S.-Y. Li, W.-M. Cai, J.-P. Xiao, Z. Zhang, and G.-Z. Xu. Clinical characteristics and patterns of failure in the parotid region after intensity-modulated radiotherapy for nasopharyngeal carcinoma. *Oral Oncol*, 49(6):611–614, Jun 2013.

[35] J. Chen, O. Morin, M. Aubin, M. K. Bucci, C. F. Chuang, and J. Pouliot. Dose-guided radiation therapy with megavoltage cone-beam CT. *Br J Radiol*, 79(Spec No 1):S87–S98, Sep 2006.

[36] J. Cheung, J.-F. Aubry, S. S. Yom, A. R. Gottschalk, J. C. Celi, and J. Pouliot. Dose recalculation and the Dose-Guided Radiation Therapy (DGRT) process using megavoltage cone-beam CT. *Int J Radiat Oncol Biol Phys*, 74(2):583–592, Jun 2009.

[37] B. Cho, P. R. Poulsen, and P. J. Keall. Real-time tumor tracking using sequential kV imaging combined with respiratory monitoring: a general framework applicable to commonly used IGRT systems. *Phys Med Biol*, 55(12):3299–3316, Jun 2010.

[38] B. Cho, P. R. Poulsen, A. Sloutsky, A. Sawant, and P. J. Keall. First demonstration of combined kV/MV image-guided real-time dynamic multileaf-collimator target tracking. *Int J Radiat Oncol Biol Phys*, 74(3):859–867, Jul 2009.

[39] L. E. Court, L. Dong, A. K. Lee, R. Cheung, M. D. Bonnen, J. O'Daniel, H. Wang, R. Mohan, and D. Kuban. An automatic CT-guided adaptive radiation therapy technique by online modification of multileaf collimator leaf positions for prostate cancer. *Int J Radiat Oncol Biol Phys*, 62(1):154–163, May 2005.

[40] L. Cozzi, A. Fogliata, and G. Nicolini. Pre-treatment verification of intensity modulated photon beams with films and electronic portal imaging–two years of clinical experience. *Z Med Phys*, 14(4):239–250, 2004.

[41] R. de Crevoisier, S. L. Tucker, L. Dong, R. Mohan, R. Cheung, J. D. Cox, and D. A. Kuban. Increased risk of biochemical and local failure in patients with distended rectum on the planning CT for prostate cancer radiotherapy. *Int J Radiat Oncol Biol Phys*, 62(4):965–973, Jul 2005.

[42] C. Descamps, M. Gonzalez, E. Garrigo, A. Germanier, and D. Venencia. Measurements of the dose delivered during CT exams using AAPM Task Group Report No. 111. *J Appl Clin Med Phys*, 13(6):3934, 2012.

[43] S. Devic, J. Seuntjens, E. Sham, E. B. Podgorsak, C. R. Schmidtlein, A. S. Kirov, and C. G. Soares. Precise radiochromic film dosimetry using a flat-bed document scanner. *Med Phys*, 32(7):2245–2253, Jul 2005.

[44] A. Ding, J. Gu, A. V. Trofimov, and X. G. Xu. Monte carlo calculation of imaging doses

from diagnostic multidetector CT and kilovoltage cone-beam CT as part of prostate cancer treatment plans. *Med Phys*, 37(12):6199–6204, Dec 2010.

[45] G. X. Ding and C. W. Coffey. Beam characteristics and radiation output of a kilovoltage cone-beam CT. *Phys Med Biol*, 55(17):5231–5248, Sep 2010.

[46] G. X. Ding, D. M. Duggan, and C. W. Coffey. Characteristics of kilovoltage x-ray beams used for cone-beam computed tomography in radiation therapy. *Phys Med Biol*, 52(6):1595–1615, Mar 2007.

[47] G. X. Ding, D. M. Duggan, and C. W. Coffey. Accurate patient dosimetry of kilovoltage cone-beam ct in radiation therapy. *Med Phys*, 35(3):1135–1144, Mar 2008.

[48] G. X. Ding, D. M. Duggan, C. W. Coffey, M. Deeley, D. E. Hallahan, A. Cmelak, and A. Malcolm. A study on adaptive IMRT treatment planning using kV cone-beam CT. *Radiother Oncol*, 85(1):116–125, Oct 2007.

[49] G. X. Ding and P. Munro. Radiation exposure to patients from image guidance procedures and techniques to reduce the imaging dose. *Radiother Oncol*, Jul 2013.

[50] G. X. Ding, J. M. Pawlowski, and C. W. Coffey. A correction-based dose calculation algorithm for kilovoltage x rays. *Med Phys*, 35(12):5312–5316, Dec 2008.

[51] R. L. Dixon and J. M. Boone. Cone beam ct dosimetry: a unified and self-consistent approach including all scan modalities–with or without phantom motion. *Med Phys*, 37(6):2703–2718, Jun 2010.

[52] S. Don, R. Macdougall, K. Strauss, Q. T. Moore, M. J. Goske, M. Cohen, T. Herrmann, S. D. John, L. Noble, G. Morrison, L. Lehman, and B. R. Whiting. Image gently campaign back to basics initiative: ten steps to help manage radiation dose in pediatric digital radiography. *AJR Am J Roentgenol*, 200(5):W431–W436, May 2013.

[53] P. Downes, R. Jarvis, E. Radu, I. Kawrakow, and E. Spezi. Monte carlo simulation and patient dosimetry for a kilovoltage cone-beam ct unit. *Med Phys*, 36(9):4156–4167, Sep 2009.

[54] V. Dufek, I. Horakova, and L. Novak. Organ and effective doses from verification techniques in image-guided radiotherapy. *Radiat Prot Dosimetry*, 147(1-2):277–280, Sep 2011.

[55] L. Duggan, C. Hood, H. Warren-Forward, M. Haque, and T. Kron. Variations in dose response with x-ray energy of LiF:Mg,Cu,P thermoluminescence dosimeters: implications for clinical dosimetry. *Phys Med Biol*, 49(17):3831–3845, Sep 2004.

[56] C. L. Fletcher and J. A. Mills. An assessment of GafChromic film for measuring 50 kV and 100 kV percentage depth dose curves. *Phys Med Biol*, 53(11):N209–N218, Jun 2008.

[57] E. C. Ford, G. S. Mageras, E. Yorke, and C. C. Ling. Respiration-correlated spiral CT: a method of measuring respiratory-induced anatomic motion for radiation treatment planning. *Med Phys*, 30(1):88–97, Jan 2003.

[58] D. P. Frush, L. F. Donnelly, and N. S. Rosen. Computed tomography and radiation risks: what pediatric health care providers should know. *Pediatrics*, 112(4):951–957, Oct 2003.

[59] J. Geleijns, M. Salvad Artells, P. W. de Bruin, R. Matter, Y. Muramatsu, and M. F. McNitt-Gray. Computed tomography dose assessment for a 160 mm wide, 320 detector row, cone beam CT scanner. *Phys Med Biol*, 54(10):3141–3159, May 2009.

[60] T. Giaddui, Y. Cui, J. Galvin, Y. Yu, and Y. Xiao. Comparative dose evaluations between XVI and OBI cone beam CT systems using gafchromic XRQA2 film and

nanodot optical stimulated luminescence dosimeters. *Med Phys*, 40(6):062102, Jun 2013.

[61] B. Gilmore and K. Cranley. Errors in the determination of total filtration of diagnostic x-ray tubes by the HVL method. *Phys Med Biol*, 35:999–1015, 1990.

[62] D. J. Godfrey, F.-F. Yin, M. Oldham, S. Yoo, and C. Willett. Digital tomosynthesis with an on-board kilovoltage imaging device. *Int J Radiat Oncol Biol Phys*, 65(1):8–15, May 2006.

[63] Y. Gong, J. Wang, S. Bai, X. Jiang, and F. Xu. Conventionally-fractionated image-guided intensity modulated radiotherapy (ig-imrt): a safe and effective treatment for cancer spinal metastasis. *Radiat Oncol*, 3:11, 2008.

[64] K. J. Gregory, J. E. Pattison, and G. Bibbo. Uncertainties of exposure-related quantities in mammographic x-ray unit quality control. *Med Phys*, 33(3):687–698, Mar 2006.

[65] B. A. Groh, J. H. Siewerdsen, D. G. Drake, J. W. Wong, and D. A. Jaffray. A performance comparison of flat-panel imager-based MV and kV cone-beam CT. *Med Phys*, 29(6):967–975, Jun 2002.

[66] J. Gu, B. Bednarz, X. G. Xu, and S. B. Jiang. Assessment of patient organ doses and effective doses using the VIP-man adult male phantom for selected cone-beam CT imaging procedures during image guided radiation therapy. *Radiat Prot Dosimetry*, 131(4):431–443, 2008.

[67] M. Guckenberger, J. Meyer, D. Vordermark, K. Baier, J. Wilbert, and M. Flentje. Magnitude and clinical relevance of translational and rotational patient setup errors: a cone-beam CT study. *Int J Radiat Oncol Biol Phys*, 65(3):934–942, Jul 2006.

[68] E. Hall and A. Giaccia. *Radiobiology for the Radiologist.* Lippincott Williams & Wilkins, Philladelvia, PA, 6 edition, 1983.

[69] J. Hanley, G. S. Mageras, J. Sun, and G. J. Kutcher. The effects of out-of-plane rotations on two dimensional portal image registration in conformal radiotherapy of the prostate. *Int J Radiat Oncol Biol Phys*, 33(5):1331–1343, Dec 1995.

[70] R. M. Harrison. Doses to organs and tissues from concomitant imaging in radiotherapy: a suggested framework for clinical justification. *Br J Radiol*, 81(972):970–974, Dec 2008.

[71] W. D. Heemsbergen, M. S. Hoogeman, M. G. Witte, S. T. H. Peeters, L. Incrocci, and J. V. Lebesque. Increased risk of biochemical and clinical failure for prostate patients with a large rectum at radiotherapy planning: results from the Dutch trial of 68 gy versus 78 gy. *Int J Radiat Oncol Biol Phys*, 67(5):1418–1424, Apr 2007.

[72] W. R. Hendee and M. K. O'Connor. Radiation risks of medical imaging: separating fact from fantasy. *Radiology*, 264(2):312–321, Aug 2012.

[73] A. L. Hill. Half value layer measurements to facilitate patient dose assessment for newer CT scanners using published normalized dose data. *The British Journal of Radiology*, 72:792–798, 1999.

[74] C. J. Hourdakis. Determination of the diagnostic x-ray tube practical peak voltage (PPV) from average or average peak voltage measurements. *Phys Med Biol*, 56(7):2199–2217, Apr 2011.

[75] W. Huda and W. He. Estimating cancer risks to adults undergoing body CT examinations. *Radiat Prot Dosimetry*, 150(2):168–179, Jun 2012.

[76] W. Huda and F. A. Mettler. Volume CT dose index and dose-length product displayed during CT: what good are they? *Radiology*, 258(1):236–242, Jan 2011.

[77] W. Huda, K. M. Ogden, and M. R. Khorasani. Converting dose-length product to effective dose at CT. *Radiology*, 248(3):995–1003, Sep 2008.

[78] International Commission on Radiation Protection (ICRP). Recommendations of the International Commission on Radiological Protection, 1977. *Ann ICRP*, 1 (3):1–53, 1977.

[79] International Commission on Radiation Protection (ICRP). 1990 Recommendations of the International Commission on Radiological Protection. *Ann ICRP*, 21 (1-3):1–201, 1992.

[80] International Commission on Radiation Protection (ICRP). Avoidance of radiation injuries from medical interventional procedures. ICRP publication 85. *Ann ICRP*, 30:7–67, 2000.

[81] International Commission on Radiation Protection (ICRP). The 2007 recommendations of the International Commission on Radiological Protection. ICRP publication 103 . *Ann ICRP*, 37 (2-4):1–332, 2007.

[82] International Commission on Radiation Units and Measurements (ICRU). *Photon, Electron, Proton, and Neutron Interaction Data for Body Tissues.* ICRU Report 46, Bethesda, Maryland, 1992.

[83] International Commission on Radiation Units and Measurements (ICRU). *Prescribing, reccording, and reporting photon beam therapy.* ICRU Report 50, Bethesda, Maryland, 1993.

[84] M. K. Islam, T. G. Purdie, B. D. Norrlinger, H. Alasti, D. J. Moseley, M. B. Sharpe, J. H. Siewerdsen, and D. A. Jaffray. Patient dose from kilovoltage cone beam computed tomography imaging in radiation therapy. *Med Phys*, 33(6):1573–1582, Jun 2006.

[85] F. Jacso, Y. Poirier, J. Grafe, I. Nygren, E. Villareal-Barajas, and R. Khan. Orthovolt-age dosimetry using ion chambers, GAFchromic EBT3 film and kV dose computations. *Radiother Oncol*, 108:S145, 2013.

[86] D. A. Jaffray. Emergent technologies for 3-dimensional image-guided radiation deliv-ery. *Semin Radiat Oncol*, 15(3):208–216, Jul 2005.

[87] D. A. Jaffray, D. G. Drake, M. Moreau, A. A. Martinez, and J. W. Wong. A ra-diographic and tomographic imaging system integrated into a medical linear acceler-ator for localization of bone and soft-tissue targets. *Int J Radiat Oncol Biol Phys*, 45(3):773–789, Oct 1999.

[88] D. A. Jaffray, J. H. Siewerdsen, J. W. Wong, and A. A. Martinez. Flat-panel cone-beam computed tomography for image-guided radiation therapy. *Int J Radiat Oncol Biol Phys*, 53(5):1337–1349, Aug 2002.

[89] H. Johns and J. Cunningham. *The physics of radiology.* Springfield, Illinois, 4 edition, 1983.

[90] C. Johnstone, R. LaFontaine, Y. Poirier, A. Kouznetsov, and M. Tambasco. Validation of in-house dose calculation software for superficial therapy. *Radiother Oncol*, 108:S302, 2013.

[91] Joint Working Party of the British Institute of Radiology and the Hospital Physicists' Association. Central axis depth dose data for use in radiotherapy. a survey of depth doses and related data measured in water or equivalent media. *Br J Radiol Suppl*, 17:1–147, 1983.

[92] Joint Working Party of the British Institute of Radiology and the Hospital Physicists' Association. Central axis depth dose data for use in radiotherapy: 1996. a survey of

depth doses and related data measured in water or equivalent media. *Br J Radiol Suppl*, 25:1–188, 1996.

[93] R. A. Jucius and G. X. Kambic. Radiation dosimetry in computed tomography (CT). *Proc. SPIE 0127, Application of Optical Instrumentation in Medicine VI*, Proc. SPIE 0127, Application of Optical Instrumentation in Medicine VI, 286:286, 1977.

[94] M. W. K. Kan, L. H. T. Leung, W. Wong, and N. Lam. Radiation dose from cone beam computed tomography for image-guided radiation therapy. *Int J Radiat Oncol Biol Phys*, 70(1):272–279, Jan 2008.

[95] I. Kawrakow and D. Rogers. The EGSnrc Code System: Monte Carlo simulation of electron and photon transport. Technical report, Technical Report PIRS701, National Research Council of Canada, Ottawa, Canada, 2002.

[96] P. J. Keall, G. S. Mageras, J. M. Balter, R. S. Emery, K. M. Forster, S. B. Jiang, J. M. Kapatoes, D. A. Low, M. J. Murphy, B. R. Murray, C. R. Ramsey, M. B. Van Herk, S. S. Vedam, J. W. Wong, and E. Yorke. The management of respiratory motion in radiation oncology report of AAPM Task Group 76. *Med Phys*, 33(10):3874–3900, Oct 2006.

[97] F. Khan. *The Physics of Radiation Therapy.* Lippincott Williams & Wilkins, Philadelphia, PA USA, third edition, 2003.

[98] D. W. Kim, W. K. Chung, and M. Yoon. Imaging doses and secondary cancer risk from kilovoltage cone-beam CT in radiation therapy. *Health Phys*, 104(5):499–503, May 2013.

[99] S. Kim, S. Yoo, F.-F. Yin, E. Samei, and T. Yoshizumi. Kilovoltage cone-beam CT: comparative dose and image quality evaluations in partial and full-angle scan protocols. *Med Phys*, 37(7):3648–3659, Jul 2010.

[100] C. Kirkby, E. Ghasroddashti, Y. Poirier, M. Tambasco, and R. D. Stewart. RBE of kV CBCT radiation determined by Monte Carlo DNA damage simulations. *Phys Med Biol*, 58(16):5693–5704, Aug 2013.

[101] K. Kitamura, H. Shirato, Y. Seppenwoolde, R. Onimaru, M. Oda, K. Fujita, S. Shimizu, N. Shinohara, T. Harabayashi, and K. Miyasaka. Three-dimensional intrafractional movement of prostate measured during real-time tumor-tracking radiotherapy in supine and prone treatment positions. *Int J Radiat Oncol Biol Phys*, 53(5):1117–1123, Aug 2002.

[102] S. Korreman, C. Rasch, H. McNair, D. Verellen, U. Oelfke, P. Maingon, B. Mijnheer, and V. Khoo. The European Society of Therapeutic Radiology and Oncology-European Institute of Radiotherapy (ESTRO-EIR) report on 3D CT-based in-room image guidance systems: a practical and technical review and guide. *Radiother Oncol*, 94(2):129–144, Feb 2010.

[103] A. Kouznetsov and M. Tambasco. A hybrid approach for rapid, accurate, and direct kilovoltage radiation dose calculations in CT voxel space. *Med Phys*, 38(3):1378–1388, Mar 2011.

[104] F. J. Lagerwaard, J. R. Van Sornsen de Koste, M. R. Nijssen-Visser, R. H. Schuchhard-Schipper, S. S. Oei, A. Munne, and S. Senan. Multiple "slow" CT scans for incorporating lung tumor mobility in radiotherapy planning. *Int J Radiat Oncol Biol Phys*, 51(4):932–937, Nov 2001.

[105] C. E. Land. Estimating cancer risks from low doses of ionizing radiation. *Science*, 209(4462):1197–1203, Sep 1980.

[106] C. Lee, K. P. Kim, D. J. Long, and W. E. Bolch. Organ doses for reference pediatric and adolescent patients undergoing computed tomography estimated by Monte Carlo simulation. *Med Phys*, 39(4):2129–2146, Apr 2012.

[107] W. Leitz, B. Axelsson, and G. Szendro. Computed tomography dose assessmentA practical approach. *Radiat. Prot. Dosim.*, 57:377380, 1995.

[108] X. Li, E. Samei, P. Segars, G. Sturgeon, J. G. Colsher, G. Toncheva, T. Yoshizumi, and D. P. Frush. Patient-specific radiation dose and cancer risk estimation in CT: Part i. development and validation of a Monte Carlo program. *Med Phys*, 38(1):397–407, Jan 2011.

[109] X. Li, D. Zhang, and B. Liu. Calculations of two new dose metrics proposed by AAPM Task Group 111 using the measurements with standard CT dosimetry phantoms. *Med Phys*, 40(8):081914, Aug 2013.

[110] D. Lpez Aventn, I. Gil, D. M. Lpez Gonzlez, and R. M. Pujol. Chronic scalp ulceration as a late complication of fluoroscopically guided cerebral aneurysm embolization. *Dermatology*, 224(3):198–203, 2012.

[111] C.-M. Ma, C. Coffey, L. Dewerd, C. Liu, R. Nath, S. Seltzer, and J. Seutjens. AAPM protocol for 40-300 kV x-ray beam dosimetry in radiotherapy and radiobiology. *Med Phys*, 28:868–893, June 2001.

[112] C. M. Ma and J. P. Seuntjens. Mass-energy absorption coefficient and backscatter factor ratios for kilovoltage x-ray beams. *Phys Med Biol*, 44(1):131–143, Jan 1999.

[113] T. R. Mackie, J. W. Scrimger, and J. J. Battista. A convolution method of calculating dose for 15-MV x rays. *Med Phys*, 12(2):188–196, 1985.

[114] I. Marco-Rius, L. Wack, P. Tsiamas, E. Tryggestad, R. Berbeco, J. Hesser, and P. Zygmanski. A fast analytic dose calculation method for arc treatments for kilovoltage small animal irradiators. *Phys Med*, 29(5):426–435, Sep 2013.

[115] G. Marinello, J.-P. Mege, M.-C. Besse, G. Kerneur, and J.-L. Lagrange. [prostate radiation therapy: in vivo measurement of the dose delivered by kv-cbct]. *Cancer*

Radiother, 13(5):353–357, Sep 2009.

[116] L. B. Marks, R. K. Ten Haken, and M. K. Martel. Guest editor's introduction to QUANTEC: a users guide. *Int J Radiat Oncol Biol Phys*, 76(3 Suppl):S1–S2, Mar 2010.

[117] J. D. Mathews, A. V. Forsythe, Z. Brady, M. W. Butler, S. K. Goergen, G. B. Byrnes, G. G. Giles, A. B. Wallace, P. R. Anderson, T. A. Guiver, P. McGale, T. M. Cain, J. G. Dowty, A. C. Bickerstaffe, and S. C. Darby. Cancer risk in 680,000 people exposed to computed tomography scans in childhood or adolescence: data linkage study of 11 million Asustralians. *BMJ*, 346:f2360, 2013.

[118] L. N. McDermott, M. Wendling, B. van Asselen, J. Stroom, J. J. Sonke, M. van Herk, and B. J. Mijnheer. Clinical experience with EPID dosimetry for prostate IMRT pre-treatment dose verification. *Med Phys*, 33(10):3921–3930, Oct 2006.

[119] K. McMillan, M. McNitt-Gray, and D. Ruan. Development and validation of a measurement-based source model for kilovoltage cone-beam CT Monte Carlo dosimetry simulations. *Med Phys*, 40, 2013.

[120] M. F. McNitt-Gray. AAPM/RSNA physics tutorial for residents: Topics in CT. radiation dose in CT. *Radiographics*, 22(6):1541–1553, 2002.

[121] P. Metcalfe, T. Kron, and P. Hoban. *The Physics of Radiation x-rays and electron.* Medical Physics Publishing, Madison, Wisconsin, 2007.

[122] E. L. Mitchell and P. Furey. Prevention of radiation injury from medical imaging. *J Vasc Surg*, 53(1 Suppl):22S–27S, Jan 2011.

[123] S. Mori, M. Endo, K. Nishizawa, T. Tsunoo, T. Aoyama, H. Fujiwara, and K. Murase. Enlarged longitudinal dose profiles in cone-beam CT and the need for modified dosimetry. *Med Phys*, 32(4):1061–1069, Apr 2005.

[124] R. Morin. *Monte Carlo Simulations in the Radiological Sciences.* CRC Press, Inc., Boca Raton, U.S.A., 1988.

[125] M. J. Murphy. Tracking moving organs in real time. *Semin Radiat Oncol*, 14(1):91–100, Jan 2004.

[126] M. J. Murphy, J. Balter, S. Balter, B. J. A, I. J. Das, S. B. Jiang, C. M. Ma, G. H. Olivera, R. F. Rodebaugh, K. J. Ruchala, H. Shirato, and F.-F. Yin. The management of imaging dose during image-guided radiotherapy: report of the AAPM Task Group 75. *Med Phys*, 34(10):4041–4063, Oct 2007.

[127] National Council on Radiation Protection (NCRP). *Implementation of the principle of as low as reasonably achievable (ALARA) for medical and dental personel.* NCRP Report 107, Bethesda, Maryland, 1990.

[128] C. Noblet, S. Chiavassa, F. Paris, S. Supiot, A. Lisbona, and G. Delpon. Underestimation of dose delivery in preclinical irradiation due to scattering conditions. *Phys Med*, pages 1120–1797, Mar 2013.

[129] M. of the Cross Sections Evaluation Working Group. *ENDF-6 Formats Manual, Data Formats and Procedures for the Evaluated Nuclear Data File, ENDF/B-VI and ENDF/B-VII.* Brookhaven National Laboratory, Upton, NY, 2009.

[130] M. E. O'Malley, P. Chung, M. Haider, H.-J. Jang, K. Jhaveri, K. Khalili, T. Panzarella, and P. Warde. Comparison of low dose with standard dose abdominal/pelvic multi-detector ct in patients with stage 1 testicular cancer under surveillance. *Eur Radiol*, 20(7):1624–1630, Jul 2010.

[131] A. Palm, E. Nilsson, and L. Herrnsdorf. Absorbed dose and dose rate using the Varian OBI 1.3 and 1.4 CBCT system. *J Appl Clin Med Phys*, 11(1):3085–3096, 2010.

[132] A. Paterson, D. P. Frush, and L. F. Donnelly. Helical CT of the body: are settings adjusted for pediatric patients? *AJR Am J Roentgenol*, 176(2):297–301, Feb 2001.

[133] J. M. Pawlowski and G. X. Ding. A new approach to account for the medium-dependent effect in model-based dose calculations for kilovoltage x-rays. *Phys Med Biol*, 56(13):3919–3934, Jul 2011.

[134] S. T. H. Peeters, W. D. Heemsbergen, P. C. M. Koper, W. L. J. van Putten, A. Slot, M. F. H. Dielwart, J. M. G. Bonfrer, L. Incrocci, and J. V. Lebesque. Dose-response in radiotherapy for localized prostate cancer: results of the Dutch multicenter randomized phase iii trial comparing 68 gy of radiotherapy with 78 gy. *J Clin Oncol*, 24(13):1990–1996, May 2006.

[135] C. L. Perkins, T. Fox, E. Elder, D. A. Kooby, C. A. Staley, 3rd, and J. Landry. Image-guided radiation therapy (IGRT) in gastrointestinal tumors. *JOP*, 7(4):372–381, 2006.

[136] Y. Poirier. The effect of small cylindrical air cavities on circumferential dose distributions due to small 6 MV photon fields. Master's thesis, McMaster University, 2007.

[137] Y. Poirier, A. Kouznetsov, B. Koger, and M. Tambasco. Experimental validation of a kilovoltage x-ray source model for computing imaging dose. *Med Phys*, 41:041915, 07 2014.

[138] Y. Poirier, A. Kouznetsov, and M. Tambasco. A simplified approach to characterizing a kilovoltage source spectrum for accurate dose computation. *Med Phys*, 39(6):3041–3050, Jun 2012.

[139] Y. Poirier, A. Kouznetsov, and M. Tambasco. Erratum: "a simplified approach to characterizing a kilovoltage source spectrum for accurate dose computation" [med. phys. 39(6), 3041-3050 (2012)]. *Med Phys*, 40(7):077201, Jul 2013.

172

[140] A. Pollack, A. L. Hanlon, E. M. Horwitz, S. J. Feigenberg, A. A. Konski, B. Movsas, R. E. Greenberg, R. G. Uzzo, C.-M. C. Ma, S. W. McNeeley, M. K. Buyyounouski, and R. A. Price, Jr. Dosimetry and preliminary acute toxicity in the first 100 men treated for prostate cancer on a randomized hypofractionation dose escalation trial. *Int J Radiat Oncol Biol Phys*, 64(2):518–526, Feb 2006.

[141] J. Pouliot, A. Bani-Hashemi, J. Chen, M. Svatos, F. Ghelmansarai, M. Mitschke, M. Aubin, P. Xia, O. Morin, K. Bucci, M. Roach, 3rd, P. Hernandez, Z. Zheng, D. Hristov, and L. Verhey. Low-dose megavoltage cone-beam CT for radiation therapy. *Int J Radiat Oncol Biol Phys*, 61(2):552–560, Feb 2005.

[142] E. H. N. Pow, D. L. W. Kwong, A. S. McMillan, M. C. M. Wong, J. S. T. Sham, L. H. T. Leung, and W. K. Leung. Xerostomia and quality of life after intensity-modulated radiotherapy vs. conventional radiotherapy for early-stage nasopharyngeal carcinoma: initial report on a randomized controlled clinical trial. *Int J Radiat Oncol Biol Phys*, 66(4):981–991, Nov 2006.

[143] R. J. Preston. Update on linear non-threshold dose-response model and implications for diagnostic radiology procedures. *Health Phys*, 95(5):541–546, Nov 2008.

[144] O. Rampado, E. Garelli, and R. Ropolo. Computed tomography dose measurements with radiochromic films and a flatbed scanner. *Med Phys*, 37(1):189–196, Jan 2010.

[145] C. Ramsey, R. Seibert, S. L. Mahan, D. Desai, and D. Chase. Out-of-field dosimetry measurements for a helical tomotherapy system. *J Appl Clin Med Phys*, 7(3):1–11, 2006.

[146] M. M. Rehani and P. Ortiz-Lopez. Radiation effects in fluoroscopically guided cardiac interventions–keeping them under control. *Int J Cardiol*, 109(2):147–151, May 2006.

[147] A. Richter, Q. Hu, D. Steglich, K. Baier, J. Wilbert, M. Guckenberger, and M. Flentje.

Investigation of the usability of cone-beam CT data sets for dose calculation. *Radiat Oncol*, 3:42, 2008.

[148] H. D. Royal. Effects of low level radiation-what's new? *Semin Nucl Med*, 38(5):392–402, Sep 2008.

[149] H. Shirato, M. Oita, K. Fujita, Y. Watanabe, and K. Miyasaka. Feasibility of synchronization of real-time tumor-tracking radiotherapy and intensity-modulated radiotherapy from viewpoint of excessive dose from fluoroscopy. *Int J Radiat Oncol Biol Phys*, 60(1):335–341, Sep 2004.

[150] H. Shirato, Y. Seppenwoolde, K. Kitamura, R. Onimura, and S. Shimizu. Intrafractional tumor motion: lung and liver. *Semin Radiat Oncol*, 14(1):10–18, Jan 2004.

[151] T. B. Shope. Radiation-induced skin injuries from fluoroscopy. *Radiographics*, 16(5):1195–1199, Sep 1996.

[152] T. B. Shope, R. M. Gagne, and G. C. Johnson. A method for describing the doses delivered by transmission x-ray computed tomography. *Med Phys*, 8(4):488–495, 1981.

[153] J. H. Siewerdsen, A. M. Waese, D. J. Moseley, S. Richard, and D. A. Jaffray. Spektr: a computational tool for x-ray spectral analysis and imaging system optimization. *Med Phys*, 31(11):3057–3067, Nov 2004.

[154] M. Sommerville, Y. Poirier, A. Kouznetsov, and M. Tambasco. Using HVL and KVp to portray an x-ray source for dose calculations in CT. *Med Phys*, 40:404, 2013.

[155] M. A. Speidel, B. P. Wilfley, A. Hsu, and D. Hristov. Feasibility of low-dose single-view 3D fiducial tracking concurrent with external beam delivery. *Med Phys*, 39(4):2163–2169, Apr 2012.

[156] E. Spezi, W. Volken, D. Frei, and M. Fix. A virtual source model for kilo-voltage cone beam CT: Source characteristics and model validation. *Med Phys*, 38:5254–5263, 2011.

[157] J. Staffurth and R. D. B. . A review of the clinical evidence for intensity-modulated radiotherapy. *Clin Oncol (R Coll Radiol)*, 22(8):643–657, Oct 2010.

[158] M. F. Steinke and E. Bezak. Technological approaches to in-room CBCT imaging. *Australas Phys Eng Sci Med*, 31(3):167–179, Sep 2008.

[159] K. L. Stephans, P. Xia, R. D. Tendulkar, and J. P. Ciezki. The current status of image-guided external beam radiotherapy for prostate cancer. *Curr Opin Urol*, 20(3):223–228, May 2010.

[160] H. Svensson. Quality assurance in radiation therapy: physical aspects. *Int J Radiat Oncol Biol Phys*, 10 Suppl 1:59–65, Jun 1984.

[161] E. Svik, N. E. Klw, J. Hellesnes, and J. Lykke. Radiation-induced skin injury after percutaneous transluminal coronary angioplasty. case report. *Acta Radiol*, 37(3 Pt 1):305–306, May 1996.

[162] V. M. Systems. *Varian On-Board Imager (OBI) Reference Guide.* Varian Medical Systems, Palo Alto (CA):, 2008. p.17071.

[163] J. A. Tanyi and M. H. Fuss. Volumetric image-guidance: does routine usage prompt adaptive re-planning? an institutional review. *Acta Oncol*, 47(7):1444–1453, 2008.

[164] T. H. M. Thomas, D. Devakumar, S. Balukrishna, H. F. Godson, and B. P. Ravindran. Validation of image registration and fusion of MV CBCT and planning CT for radiotherapy treatment planning. *Australas Phys Eng Sci Med*, 34(4):441–447, Dec 2011.

[165] T. H. M. Thomas, D. Devakumar, S. Purnima, and B. P. Ravindran. The adaptation of megavoltage cone beam CT for use in standard radiotherapy treatment planning. *Phys Med Biol*, 54(7):2067–2077, Apr 2009.

[166] W. A. Tom, H. A. Jaradat, I. A. Nelson, M. A. Ritter, and M. P. Mehta. Helical tomotherapy: image guidance and adaptive dose guidance. *Front Radiat Ther Oncol*, 40:162–178, 2007.

[167] Tomic, N., Devic, S., DeBlois, F., and J. Seuntjens. Reference radiochromic film dosimetry in kilovoltage photon beams during CBCT image acquisition. *Med Phys*, 37(3):1083–1092, Mar 2010.

[168] N. T. Tran, T. Iimoto, and T. Kosako. Calibration of kVp meter used in quality control tests of diagnostic x-ray units. *Radiat Prot Dosimetry*, 144(1-4):257–261, Mar 2011.

[169] M. Tubiana, A. Aurengo, D. Averbeck, and R. Masse. The debate on the use of linear no threshold for assessing the effects of low doses. *J Radiol Prot*, 26(3):317–324, Sep 2006.

[170] A. C. Turner, D. Zhang, H. J. Kim, J. J. DeMarco, C. H. Cagnon, E. Angel, D. D. Cody, D. M. Stevens, A. N. Primak, C. H. McCollough, and M. F. McNitt-Gray. A method to generate equivalent energy spectra and filtration models based on measurement for multidetector CT Monte Carlo dosimetry simulations. *Med Phys*, 36(6):2154–2164, Jun 2009.

[171] A. van der Reijden, M. van Herk, and J.-J. Sonke. Motion compensated digital tomosynthesis. *Radiother Oncol*, Oct 2013.

[172] J. Van Dyk. *The Modern Technology of Radiation Oncology*. Medical Physics Publishing, Madison, Wisconsin, 1999.

[173] W. van Elmpt, L. McDermott, S. Nijsten, M. Wendling, P. Lambin, and B. Mijnheer. A literature review of electronic portal imaging for radiotherapy dosimetry. *Radiother Oncol*, 88(3):289–309, Sep 2008.

[174] W. van Elmpt, S. Nijsten, S. Petit, B. Mijnheer, P. Lambin, and A. Dekker. 3D in vivo dosimetry using megavoltage cone-beam CT and EPID dosimetry. *Int J Radiat Oncol Biol Phys*, 73(5):1580–1587, Apr 2009.

[175] M. van Herk. Errors and margins in radiotherapy. *Semin Radiat Oncol*, 14(1):52–64, Jan 2004.

[176] M. van Herk. Different styles of image-guided radiotherapy. *Semin Radiat Oncol*, 17(4):258–267, Oct 2007.

[177] B. Vanderstraeten, P. W. Chin, M. Fix, A. Leal, G. Mora, N. Reynaert, J. Seco, M. Soukup, W. Spezi, E.and De Neve, and H. Thierens. Conversion of CT nnumber into tissue pparameter for Monte Carlo dose calculations: a multi-centre study. *Phys Med Biol*, 52(3):539–562, Feb 2007.

[178] D. Verellen, M. De Ridder, and G. Storme. A (short) history of image-guided radio-therapy. *Radiother Oncol*, 86(1):4–13, Jan 2008.

[179] R. E. Vlietstra, L. K. Wagner, T. Koenig, and F. Mettler. Radiation burns as a severe complication of fluoroscopically guided cardiological interventions. *J Interv Cardiol*, 17(3):131–142, Jun 2004.

[180] L. K. Wagner, M. D. McNeese, M. V. Marx, and E. L. Siegel. Severe skin reactions from interventional fluoroscopy: case report and review of the literature. *Radiology*, 213(3):773–776, Dec 1999.

[181] Z.-H. Wang, C. Yan, Z.-Y. Zhang, C.-P. Zhang, H.-S. Hu, W.-Y. Tu, J. Kirwan, and W. M. Mendenhall. Impact of salivary gland dosimetry on post-IMRT recovery of saliva output and xerostomia grade for head-and-neck cancer patients treated with or without contralateral submandibular gland sparing: a longitudinal study. *Int J Radiat Oncol Biol Phys*, 81(5):1479–1487, Dec 2011.

[182] N. Wen, H. Guan, R. Hammoud, D. Pradhan, T. Nurushev, S. Li, and B. Movsas. Dose delivered from Varian's CBCT to patients receiving IMRT for prostate cancer. *Phys Med Biol*, 52(8):2267–2276, Apr 2007.

[183] H. Wertz, D. Stsepankou, M. Blessing, M. Rossi, C. Knox, K. Brown, U. Gros, J. Boda-Heggemann, C. Walter, J. Hesser, F. Lohr, and F. Wenz. Fast kilovoltage/megavoltage (kVMV) breathhold cone-beam CT for image-guided radiotherapy of lung cancer. *Phys Med Biol*, 55(15):4203–4217, Aug 2010.

[184] D. R. White, H. Q. Woodard, and S. M. Hammond. Average soft-tissue and bone models for use in radiation dosimetry. *Br J Radiol*, 60(717):907–913, Sep 1987.

[185] C. Wu, R. Jeraj, G. H. Olivera, and T. R. Mackie. Re-optimization in adaptive radiotherapy. *Phys Med Biol*, 47(17):3181–3195, Sep 2002.

[186] Q. J. Wu, D. Thongphiew, Z. Wang, B. Mathayomchan, V. Chankong, S. Yoo, W. R. Lee, and F.-F. Yin. On-line re-optimization of prostate IMRT plans for adaptive radiation therapy. *Phys Med Biol*, 53(3):673–691, Feb 2008.

[187] X-5 Monte Carlo Team. *MCNP- A general Monte Carlo N-particle transport code, Version 5, Vol. I: Overview and theory.* Los Alamos National Laboratory, CA, 2003.

[188] D. Yan, D. Lockman, D. Brabbins, L. Tyburski, and A. Martinez. An off-line strategy for constructing a patient-specific planning target volume in adaptive treatment process for prostate cancer. *Int J Radiat Oncol Biol Phys*, 48(1):289–302, Aug 2000.

[189] Y. Yang, E. Schreibmann, T. Li, C. Wang, and L. Xing. Evaluation of on-board kV cone beam CT (CBCT)-based dose calculation. *Phys Med Biol*, 52(3):685–705, Feb 2007.

[190] S. Yoo, Q. J. Wu, D. Godfrey, H. Yan, L. Ren, S. Das, W. R. Lee, and F.-F. Yin. Clinical evaluation of positioning verification using digital tomosynthesis and bony

anatomy and soft tissues for prostate image-guided radiotherapy. *Int J Radiat Oncol Biol Phys*, 73(1):296–305, Jan 2009.

[191] O. A. Zeidan, S. A. L. Stephenson, S. L. Meeks, T. H. Wagner, T. R. Willoughby, P. A. Kupelian, and K. M. Langen. Characterization and use of EBT radiochromic film for IMRT dose verification. *Med Phys*, 33(11):4064–4072, Nov 2006.

[192] Y. Zhang, L. Ren, C. C. Ling, and F.-F. Yin. Respiration-phase-matched digital tomosynthesis imaging for moving target verification: A feasibility study. *Med Phys*, 40(7):071723 (1–13), Jul 2013.

[193] H. Zhou, P. J. Keall, and E. E. Graves. A bone composition model for Monte Carlo x-ray transport simulations. *Med Phys*, 36(3):1008–1018, Mar 2009.